NOVEL METHODS TO CONSTRUCT MICROCHANNEL NETWORKS WITH COMPLEX TOPOLOGIES

A Dissertation

by

JEN-HUANG HUANG

Submitted to the Office of Graduate Studies of
TexasA&MUniversity
in partial fulfillment of the requirements for the degree of

DOCTOR OF PHILOSOPHY

Approved by:

Chair of Committee,	Victor M. Ugaz
Committee Members,	Arul Jayaraman
	YueKuo
	Suresh Pillai
Head of Department,	M. NazmulKarim

December 2012

Major Subject: Chemical Engineering

ABSTRACT

Microfluidic technology is a useful tool to help answer unsolved problems in multidisciplinary fields, including molecular biology, clinical pathology and the pharmaceutical industry.Current microfluidic based devices with diverse structures have been constructed via extensively used soft lithography orphotolithography fabrication methods. A layer-by-layer stacking of 2D planar microchannel arrays can achieve a limited degree of three dimensionality. However, assembly of large-scale multi-tiered structures is tedious, and the inherently planar nature of the individual layers restricts the network's topological complexity. In order to overcome the limitations of existing microfabrication methodswe demonstrate several novel methods that enable microvasculature networks: electrostatic discharge,global channel deformation and enzymatic sculpting to fabricate complex surface topologies.

These methods enable construction of networks of branched microchannels arranged in a tree-like architecture with diameters ranging from approximately 10 μm to 1 mm. Interconnected networks with multiple fluidic access points can be straightforwardly constructed, and quantification of their branching characteristics reveals remarkable similarity to naturally occurring vasculature. In addition, by harnessing enzymatic micromachining we are able to construct nanochannels, microchannels containing embedded features templated by the substrate's crystalline morphology, and an irregular cross section of microchannel capable of performing isolation and enrichment of cells from whole blood with throughput 1 – 2 orders of

magnitude faster than currently possible. These techniques can play a key role in developing an organ-sized engineered tissue scaffolds and high-throughput continuous flow separations.

DEDICATION

To my parents,

my beloved wife Sharon,

my sisters Liting and Lidia,

my uncle Dr. Je-Chin Han and his family

and my son Andrew

ACKNOWLEDGEMENTS

I express my sincere and heartfelt gratitude to my advisor, Dr. Victor M. Ugaz for his invaluable supervision and support throughout this important phase of my career. With his guidance, I learned how to solve a very complicated problemwith several creative methods and also learned how to become aresponsible researcher to face more future challenges independently.

I also would like to give my great appreciate to my committee members, Dr. Arul Jayaraman, Dr. YueKuo and Dr. Suresh Pillai to guide me and give me useful advices and insights on the research.I am grateful to Dr.Pillai and the staff at the National Center for Electron Beam Research (Texas A&M) for assistance with the electron beam irradiation experiments.I also thank Dr. Jayaraman generously forproviding his lab to complete my experiments and Dr. Maria King for assistance with cell counting experiments. I want to especially thank my mentor Dr. Jeongyun Kim to guide me and explore my view in research.

I am also indebted to my past and present group members: Roger Lo, Faisal Shaikh, Jian Wang, Xiaojia Chen, SerdarOzturk, RadhaMuddu, Jose C. Contreras Naranjo, Yu-Wen Huang, Nan Shi, Aashish Priye, FanxuMeng, Duanduan Han, Molly E. Morin and Derek Schwanz,for their support, inspiration, and entertainment.

Finally, I am truly grateful for my parents, my uncle's family and my lovely wife for their continuous encouragement and support. This work would not be completed without them.

NOMENCLATURE

2D	Two dimensional
3D	Three dimensional
CTC	Circulating tumor cell
EC	Endothelial cell
ECM	Extracellular matrix
κ	Dean number
PDMS	Poly(dimethylsiloxane)
PK	Proteinase K
PLA	Poly(lactic acid)
PMMA	Poly(methyl methacrylate)
RBC	Red blood cell
Re	Reynolds number
SEM	Scanning electron microscopy
SMC	Smooth muscle cell
WBC	White blood cell

TABLE OF CONTENTS

Page

Page

LIST OF FIGURES

LIST OF TABLES

CHAPTER I

INTRODUCTION

1.1 Overview

Microenvironments throughout nature incorporate complex topologies that assist in orchestrating a host of physical and biological functions, particularly in the presence of flow where phenomena at surfaces and in the bulk fluid are often strongly coupled.Current models have been developed to mimic these distinctive features which can be applied,for example, to fabricatean artificial microvascular network for tissue engineering applications via softlithography[1, 2].Similarly, intricately-shaped surface features can be exploited to establish flow fields capable of providing enhanced transport that has proven beneficial in applications like micromixing[3-5]. Despite their importance, however, many of these structured features and surfaces are challenging to build using existing micromachining methods.The goal of my research is (1) to develop the fabrication technologies to overcome one of the greatest obstacles in the field of tissue engineering by mimicking the vasculature network inside organ-size biomaterial scaffoldsand (2) to establish an innovative microfluidic-base filtration method capable of performing simultaneous size-based isolation and enrichment of circulating tumor cells.I hypothesized that a fabricated microvascular network and constructed complex topologiescan be used both to transport nutrients to maintain the viability of cells and to separate cancer cells from the blood stream.

1.2 MicrovascularNetwork

Interest in developing new capabilities to engineer artificial tissue and organ structures suitable for implantation has intensified during the past decade owing to theirenormous untapped lifesaving potential. Health care costs related to organ failure are staggering, easily extending into the hundreds of billions of dollars in the US alone—a situation compounded by the fact that transplantation is often the only viable therapeutic option in many cases (e.g. acute physical trauma, severe burns, etc.)[6]. A well-known example is cardiovascular disease, a condition impacting over 80 million adults in the US, contributing to 1 out of every 3 deaths in 2007[7]. These problems are expected to grow over the coming years as overall life expectancies increase, as evidenced by the fact that the waiting list for donor organs in the US has doubled in size during the past 20 years. In 2010, out of a total of 110,942 patients on the transplantation waiting list in the US, however,only 22,104 received organs and 6,521 died awaiting a suitable donor (Organ Procurement and Transplantation Network, http://optn.transplant.hrsa.gov/). Engineered organ replacements offer a compelling alternative to address this growing need.

A major barrier to production of organ-sized tissue constructs is the challengeof designing scaffold microenvironments that are capable of providing sufficient nutrient delivery and waste removal throughout extended three-dimensional volumes[8-12]. Incredible progress has been made toward development of porous biodegradable scaffolds for tissue culture[13-15], but transport within these scaffolds primarily occurs by molecular diffusion—a passive and inherently slow process. This fundamental limitation

effectively restricts the maximum thickness of engineered tissues to 100 – 200 μm[16, 17], beyond which cells in the interior remain nutrient limited and die[18, 19]. In nature, vascular networks have evolved to elegantly address this problem by incorporating highly branched fractal-like architectures that are efficiently space-filling while minimizing the energy required to sustain transport[20, 21]. Metabolically active cells in the body, for example, are often located no more than 50 – 100 μm away from a capillary bed. In addition to functioning as local nutrient and waste sinks, the specific microstructure and positioning of these capillary networks provide cues that help orchestrate the organization and differentiation of cells within the tissue structure. Consequently, the ability to embed functional capillary networks within tissue engineering scaffolds would represent a significant step toward manufacturing organ-sized constructs *in vitro*[22, 23].

1.2.1 Characteristics of branched vascular networks

Naturally occurring vascular networks are notoriously challenging to replicate artificially owing to their unique complexity, characterized by a well-defined global architecture that persists despite the fact that no two networks are completely identical at all structural levels. However, despite these variations, there is self-similarity expressed in terms of parameters related to a network's branching characteristics (average branching angle, diameter ratio and symmetry between parent and daughter branches, fractal dimension, etc.). One of these key parameters more directly related to transport efficiency can be obtained by considering a balance between the energy needed to sustain flow through a conduit versus the energy required to produce enough fluid to fill

its volume. This analysis yields a relationship known as Murray's law, predicting that an optimal system-wide state of uniform shear stress corresponds to a global scaling of flow rate with the cube of microchannel diameter[24-27]. Specifically, in the case of a parent channel of diameter d_0 bifurcating into two daughter channels with diameters d_1 and d_2, Murray's law implies that $d_0^k = d_1^k + d_2^k$ where a value of $k = 3$ is predicted under ideal conditions (e.g., laminar, non-pulsatile flow). In physiological systems, values of the branching exponent k generally range between 2 and 3 depending on location within the network (e.g., data from porcine vasculature display scaling exponents of $k = 2.82$ for $d_0 \leq 40$ μm, $k = 2.50$ for $40 < d_0 \leq 200$ μm, and $k = 2.35$ for $d_0 > 200$ μm)[28-30]. Other notable examples include human pulmonary vasculature ($k \sim 2.5$[31]) and the pig coronary arterial tree ($k \sim 2.2$[32]). These deviations from the ideal $k = 3$ scaling arise in part because pulsatile flow generally dominates in the larger diameter vessels (e.g., aorta and major arteries), where area-preserving branching ($k = 2$) helps to minimize wave reflections at the branching points[33]. Smaller vessels, on the other hand, maintain exponents closer to $k = 3$ because the need to maintain the blood flow with minimal energy consumption becomes a dominant consideration[21].

1.2.2 Fabrication of 2D microvascular networks

Although methods currently exist to artificially construct analogs of individual large blood vessels, the formation of the much smaller diameter capillaries is more challenging. Photolithography-based micromachining methods have recently emerged as valuable tools to enable construction of microfluidic and

microelectromechanicalsystems. These same processes offer a natural avenue to construct vascular-mimicking networks by allowing complex microscale geometries to be fashioned in planar substrates (**Table 1.1**). In the early 2000s, Vacanti and co-workers pioneered some of the first applications of these methods to produce microvascular topologies in silicon wafers, which subsequently served as rigid molds to imprint the patterned networks into biodegradable polymers like poly(lactic-co-glycolic acid) (PLGA)[2, 34, 35]. This process, typically referred to as *soft lithography*, involves the following basic sequence of steps: (1) spin coating photoresist onto the surface of clean silicon wafers, (2) patterning the photoresist by exposure to UV light through a photomask, (3) developing the pattern by exposure to a chemical that selectively removes the photoresist in areas exposed to the UV light, (4) etching the network pattern into the silicon substrate, and (5) stripping away the remaining photoresist. The resulting silicon wafer now contains a negative imprint of the desired microchannel pattern that then serves as a rigid mold or *master* against which a positive replica can be cast in the desired substrate material (in this case by pouring molten PLGA onto the surface and peeling it away after solidification). The patterned polymer is then bonded to a flat surface to create enclosed microchannels[36].

Table 1.1.Summary of literature reporting construction of 2D microvascular networks.

(Publications from the same laboratory are grouped together)

Channel cross-section	Channel size range	Micromachining method	Construction time	Substrate material(s)	Substrate size	Reference
rectangular	20-60 µm	electroforming	-	polycarbonate, poly lactide-coglycolides	1 x 2 cm^2	37
rectangular	20-60 µm	photoresist based molding	-	PMMA, PDMS	1 x 2 cm^2	38
circular	60-120 µm	photoresist based molding and bonding	-	PDMS	1 x 2 cm^2	39
rectangular	5-300 µm	micro-patterning	-	collagen-glycosaminoglycan membrane	1.7 mm thickness	40
rectangular	100 µm-5 mm	soft lithography	-	PDMS	1 x 2 cm^2	41
semi-circular	40-120 µm	wet etching	5 h	silicon	7.5 x 2.5 cm^2	42
rectangular	6-50 µm	soft lithography with sacrificial element	5 h	gelatin	85 cm^2	43
rectangular	45µm-3mm	soft lithography	~ 5 days	poly(glycerol sebacate)	3.8 x 7.5 x 0.1 cm^3	1
rectangular	10-500 µm	wet/plasma etching	-	silicon and Pyrex	10 cm^2	35
rectangular	35 µm-5 mm	lithographic and etching followed by soft lithography	4 h	PDMS	2 x 4 cm^2	44, 45
rectangular	-	wet/plasma etching	-	silicon mold/PLGA	5 x 5 cm^2	34
rectangular	50-1000 µm	soft lithography, molding agarose to wafer then sealing two layers of agarose together	-	agarose with or without cell encapsulation	1 cm thickness	46
rectangular	100 µm	soft lithography, injection of alginate and cells, sealing of hydrogel layers to form channels	-	calcium alginate hydrogel seeded with chondrocytes	1 x 1cm^2	47
rectangular	6-63 µm	soft lithography	-	PDMS	-	48
rectangular	267-727 µm	electric discharge machining of stainless steel mold, then soft lithography to cast in PDMS	-	PDMS	circle, 130 mm diameter	49
rectangular	20 µm-2.73 mm	micromachining of stainless steel mold then soft lithography to cast in PDMS	-	PDMS	5 x 5 cm^2	50
rectangular	1.197 mm	soft lithography	-	PDMS	2 x 2 cm^2	51
round	80-190 µm	electroplating of silicon master mold, then micro-patterning	-	polystyrene	1 x 3 cm^2	52
rectangular	50-400 µm	UV exposure to polymer through mask pattern	-	pCLLA acrylate	-	53

Table 1.1. Continued

Channel cross-section	Channel size range	Micromachining method	Construction time	Substrate material(s)	Substrate size	Reference
rectangular	125-660 µm	laser nanosecond ablation followed by chemical wet etching	-	silicon	1.5 cm	54, 55
semi-circular	50 µm-1 mm	laser ablation followed by chemical wet etching	8 h	silicon mold/ PDMS channel	1 cm	56
rectangular	90-600 µm hydraulic diameter	femtosecond laser ablation followed by chemical wet etching	5 h	silicon	3 x 6 cm^2	57
round	100 µm	inkjet printing of cells	-	fibrin	2 x 8 mm^2	58
rectangular	40-60 µm	hydrogel constructs cast from PDMS mold	-	alginate, collagen I, Matrigel I, fibrin	1 x 2 mm^2	59
round	< 10 µm or larger if co-cultured	laser guided direct writing	weeks, if co-culturing with hepatocytes	Matrigel, collagen	0.5 mm thickness	60

Variations of this basic soft lithography method have enabled microvascular-mimicking flow networks to be constructed in a variety of substrate materials suitable for cell culture. Poly(dimethyl siloxane) (PDMS) is one of the most widely used substrates owing to a number of favorable properties including optical transparency and gas permeability[44, 45], but more recent studies have explored a wider range of materials. For example, Fidkowski*et al.* synthesized a rubber-like biodegradable polymer, poly(glycerol sebacate) (PGS), and applied it to construct an endothelialized capillary network using human umbilical vein endothelial cells (HUVECs) (**Fig.1.1a**)[1]. A number of hydrogel substrates have also been investigated, including argarose[46], alginate (**Fig. 1.1b**)[47], and collagen/alginate (**Fig. 1.1c**)[59]. Ling*et al.* demonstrated that flow networks embedded in agarose can efficiently provide nutrient and waste exchange for surrounding cells[46]. Choi*et al.* investigated metabolite (e.g. calcein-AM) delivery in cell-seeded alginate hydrogels[47], while Gillette*etal.* demonstrated *in situ* collagen fiber

assembly in a cell-seeded hydrogel[59]. Additional complexity can be introduced by machining channels with variable depths, accomplished by processes such as laser machining into silicon followed by acid etching (**Fig.1.1d**)[54-57]. Although not fully three dimensional, the ability to vary the depth enables construction of networks with architectures that more closely follow the scalings predicted by Murray's law[61, 62]. Another novel approach was demonstrated by Cui and Boland, who constructed micron-sized fibrin channels using drop-on-demand polymerization implemented via an inkjet printing process, and subsequently demonstrated successful cell culture for up to 21 days in the resulting microchannel network (**Fig.1.1e**)[58].

1.2.3 Fabrication of 3D microvascular networks

Although vascularized microfluidic networks are readily produced in 2D by photolithographic or soft-lithographic techniques, comparable progress toward constructing 3D networks has occurred only recently (**Table 1.2**). This capability is of interest because it is generally recognized that 3D culture environments more closely replicate physiological conditions *in vitro* than 2D cultures. The simplest approach to generate 3D architectures involves stacking multiple 2D vascularized layers in a fluidically interconnected arrangement[2, 63, 64](**Fig. 1.2a-c**). For example, Bettinger*et al.* assembled five microfluidic layers constructed in a biodegradable substrate to create a 3D tissue culture scaffold, which was then seeded with a high density of HepG2 cells that formed aggregates throughout the microchannels[63].

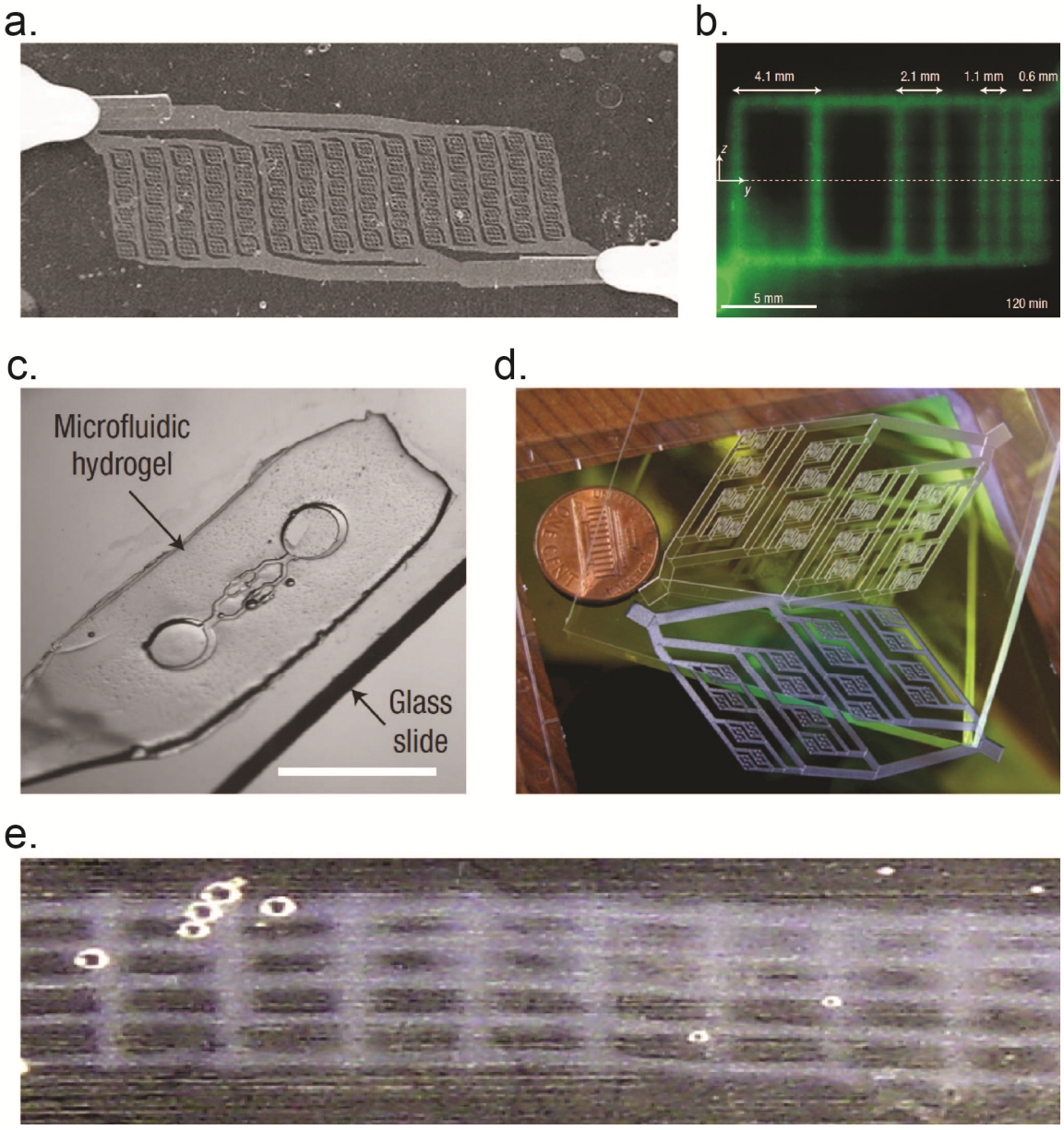

Figure 1.1.Construction of 2D microvascular networks. Soft lithography methods enable networks to be constructed in a variety of substrates including **(a)** PGS (reproduced with permission from reference[1]), **(b)** alginate (reproduced with permission from reference[47]), and **(c)** collagen/alginate (reproduced with permission from reference[59]). Other construction methods include **(d)** laser machining (reproduced with permission from reference[57]), and **(e)** inkjet printing (reproduced with permission from reference[58]).

The capacity for long-term viability was assessed by measuring albumin secretion rates. Kniazeva*et al.* employed a similar approach to construct individual blood-gas subunits that could be stacked together to form a microfluidic respiratory assist device to study gas permeance in artificial lung applications[64].

Lewis and coworkers have pioneered a novel approach involving direct writing of organic inks to create 3D microvascular networks in a Pluronic F127-diacrylate (DA) hydrogel[65] (**Fig. 1.2d**). In this approach, the ink is precisely dispensed using a fine nozzle positioned by a robotically controlled multi-axis stage so that 3D structures can be produced in a layer-by-layer fashion. After encapsulation in a desired substrate, the fugitive ink is liquefied and removed by application of a modest vacuum, leaving a microchannel network embedded in the surrounding matrix[66-70].

Other research projects have applied similar direct writing methods based on fusing multicellular spheroid aggregates containing various cell types (e.g. smooth muscle, fibroblasts) into tubular structures which serve as building blocks within a molding template (**Fig. 1.2e**)[71, 72]. Layer-by-layer deposition of these components permits the resulting tube diameter, wall thickness, and branching pattern to be accurately controlled. These scaffold-free constructs offer an alternative approach to enable tissue culture in expanded 3D volumes.

Table 1.2.Summary of literature reporting construction of 3D microvascular networks.

(Publications from the same laboratory are grouped together)

Channel cross-section	Channel size range	Micromachining method	Construction time	Substrate material(s)	Substrate size	Reference
varied	100 µm	soft lithography	-	PDMS	1 mm thick	73
rectangular	10 µm-1 cm	wet/plasma etching	-	silicon mold/PLGA	5 x 5 cm^2	2
rectangular	35 µm-5 mm	soft lithography	-	PDMS	3 x 3 x 5 cm^3	64
circular	0.9-2.5 mm	deposition of bioink particles into tubular structures using bioprinter	2-4 days	agarose		71
circular	varied	cell sheet engineering	3-7 days	NHDF and HUVEC sheets	60 µm	74
circular	30 µm	co-seeding HUVEC and 10 T1/2 precursor cells *in vivo*	up to 2 weeks	collagen gel	165 µm	75
circular	30-45 nm	culturing HUVEC on ionic self-assembling peptide gels	2 days	peptide gel	500 µm	76
varied	varied	modular assembly of HUVEC coated cylinders	3 days	collagen-HepG2 cylinders	0.57 mm diameter, 1.8 mm long	77
circular	230 µm	direct-write assembly	-	epoxy resin		66
circular	200 µm	direct-write assembly	-	epoxy resin	20 x 20 x 20 mm^3	67
circular	100-500 µm	direct-write assembly	-	epoxy resin	40 x 40 x 5 mm^3	68
circular	200-600 µm	direct-write assembly	-	Pluronic F127 diacrylate (F127-DA)	40 x 20 x 1 mm^3	65
rectangular	200 µm	direct-write assembly	-	epoxy resin	45 x 7 x 10 mm^3	69
circular	vertical: 100-410 µm	dual ink deposition and vertical ink writing	-	epoxy resin	50 x 12 x 6 mm^3	70
trapezoidal	200 µm	photolithographic and plasma-etching to produce silicon master	-	poly(glycerol sebacate)	10 x 5 x 1 mm^3	63
circular	1-100 µm	sacrificial sugar structures	-	polycaprolactone	1 x 2 x 0.5 cm^3	78, 79
rectangular	400 µm	layer by layer direct printing	-	collagen	5 x 5 x 1 mm^3	80
circular	10 µm-1 mm	electrostatic discharge	seconds	PMMA, PLA	25 x 10 x 10 mm^3	81
varied	15-20 µm	angiogenesis in three layers of fibroblast sheets *in vitro*	15-31 days	Fibroblasts, keratinocytes, HUVEC or HMVEC	3 x 3 cm^2	82, 83

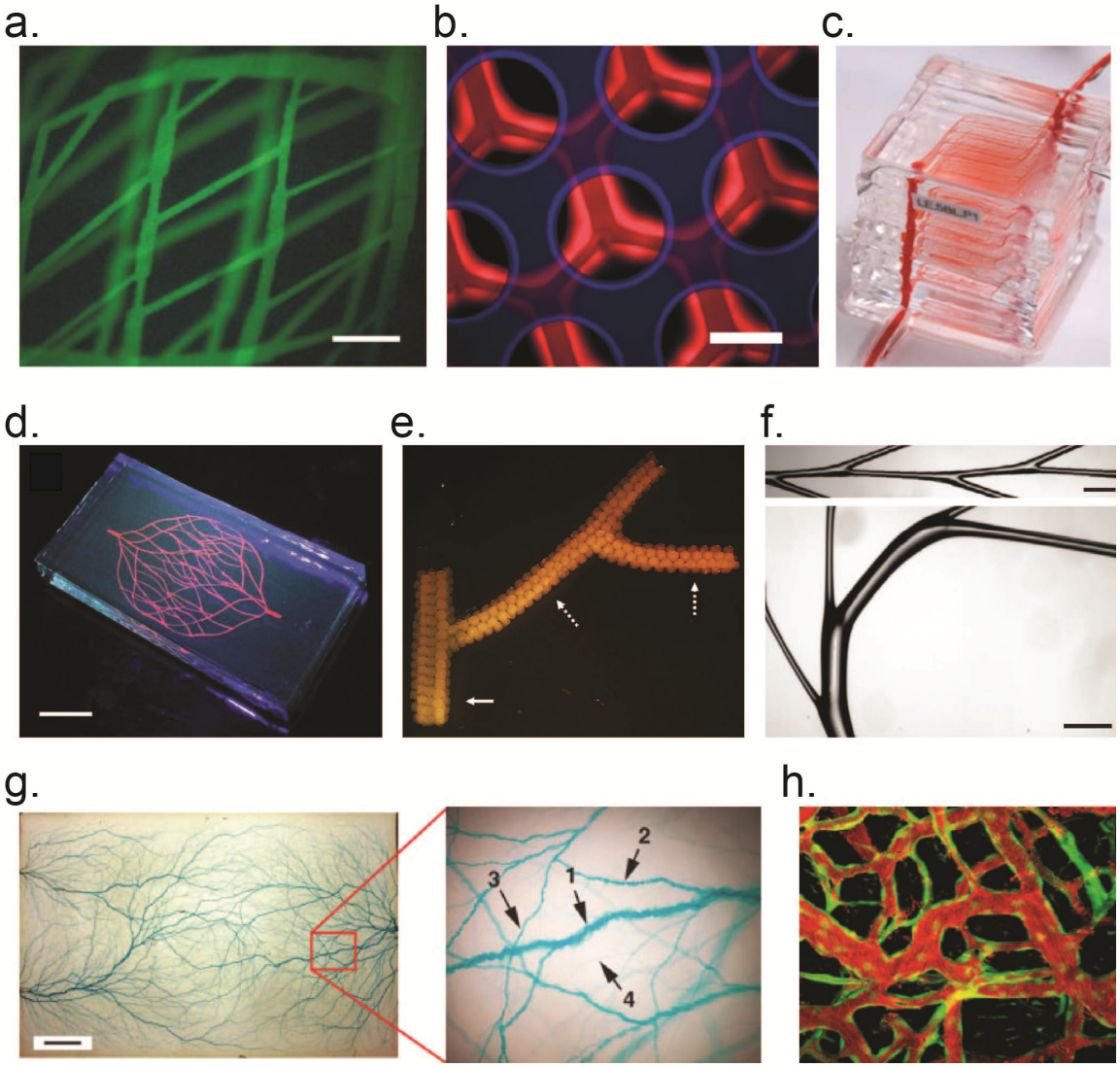

Figure 1.2.Construction of 3D microvascular networks.(a) Stacking of 2D PLGA-based micro-patterns (reproduced with permission from reference[2]). **(b)** Stacking of 2D PGS-based micro-patterns (reproduced with permission from reference[63]). **(c)** Stacking of 2D PDMS-based micro-patterns (reproduced with permission from reference[64]). **(d)** Embedding of vasculature within a Pluronic F127-based construct by direct-write assembly (reproduced with permission from reference[65]). **(e)** Deposition of bioink particles into tubular structures using a bioprinter (reproduced with permission from reference[71]). **(f)** Network constructed using a sacrificial sugar process (reproduced with permission from reference[78, 79]). **(g)** Tree-like branched network fabricated in PLA using electrostatic discharge (reproduced with permission from reference[81]). **(h)** Vasculogenesis by co-seeding HUVEC and 10 T1/2 precursor cells *in vivo* (reproduced with permission from reference[75]).

Sacrificial techniques have also been developed to construct microvascular networks. Golden and Tien demonstrated the ability to embed complex 2D networks within hydrogels by lithographic patterning of gelatin as a sacrificial element[43]. Lee*et al.* extended this concept into 3D by printing a heated gelatin solution between collagen layers[80]. A novel albeit unconventional approach was employed by embeddingmicrovascular networks within PDMS, epoxy, polycaprolactoneand other hydrogel matrices using melt-spun sugar fibers and carbohydrate glass as the sacrificial elements(**Fig. 1.2f**)[78, 79].

A key drawback associated with many of these methods is that the microchannels produced generally possess a relatively narrow range of diameters, rendering them less representative of physiologically relevant vascular systems where diameters become progressively smaller from the base to the tips of the branched network. One novel approach to mimic this architecture involves using electrostatic discharge (**Fig. 1.2g**)[81]. This process harnesses electron beam irradiation to implant a high level of electric charge inside an insulating polymeric substrate so that the energy released upon discharge will be sufficiently intense to locally vaporize and fracture the surrounding material. In this way, networks of highly branched tree-like microchannels with diameters ranging from approximately 10 μm to 1 mm are produced that become permanently embedded within the substrate. These networks incorporate branching characteristics quantitatively similar to naturally occurring vasculature, and have been successfully produced in both in both poly(methyl methacrylate) (PMMA) and biodegradable poly(lactic acid) (PLA) substrates.

In addition to manufacturing scaffolds with embedded vasculature, progress has also been made toward inducing formation of microvascular networks by directed differentiation of vascular endothelial cells and vascular progenitors (e.g. angioblasts), a process called *vasculogenesis*[84]. Although the resulting blood vessels sometimes become immature and unstable[85], Jain and coworkers have demonstrated the ability to produce a long-lasting blood vessel network (functional for one year) by co-culturing vascular endothelial cells and mesenchymal precursor cells (**Fig. 1.2h**)[75]. Finally, a promising approach based on decellularization of allogeneic or xenogeneic donor organs has been explored to reconstruct a variety of tissues including heart[86], liver[87], lung[88-90], and blood vessels[91]. The decellularization process yields an acellular3D scaffold directly replicating its natural counterpart that can subsequently be re-seeded with either functional parenchymal cells or selected progenitor cell populations. Initial results have shown promise, however, challenges associated with fibrosis of the *in vivo* cultured constructs after implantation as well as the need to rely on donor organs to provide a source for each decellularized construct still remain to be overcome.

1.2.4 Microchannel topologies

Ideally, microfluidic channels comprising vascular networks should incorporate circular cross-sectional profiles mimicking those in natural vasculature. But conventional lithographic and molding techniques are generally only capable of creating square, rectangular, or trapezoidal cross-sections. Despite these limitations, the ease with which 2D microchannel networks can be constructed using soft lithography has led it to

become one of the most widely used micromachining methods[1, 2, 34, 35, 44, 45]. Other approaches including electroforming[37], laser ablation[57], and sacrificial elements[43] have also been used to produce 2D branched networks with rectangular cross-sectional profiles. These studies have been proven useful to reveal key features associated with metabolite and oxygen exchange, waste dispersal, flow behavior, and extracellular matrix (ECM) formation that are critical to understand in order to undertake long term cell culture.

Despite these successes, however, the use of non-circular cross-sections for these studies poses challenges because the sharp corners are difficult to seed uniformly[92], making it difficult to form the confluent layers necessary to produce fully endothelialized networks. Moreover, wall shear stresses can vary widely across the width of microchannels with rectangular or trapezoidal cross-sections[93], as well as in the vicinity of flow obstructions[94]. Since these local shear stresses play an important role in governing functional phenotype and gene expression in endothelial cells[95-97], the extent to which experiments using these geometries faithfully replicate the physiological microenvironment must be considered.

Other area where microfluidic networks have provided useful insights is in studies investigating blood clotting phenomena (both in initial[98] and propagation[99] phases) that contribute to venous and arterial thrombosis according to Virchow's triad describing venous thrombosis in terms of an interplay among effects related to (1) vessel wall damage, (2) blood flow changes, and (3) alterations in the blood's fluidic characteristics[100].

Recent advances in micromachining technology have made it possible to construct semi-circular topologies by applying methods such as photoresist-based molding[39], wet etching[42], electroplated molding[52], laser ablation[56], and micromilling[101]. Microchannels with circular cross-sections are then constructed by aligning two substrates imprinted with complementary semi-circular patterns and bonding them together. Direct-ink writing methods have also been employed to construct 3D branched networks with circular cross-sectional profiles in hydrogel matrices[65]. The electrostatic discharge method also shows promise to enable 3D networks with circular cross-section topologies to be embedded in larger substrates[81].

In addition to the cross-sectional profile of individual microchannels, the branching architecture of the global network should match that of the physiological system of interest (**Table 1.3**). This can be accomplished by applying Murray's law to determine hierarchy of changes in diameter that should be experienced by microchannels entering and exiting each branch point. These concepts have been applied to design and construct branched microvascular networks in both 2D[42, 49, 50, 54-57, 102] and 3D[64, 68, 81]. But while providing an important guide, Murray's law is not the only consideration because in reality the wall shear stress (WSS) values display variability in physiological systems depending on the particular location within the flow network. For example, mean WSS values were found to range on average between 1.1 – 1.4 Pa in the common carotid artery, whereas values in the 0.5 – 5.0 Pa range are found in arterioles larger than 15 μm in diameter. In smaller arterioles (capillaries) in the 6 μm range, WSS values above 10 Pa can occur owing to non-regulatory properties of mesenteric arterioles[103]. These kinds

of local variations, coupled with realistic flow conditions (**Table 1.4**) must be incorporated into the design of artificial vascular networks in order to ensure that physiological conditions are reproduced.

Table 1.3.Summary of literature reporting construction of branched microvascular networks.
(Publications from the same laboratory are grouped together)

Channel cross-section	Channel size range	Micromachining method	Based on Murray's law?	Spatial geometry	Reference
square	35 µm-5 mm	lithography and etching followed by soft lithography	No	2D	1, 2, 34, 35, 44, 45
rectangular	1.197 mm	soft lithography	No	2D	51
square, rectangular, or trapezoid	44.2-250 µm	simulation	Yes	2D	55, 102
rectangular	125-660 µm	laser ablation followed by chemical wet etching	Yes	2D	54
rectangular	> 50 µm	simulation	No	2D	104
rectangular	100 µm-5 mm	soft lithography	No	2D	41
rectangular	20 µm-2.73 mm	micromachining of stainless steel mold, then soft lithography to cast in PDMS	Yes	2D	49, 50
circular	80-190 µm	electroplating of silicon master mold, then micro-patterning	No	2D	52
rectangular	40-60 µm	hydrogel constructs cast from PDMS mold	No	2D	59
semi-circular	40-120 µm	wet etching	Yes	2D	42
rectangular	20-60 µm	electroforming	No	2D	37
circular	60-120 µm	photoresist based molding and bonding	No	2D	39
semi-circular	50 µm-1 mm	laser ablation followed by chemical wet etching	Yes	2D	56
rectangular	90-600 µm	laser ablation followed by chemical wet etching	Yes	2D	57
rectangular	6-50 µm	soft lithography with sacrificial element	No	2D	43
rectangular	35 µm-5 mm	soft lithography	Yes	3D	64
circular	100-500 µm	direct-write assembly	Yes	3D	68
circular	200-600 µm	direct-write assembly	No	3D	65
circular	10 µm-1 mm	electrostatic discharge	Yes	3D	81

Table 1.4. Characteristic flow properties in blood vessels under human physiological conditions[105].

	Artery	Arteriole	capillary	Venule	Vein
Diameter (μm)	4,000	30	6	20	5,000
Average flow rate (mL/s)	1.3	4×10^{-6}	8×10^{-9}	9×10^{-7}	1.0
Mean pressure (mm Hg)	90	60	25	15	12

1.2.5 Engineering meets biology: toward tissue engineering and bio-MEMS applications

Construction of microvascular networks, while important, is only one piece of a much broader puzzle that must be solved in order to artificially manufacture complex tissues. These insights have been developed through extensive studies dating back to Weinberg and Bell's pioneering demonstration of the first *in vivo* tissue-engineered blood vessels in 1986, cultured from a combination of bovine endothelial cells, smooth muscle cells, and fibroblasts[106]. Through these efforts, it is now generally appreciated that organ-sized artificial tissues require (1) an embedded vascular network to sustain transport of nutrients and waste, (2) a three dimensional matrix to support cell seeding and culture, and (3) incorporation of appropriate cell types into the construct.

The range of cell types that need to be incorporated into functional tissues is illustrated by considering the case of capillaries, the most abundant blood vessels, consisting of endothelial cells (ECs) surrounded by basement membrane (composed of sheet-like depositions of extracellular matrix (ECM) material) and a sparse layer of pericytes (a type of perivascular cell found in small vessels) embedded within the EC basement membrane (**Fig. 1.3a**).

The main function of capillaries is to exchange the nutrients and waste between blood and tissue cells by utilizing their specific wall geometry and large contact surface. Precapillary arterioles are completely surrounded with vascular smooth muscle cells (SMCs) and their own basement membrane are formed associated with the circumferentially arranged, closely packed, and tightly endothelium. By gradually coverage of mural cells on capillaries, arterioles and venules are eventually formed. More complex structures can also include fibroblasts, precursor cells able to synthesize ECM material[107].

The role of vascularization can now be appreciated in the context of a general strategy to construct organ-sized artificial tissues *in vitro*. Ordinarily, the process of vasculogenesis begins to unfold upon cell seeding when the ECM environment coupled with hypoxia (low oxygen) experienced by the cells stimulates endogenous release of angiogenic growth factors responsible for growth of new blood vessels. Unfortunately, this spontaneous vasculaturization process occurs too slowly to supply the seeded cells with adequate oxygen and nutrients during the time needed for a mature network to form[108]. Furthermore, it is not yet fully understood how to direct the process so that well-defined interconnected branched networks are produced. These obstacles can be overcome by incorporating embedded 3D vasculature within the scaffold to both provide transport of nutrients and waste throughout the cell-seeded scaffold, and act as a template for construction of artificial vasculature by seeding the interior of the microchannels with endothelial cells. These embedded networks should incorporate a branched architecture containing small arteries (1 – 2 mm diameter) leading into an

arteriolar network (100 – 1000 μm diameter), and terminating in capillary-like vascular bed (10 – 15 μm diameter). This network should in turn be surrounded by a matrix that functions as a reservoir to deliver growth factors (e.g. vascular endothelial growth factor (VEGF)), and a scaffold that serves as a temporary ECM (**Fig. 1.3b**; in tissue engineering applications, ECM materials are generally classified into two groups: (1) natural biodegradable polymers that are inherently biodegradable, non-immunogenic and biocompatible, and (2) synthetic biodegradable polymers with controllable mechanical properties and crosslinkable functional groups). The resulting scaffold can then be seeded with appropriate cell types (e.g., adult stem cells derived from the patient) whose differentiation could be orchestrated to produce mature blood vessels and ultimately functional tissue.

1.3 Isolation of Circulating Tumor Cells

There is currently a critical need for advanced filtration methods adaptable for separation of cells and cell-sized components from blood samples, specifically offering the capability to rapidly process large sample volumes (> mL/min flow rates). One example of this need can be found in efforts to develop technologies to enable rapid separation of blood components (red blood cells, platelets, plasma) in a portable format. Current blood bank procedures generally involve tedious and labor intensive manual steps combined with bulky centrifugation-based instruments that are typically single component separators, are the size of an ice chest, and can weigh as much as 30 – 60 lbs.

Collection of a standard blood unit can be performed in 20 minutes, but a blood bank laboratory is required for processing the components. Microfluidic technologies provide a natural platform to address these challenges, but these efforts have yet to advance past the proof of concept stage to show that it is possible to rapidly and reliably deliver blood components that meet the American Association of Blood Bank standards (i.e., low hemolysis of red blood cells, high percent of purity of each component, normal platelet function parameters, sterility, etc).

Another key area where high-throughput separation of blood cell-sized components is important is in analysis of disease biomarkers relevant to cancer. In 2010, approximately 1.53 million Americans were diagnosed with cancer and about 570,000 died of the disease. An estimated $263.8 billion will be spent on health care costs for cancer according to American Cancer Society and National Cancer Institute. But despite decades of research, the 5-year survival rates of cancer patients are still increasing (50% in 1975 to 68% in 2007). Circulating tumor cells (CTCs) refer to a class of epithelial cells that are released either from a primary tumor or its metastases and are subsequently transported throughout the peripheral blood circulatory system. CTCs have emerged as an area of intense research interest because of their potential to play an important role in cancer diagnostics (i.e., to provide early detection of metastasis) and early detection[109, 110]. Isolation of CTCs, however, poses daunting technical challenges because their occurrence in the bloodstream is extremely rare (of order 1 in 10^6 to 10^9 blood cells)[111]. Thus, availability of a convenient platform to monitor CTC levels (i.e., spreading of cancer cells from organ to organ through blood stream) would provide a new and

powerful method to assess the efficacy of cancer treatments so that personalized "on the fly" adjustments could be made during the course of therapy.

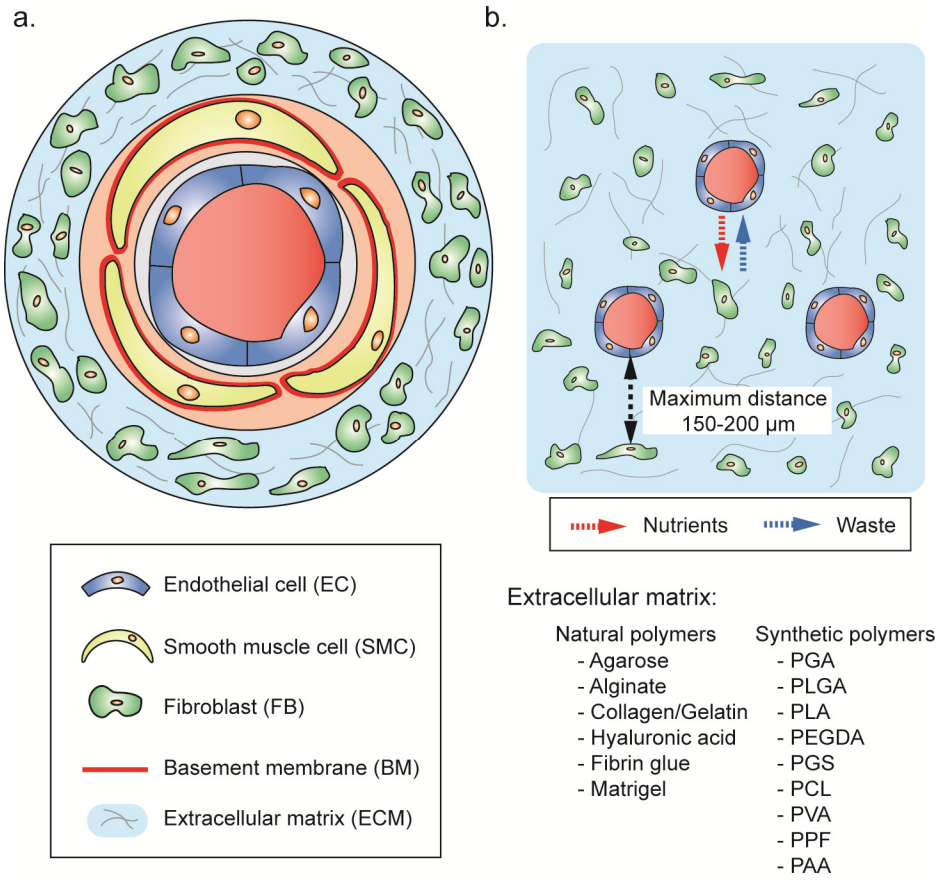

Figure 1.3.Cellular composition of blood vessels. (a) The walls of larger vessels consist of three major cellular layers: endothelial cells, smooth muscle cells surrounded by basement membrane, and fibroblasts incorporated with extracellular matrix. **(b)** Artificial ECM materials can be broadly classified into natural and synthetic polymers. Mass transport between cells and the nutrient blood flow source is conducted within the ECM, but cells can survive by diffusion alone only if they are located within about 150 – 200 µm of a vascular element.

1.3.1 Current methods

Current methods for CTC analysis suffer from a number of drawbacks that have prevented their use as a routine diagnostic tool (**Table 1.5**). Traditional isolation and enrichment methods involve density gradient centrifugation. However, the density difference between CTCs and other blood cells is very small, resulting in the need to perform additional immunostaining steps. The stained samples must be examined by a trained pathologist, introducing a tedious and time consuming manual process. Maximum CTC recovery rates are also fairly low (~70%). Immunomagnetic separation methods have also been employed for CTC isolation. Here, antibody functionalized magnetic beads are used to capture CTCs, after which they can be isolated and enriched. Capture efficiencies are generally improved over centrifugation-based approaches, but these methods are costly and limited due to the need to supply antibodies specific to the desired target. Membrane-based methods have also been employed to separate CTCs based on their size difference versus other blood cells (~15-20 μm versus 10 μm or less for other blood cells). But success of these methods critically depends on obtaining membranes with near-monodisperse pore sizes in the correct range. The membranes are also mechanically fragile and subject to clogging, limiting the flow rates that can be applied.

Table 1.5.Overview of existing CTC enrichment methods.

CTC enrichment method	Ref	System	Sample vol. (ml)	CTC recovery	Flow rate	Analysis time	Drawbacks
Centrifugation	112	Oncoquick®	10-30	25-70%		40 min	**Additional sample prep and bench work needed**
	113	Oncoquick®	15-35	62-75%		45 min	
	112	Ficoll	10	1-2%		30 min	
Immuno-magnetic separation	114	EPCAM-coated ferrofluid	10-20	75-100%		~ 1 h	**Expensive, additional sample prep and bench work needed**
	115-117	MACS	7.5-10	83 %		2 h	
	118	CellSearch®	7.5	>1/7.5 mL		40 min/300 µl	
Immuno-selection	119	Antibody coated microposts	2.7	65-80 %	1-2 mL/h	1-2 h	**Too slow to process large volumes for detection at low concentrations**
	120	Antibody coated microchannel	> 1	10-250 / mL		~ 35 min	
Dielectro-phoresis	121	Dielectro-phoretic flow fractionation	0.25- 4.5	90%	1.5 mL/min	20 min	**Special ionic buffer conditions**
Size-based separation	122-124	ISET	10	>1/10 mL		10 min	**Cell concentration must be diluted to avoid clogging, various additional sample preparation steps needed**
	125	Pool-dam			0.1 mL/min		
	126	Membrane filter	9	0.2-5.7 / mL		2 min	
	127	Membrane filter	1			10 min	
	128	Isolation wells	1.7	80%	0.7 mL/h	2.5 h	
	129	Micropost array			0.3 mL/min		
	130	Micropost array			1 mL/h		

These challenges have motivated interest in exploring microfluidic-based approaches for CTC isolation and enrichment (**Fig. 1.4**). Many of these methods are based on constructing micromachined filtration structures that act either alone to provide size-selective isolation or in combination with functionalized antibodies to provide affinity capture. Although previous work in this area has demonstrated the potential of these microdevices to provide enhancements in CTC analysis[131], they still suffer from limitations inherent to the filtration-based design. Most notably, the achievable flow rates are typically very small due to the large pressures that must be applied to force the cell suspension to flow through the tiny pore networks present. Consequently, the cell suspensions usually must be diluted prior to analysis (making it necessary to process even greater volumes due to the rare nature of CTCs), and the large internal shear stresses prevent recovery of viable cells unless extremely low flow rates are used (further increasing the analysis time)[131]. These problems with existing methods point to a need for development of filtration approaches capable of isolating CTCs (1) at high flow rates, (2) with no clogging and (3) preserving cell viability.

1.3.2 Size-based filtration

Size-based filtration is a nearly ideal candidate to separate and enrich CTCs which are well-known to be larger in size than normal leukocytes and erythrocytes[132-135]. These size differences can be very dramatic in many clinically relevant examples. For example, Meng*et al.* found that from those patients' blood diagnosis with breast cancer the mean diameter of tumor cells ranges from ~30-34 μm[134]. A further relevant example

is found in the work of Vona*et al.* who used size-based isolation to obtain epithelial tumor cells (ISET) from patients with liver cancer, and found characteristic sizes to be in the range of ~40-42 μm[136].

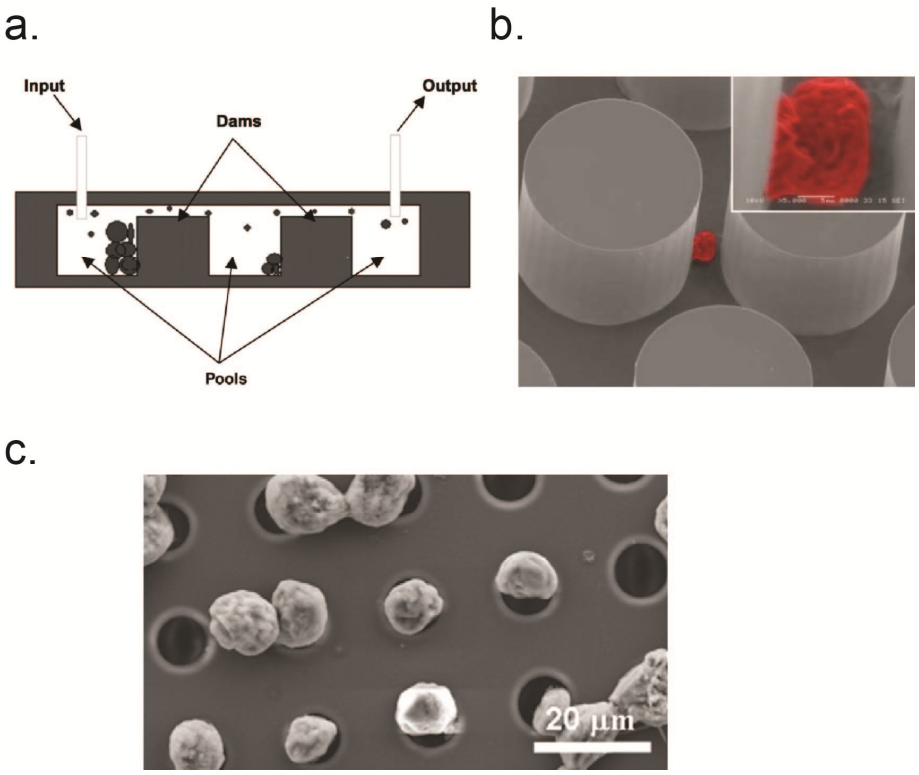

Figure 1.4. Overview of previous microfluidic CTC filtration designs. **(a)** "pool-dam" structures based on alternating deep and narrow channel segments (reproduced with permission from reference[125]), **(b)** arrays of antibody functionalized posts (reproduced with permission from reference[119]), and **(c)** etched porous membranes (reproduced with permission from reference[127]). All of these are restricted to low flow rate operation and permit only limited recovery of viable cells.

Another important point is that metastatic tumor cells do not individually shed from primary tumors as signalmesenchymal-like cells and invade through nearby blood or lymph vessel walls. In fact, these malignant tumor cells may also invade surrounding normal tissues in the form of cell clusters or multicellular aggregates in a process known as ‘‘cohort’’ or ‘‘collective’’ migration[137]. Recent studies investigated that these tumor cell clusters, much larger in size than any other blood components, can attach to and rupture vessel walls of arterioles and capillaries andprovidefurther advantages for tumor cell survival, proliferation, and formation of small tumor known as micrometastasesin distant organs[138, 139]. Thus, it is generally accepted that the presence of circulating tumor cell clusters, easily distinguishable by filtration methods, can be viewed as a diagnosis marker of highly metastatic potential[138-142]

The “pool-dam” structuresshown in **Fig. 1.4a**[125]operate in a specific design (i.e., by imposing a physical obstacle that restricts the flow of larger sized components in the fluid), but placement of the barriers perpendicular to the flow direction makes the pool-dam arrangement highly susceptible to clogging and introduces large pressure drops that limit achievable flow rates (especially if recovery of viable cells is desired). Nevertheless, successful separation of SPA-C-1 CTCs from whole blood samples was demonstrated using the pool-dam configuration, thereby validating the underlying principle of the physical separation mechanism. Taken together, these considerations suggest that a size-based filtration approach can provide a highly effective tool for isolation and enrichment of CTCs.

1.3.3 Compared to conventional affinity-based methods

To further illustrate the benefits of a size-based separation approach, the CellSearch® assay based on immuno-magnetic antibody enrichment, the first CTC-based system to receive FDA approval for monitoring patients with metastatic breast, colorectal, and prostate cancers is compared. Although the assay is effective, results can be inconsistent due to the inherent need to rely solely on affinity interactions. In the case of breast cancer, for example, the frequency of Ep-CAM expression can vary over a fairly wide range (i.e., from ~35 to 100%)[143-146]. It has also proven challenging to identify antibodies that are highly specific to CTCs (i.e.,epithelial antigens expressed not only by all types of invasive tumor cells but also expressed by leukocytes or by other circulating non-tumor cells)[109]. Moreover, the majority of antibodies currently employed are limited to selection of cancer cells expressing epithelial antigens. Consequently, anti-cytokeratin antibodyhas been reported to show specific and non-specificbinding to macrophages, plasma cells and nucleated hematopoietic cell precursors to generate a false-positive result[147, 148]. Finally, even if highly specific antibodies are identified, the affinity-based approach inherently limits the ability to detect other circulating tumor cells or "rare cells" (e.g., trophoblastic, endothelial progenitor[149] and stem cells) for which specific antibodies have not yet been developed. The significance of these drawbacks is evident by the fact that the American Society of Clinical Oncology does not currently recommend the use of CTC measurements for diagnostic or treatment decision making[150]. These limitations offer a compelling argument against the

conventional affinity-based approach for CTC analysis, and point to the need for more general (i.e., size-based) isolation/enrichment methods.

1.4 Organization of the Dissertation

In Chapter II, the experimental procedures are provided that show how to fabricate microvascular networks in different types of materials and construct complex topologies via a novel approach. In Chapter III, the fabrication process of tree-like microvascular networks is reported along with an analysis of their branching characteristics. In Chapter IV, the improved fabrication methods are demonstrated and show the abilities to mimic the similar geometry of a natural microvascular network. In Chapter V, the construction methods and mechanism of enzymatic micro- and nano-fabrication are described. In Chapter VI, the mechanism and application of membraneless microfluidic filter are discussed. Finally, the conclusions of my dissertation are summarized in Chapter VII.

CHAPTER II

EXPERIMENTAL PROCEDURES

2.1 Block Sample Preparation

Polished acrylic rectangular blocks (1x3x3 inch) and cylindrical rods (1.5 inch dia., 4.5 inch long) were purchased from Trio Display (San Diego, CA). Polished blocks are desirable when constructing discharge networks using the grounded contact method because they reduce nucleation of unwanted spontaneous discharges that may occur due to surface imperfections. Rectangular blocks of poly(lactic acid) were thermally molded from pelletized resin (NatureWorks grade 3051; Jamplast Inc., Ellisville, MO). Pellets were loaded into molds constructed from poly(dimethyl siloxane) and heated to 180 °C under vacuum for 2 h, after which the vacuum was released and heating continued for an additional hour. The mold was then removed from the oven and cooled at room temperature so that the PLA blocks (1.5x5x8 cm) could be easily released.

2.2 Electrostatic Discharge

Experiments were performed at the National Center for Electron Beam Research at Texas A&M University. This system employs a 15 kW linear accelerator to produce a single 10 MeV electron beam directed upward from below the sample. The energy of the incident beam was attenuated using three sheets of 5 mm thick high-density polyethylene (HDPE) to achieve the target dose at the desired depth inside the substrate. An estimate of the maximum penetration depth was obtained using CSDA range data at

10 MeV provided in the NIST ESTAR Database of Stopping Powers and Ranges for Electrons (physics.nist.gov/PhysRefData/Star/Text/ ESTAR.html). Applying these parameters ($R_{CSDA,PMMA}$ = 5.158 g cm^{-2}, ρ_{PMMA} = 1.19 g cm^{-3}; $R_{CSDA,HDPE}$ = 4.833 g cm^{-2}, ρ_{HDPE} = 0.957 g cm^{-3}) yields average penetration depths of 4.33 and 4.06 cm in PMMA and HDPE respectively. For light particles like electrons, the CSDA range represents a maximum upper-limit value of the actual penetration depth (experimental data place the peak dose at R_{PMMA} ~ 2.8 – 3 g cm^{-2})[151]. that is useful to determine the attenuation needed to maximize the implanted charge. The substrate and attenuating sheets were mounted on a cardboard carrier tray and transported though the electron beam by a conveyor at a speed of 10 ft min^{-1}. Microchannel networks formed by spontaneous discharge became embedded inside the substrate immediately upon exposure to the beam (holes of approximately 1 mm diameter were drilled to a depth of about 1 cm, tapering to a point near the bottom of the hole; we did not observe a strong effect of hole size on the features of the resulting network, but this was not systematically investigated). In the grounded contact method, irradiated substrates were discharged using a hammer to strike the surface with a sharp-tipped metal tool (e.g., a nail or needle) connected to a grounded cable.

2.3 Flow Analysis

Interconnectivity and flow within the vascular networks were quantified by injecting an aqueous solution of blue food dye using a syringe pump at flow rate of 0.1 µl min^{-1}. Volumetric imaging of the microvascular networks was performed using a

Leica TCS SP5 Confocal microscope (scan speed 400 Hz) to scan blocks injected with Rhodamine B dye (Sigma-Aldrich). Image stack data were then assembled into 3D reconstructions. Instrument limitations (e.g., acquisition times of several hours) restricted the allowable imaging volume to a small subregion of the overall network.

2.4 Image Analysis

Branching characteristics were quantified by using photographic images of the networks acquired along the midplane of each block (**Fig. 2.1**) as a basis to render digital reconstructions using *Neuromantic* software (www.rdg.ac.uk/neuromantic/), after which the software package *L-Measure* (cng.gmu.edu:8080/Lm/pdfs/lmhomepg.jsp) was used to extract quantitative parameters. Fractal dimension calculations were performed using *Fractalyse* analysis software (fractalyse.org/en-home.html). All software packages are freely available.

2.5 PLA Substrate Preparation

Smooth planar substrates were obtained by placing pelletized PLA resin (MW = 1.04 x 10^5 g/mol, NatureWorks, grade 3051D; Jamplast Inc.) directly onto glass microscope slides. A silane pre-treatment was applied to enable easy release of the PLA film by exposing the slides to tridecafluoro-1,1,2,2-tetrahydrooctyltrichlorosilane vapor (SIT8174.0; Gelest Inc.) inside a dessicator for at least 2 h at room temperature. The glass slides containing the PLA pellets were heated to 180 °C under vacuum for 1 h, followed by an additional 1 h of heating after the vacuum was released. The slides were

then cooled at room temperature for 1 h, after which the PLA film could be easily peeled away.

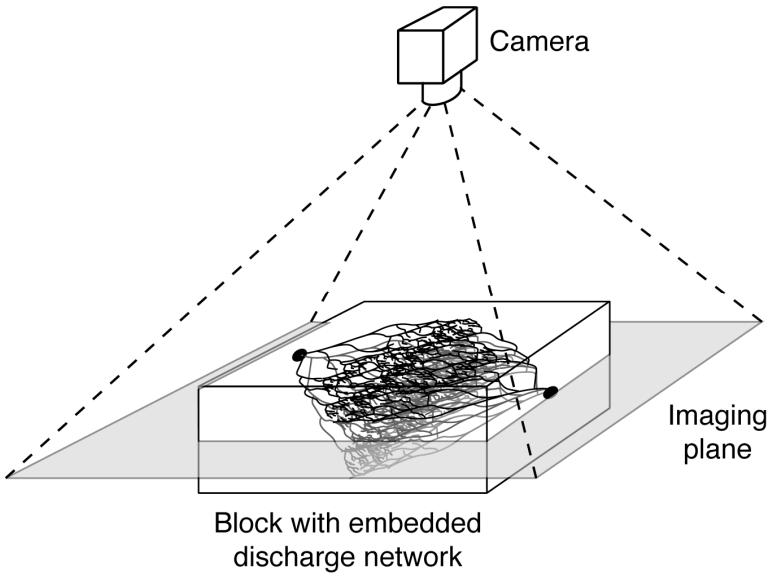

Figure 2.1.Illustration of image acquisition. Quantitative analysis of the network morphology presented in Fig. 3.5 and Table 3.1. 2D projections of the discharge network were collected by aligning the focal plane of the camera approximately along the midplane of the block. These images were then used to reconstruct the network using the software described in the paper.

2.6 Patterned PLA Substrate Preparation

Reversepatterns were photolithographically defined using a mask printed on transparency film at 65,024 dpi. The resulting photoresist structures were then used as master molds to replicate the reverse microchannel patterns in PDMS (Sylgard 184; Dow Corning) prepared using a 10:1 degassed mixture of prepolymer and curing agent. After curing for 2 h at 80 °C, the cooled PDMS slab was peeled from the master mold as a soft elastomer template. This PDMS mold containing reverse microchannel patterns was rinsed with 2-propanol (Fisher Scientific), dried in a stream of compressed air. Microchannel patterned PLA plate can be constructed by directly placing pelletized PLA resin (MW = 1.04 x 10^5 g/mol, NatureWorks, grade 3051D; Jamplast Inc.) onto PDMS mold and heating to 180 °C for 1 h under vacuum, followed by another 1 h at atmospheric pressure and then cooled at room temperature for 1 h(**Fig. 2.2**). After peeling from PDMS mold, the fluidic access ports on PLA microchannel were drilled with a 1/32 inch bit. Smooth planar substrates were obtained by placing pelletized PLA resin directly onto glass microscope slides. A silane pre-treatment was applied to enable easy release of the PLA film by exposing the slides to tridecafluoro-1,1,2,2-tetrahydrooctyltrichlorosilane vapor (SIT8174.0; Gelest Inc.) inside a dessicator for at least 2 h at room temperature. The glass slides containing the PLA pellets were heated to 180 °C under vacuum for 1 h, followed by an additional 1 h of heating after the vacuum was released. The slides were then cooled at room temperature for 1 h, after which the PLA film could be easily peeled away. Both the microchannel patterned and flat PLA plates were rinsed with 2-propanol followed by DI water and dried with compressed air.

Enclosed microchannels were fabricated by directly placing the patterned PLA replica on the flat PLA plate and heated at 80 °C for 20 min. Tygon tubing (0.03 inch O.D.) was inserted into the access ports and sealed with epoxy glue to obtain interconnect fluidic channels.

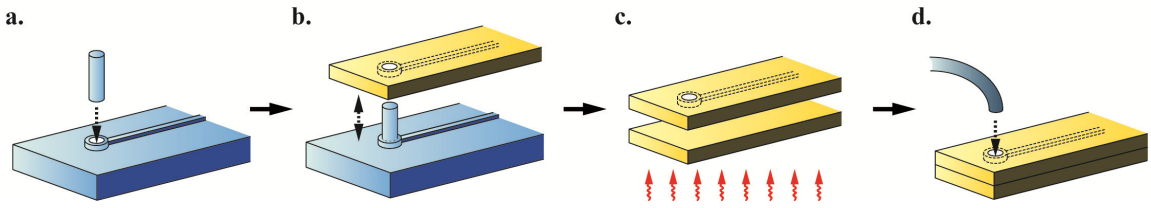

Figure 2.2. Schematic of fabrication enclosed PLA microhannels with fluidic access ports (see also in Fig. 6.7). **(a)** A PDMS mold containing reverse patterns was obtained from demolding of etched PLA or patterned SU-8 silicon wafer. This mold was punched with a blunt needle and inserted with a pillar shape PDMS. **(b)** After melting process, patterned PLA plate was peeled from PDMS mold. **(c)** Enclosed microchannels can be fabricated by thermal bonding with another flat PLA substrate. **(d)** PLA device embedded with patterned microchannel was constructed by inserting Tygon tubing and sealing with epoxy glue.

2.7 Air Deformation Process

The enclosed PLA substrate embedded with microchannels and connected with tygon tubing was coupled with pneumatic drive system consisting of compressed air, pressure regulator and pressure gauge to control and monitor the desire pressure. Connected PLA substrate then can be stored in temperature controllable vacuum oven (VWR 1415M, West Chester, PA) for desire polymer softening temperature condition. The process was stopped by closing pressure valve and removing the PLA substrate from the oven to cool down at room temperature. The contraction effect of molten PLA after stopping process can be ignored because of low mold shrinkage value of PLA (0.004 in/in, provided by NatureWorks® Co.).

2.8 Computational Fluid Dynamics (CFD) Analysis

2.8.1 COMSOL Multiphysics

A 3D computational model was formulated using COMSOL Multiphysics (version 4.0a, COMSOL, Inc.) The laminar flow and viscoelastic material models were selected from COMOSL's model library to simulate geometry change of channel, and two-dimensional convection-diffusion mode was selected to numerically evaluate mass transport model. The computational domain was discretized into a mesh of quadrilateral elements.Properties of water at 37 °C (ρ = 993.36 kg/m^3, μ = 6.9 x 10^{-4}Pa·s) were used to represent all solutions (proteinase K, buffer, BSA). Diffusion coefficients for proteinase K, BSA, and PK-BSA complex were estimated to be 1.22 x 10^{-6}, 9.25 x 10^{-7}, and 8.2 x 10^{-7} cm^2/s, respectively based on their molecular weight (T = 37 °C)[152].

2.8.2 STAR-CCM+ (CD-adapco)

A 3D computational model was formulated using STAR-CCM+ (CD-adapco) meshed using a nonuniform grid containing 212,992 cells. Water was used as the fluid with properties at room temperature. A flow rate of 1 mL/min was imposed on each side of the centerline barrier as the inlet boundary condition, with a flow-split boundary condition at the outlet. Particle transport was assessed by simulated injection of 3 μm diameter beads randomly distributed throughout the cross-section along the inner flow path. Lagrangian tracking was applied to dynamically map the particle positions as they traveled through the microchannel. A Schiller-Naumann drag coefficient was applied to calculate the drag force on the particles, and elastic wall interactions were imposed.

2.9 PLA Based MicrovascularNetwork Scaffold

(1) Seven layers of patterned branched network. Seven pieces of patterned PLA microchannel and one piece of flat PLA plates were rinsed with 2-propanol followed by DI water and dried with compressed air. All layers of PLA sheet were thermally bonded at 80 °C for 20 min to form an enclosed flow network at the same time. Tygon tubing (0.03 inch O.D.) was inserted into the access ports and sealed with epoxy glue to obtain interconnected fluidic channels. **(2) Electrostatic discharged vascular network.** Rectangular blocks of PLA were thermally molded from pelletized resin by using the substrate preparation method above.Experiments were performed at the National Center for Electron Beam Research at TexasA&M University. The substrate and 1.5 cm of HDPE (high-density polyethylene) attenuating sheets were

mounted on a cardboard carrier tray and transported though the 10 MeV electron beam by a conveyor at a speed of 10 ft/min. Microchannel networks formed by spontaneous discharge became embedded inside the substrate immediately upon exposure to the beam (holes of 1 mm diameter were drilled to a depth of about 1 cm, tapering to a point near the bottom of the hole[81]. **(3) Porogen embedded scaffold.** The pelletized PLA resins (2 g) were dissolved in chloroform solvent (10 mL) and mixed with 90 % w/w sieved sodium chloride (250-420 µm with #40 and #60 sieves from McMaster-Carr) as porogen to yield moldable slurry mixture. The mixture then was placed and compacted into hollow Teflon mold (5 mm in diameter and 5 mm in height) and air dried in fume hood for overnight. The solidified polymer/porogen disc-like scaffolds were removed from mold and soaked with 2-propanol for 2 h to replace solvent following by air dried again for overnight to completely vaporized remain solvent. The scaffolds were stored in a vacuum desiccator for later use. PLA patches contained high concentration porogen were fabricated by directly placing polymer/porogen disc-like scaffolds into melted PLA and cooled down at room temperature. Molded PLA patches were electrostatic discharged by using the method mentioned above to create vascular branched networks.

2.10 Cell Culture in PLA Channel

Circular PLA microchannels were coated with 25 µg/mL of fibronectin (BD Biosciences) followed by incubating in 37°C, 5% CO_2 incubator for 1 h to facilitate the cell attachment. The channels were then rinsed with DMEM medium (SAFC Biosciences) contained 10% FBS (Thermo Science) and 1% penicillin-streptomycin).

Bovine Aortic Endothelial Cells (BAECs) were prepared at 5 x 10^6 cells/mL medium for 500 µm channel or 2 x10^7 cells/mL medium for 100 µm and branched channel. After inoculating cell suspension into the channel, the microchannels were put into the incubator for 2 h to allow cells attach well. The devices were refreshed with medium and then reseed with cells, rotated by 120° and again placed into the incubator for another 2 h. This step was repeated one or two more times to let cell confluence in the circular channel. After completion of seeding procedure, attached cells were stain with 25 µM of CellTracker Green CMFDA (Invitrogen) and incubated for 1 h to trace live cells. For long term cell culture, the microchannels within PLA substrate were connected with a computer controlled micropump system and flushed with continuous circulating medium at flow rate of 0.5 µL/min. Cell viability was monitored and imaged under fluorescence microscopy (Axiovert 200M, Carl Zeiss MicroImaging, Inc.).

2.11 Microfluidic Etching Template

Microchannels were fabricated in poly(dimethyl siloxane) (PDMS) using soft lithography[36]. Briefly, master molds were constructed using SU-8 2050 photoresist (Microchem) applied to a 35 mm silicon wafer by spin coating at 3,200 rpm for 60 s, yielding a 50 µm thick layer. Patterns were photolithographically defined using a mask printed on transparency film at 20,320 dpi. The resulting photoresist structures were then used as master molds to replicate the microchannel patterns in PDMS (Sylgard 184; Dow Corning) prepared using a 10:1 degassed mixture of prepolymer and curing agent. After curing for 2 h at 80 °C, the cooled PDMS slab was peeled from the master mold

and fluidic access ports were punched with a 22 gauge blunt-end needle. The microchannels were rinsed with 2-propanol (Fisher Scientific), dried in a stream of compressed air, and directly adhered to the flat surface of a PLA substrate to produce enclosed channel networks. Tygon tubing (0.03 inch O.D.; Small parts Inc.) was inserted into the access ports, and the entire assembly was clamped between two acrylic sheets to ensure a tight seal.

2.12 Enzymatic Etching

Aqueous solutions of proteinase K (MW = 28.9 kDa; BP1700, Fisher Scientific) and BSA (MW = 66.4 kDa; A2153, Sigma-Aldrich) were prepared in 30 mMTris-HCl buffer (pH 8.0, BP1758; Fisher Scientific). An etchant concentration of [PK] = 6.92 μM (0.2 mg/mL) was used in most experiments. Prior to etching, the PDMS microfluidic template was thoroughly rinsed with DI water. A syringe pump (PHD 2000; Harvard Apparatus) was connected, and the entire assembly was placed inside an incubator while the etching solutions (enzyme, BSA, buffer) were continuously pumped though the network at 37 °C. After etching was completed, the PDMS template was removed from the PLA substrate and the resulting patterns were washed using 2-propanol following by DI water to stop the enzymatic reaction. The etched channel depths were measured using a Dektak 3 stylus profilometer (Veeco Instruments). Surface topologies were imaged using a JEOL JSM-6400 scanning electron microscope, post processed with NanoScope Analysis software (v1.4; Bruker Corp).

Nanochannels were etched using a microchannel with 3 inlets to co-inject a central stream of PK with BSA solution on each side (2 µL/min each stream) into a tapered microchannel for 3 h at room temperature (25 °C). The BSA sheath flows focused the PK stream to confine etching within a ~ 4 µm wide zone in the narrow constriction region of the microfluidic template. Nanochannel topologies were characterized using a Nanoscope III atomic force microscope (Digital Instruments; Santa Barbara, CA) and post processed with SPIP software (Image Metrology, Denmark).

2.13 Flow Visualization

Images of the flow field inside the microchannels were obtained using a Zeiss Axiovert 200M fluorescence microscope. Brightfield images of co-injected food dye streams were used to visualize the interface under different flow conditions. Diffusive transport of BSA was observed using FITC-BSA (A9771; Sigma-Aldrich). Images were acquired using Zeiss AxioVision Software version 4.8 with a FITC filter set.

2.14 Membraneless Filtration Device

The etching process described above was first applied to construct the microchannel geometry in PLA, after which the etched PLA was used as a template to construct a PDMS mold. The fluidic access ports on PDMS mold were punched with a 20 gauge blunt-end needle and inserted with a pillar shape PDMS (1/32 inch in diameter) fixed with PDMS mixture. This PDMS mold, containing a reverse imprint of the etched pattern, was then used repeatedly to produce additional microchannels in PLA

(**Fig. 2.3**). Enclosed microchannels were then constructed by thermally bonding the PLA replica to a flat PLA substrate molded using glass slides as described above. Both the microchannel and flat substrate were rinsed with 2-propanol followed by DI water and dried with compressed air. The PLA replica was directly placed on the flat PLA substrate and heated at 80 °C for 20 min. Tygon tubing (0.03 inch O.D.) was inserted into the access ports and sealed with epoxy glue. Aqueous suspensions of fluorescent polystyrene latex microbeads (3 and 10 μm diameter; Catalog numbers 17155 and 17156; Polysciences, Inc.) were diluted to 1.68 x 10^6 and 4.55 x 10^4 particles/mL, respectively and injected into the inner inlet of the filtration device while water was infused through the outer inlet. The separated microbeads were observed using an Olympus SZX12 stereoscope with fluorescence illuminator and CCD-300 camera (DAGE-MTI).

2.15 Blood Cell Separations

Human prostate cancer cell line PC3 obtained from ATCC (Manassas, VA) was maintained in RPMI 1640 medium (Sigma-Aldrich) supplemented with 10 % fetal bovine serum (Hyclone), 100 U/mL penicillin, and 100 μg/mL streptomycin (Sigma-Aldrich) at 37°C under a humidified 5% CO_2. PC3 cells were then stained with CellTracker Red CMTPX (Invitrogen) and spiked into fresh human blood (K2 EDTA anticoagulant) obtained from Bioreclamation Inc. The ratio of blood cells and PC3 cells were adjusted by addition of phosphate buffered saline solution (Fisher Scientific) to achieve equal amount of WBCs and PC3 cells. Cell counts were obtained using a

Multisizer 3 Coulter counter (Beckman Coulter). Erythrocytes were lysed with Zap-oglobin II lytic reagent (Beckman Coulter) for determination of leukocyte and cancer cell counts. Pure PC3 cells were also counted as a control to determine their size distribution profile. Cells numbers are expressed with respect to the total collected sample volume.

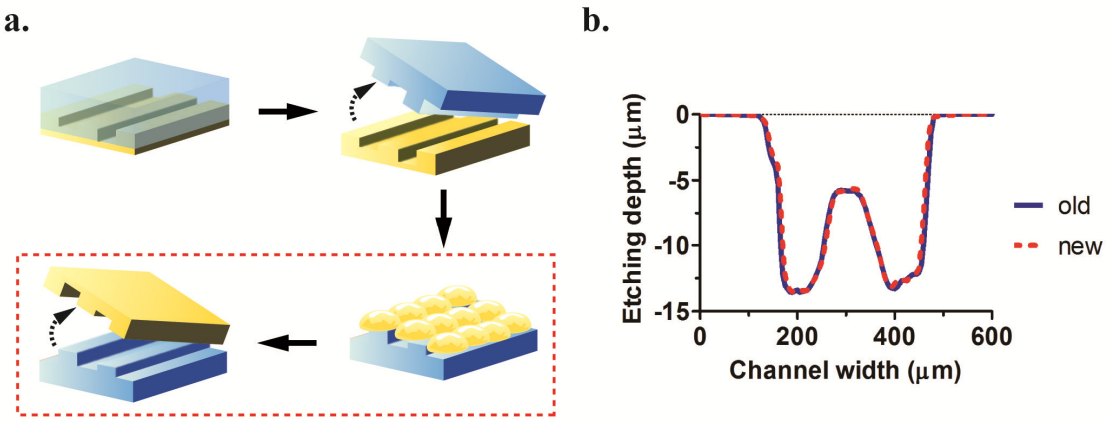

Figure 2.3.Reproducible hot-molding process.**(a)** A replica mold is made by casting PDMS elastomer directly onto etched PLA channels. The curing temperature of PDMS should not exceed the glass transition temperature of PLA (60 – 65 °C) to avoid deformation of the etched structures. After curing for 2 h at 50 °C, the PLA substrate can be peeled from the mold leaving the reverse pattern imprinted in PDMS. The solidified PDMS is then further cured for 1 h at 80 °C. The original etched PLA substrate can be used to make multiple PDMS molds. Once the inverse pattern is replicated in PDMS, microchannels are constructed by placing PLA resin in the mold and heating to 180 °C for 1 h under vacuum, followed by another 1 h at atmospheric pressure and by cooling at room temperature for 1 h. **(b)**Profilometry data show that the molded microchannels identically replicate features of the original etched substrate.

2.16 Imprinting of Crystalline Morphologies

PLA substrates with different crystalline morphologies were obtained by placing pelletized resin directly onto planar PDMS slabs that could be easily separated after molding. The pellets were melted at 180 °C under vacuum for 1 h, followed by an additional 1 h of heating after the vacuum was released. The PLA was then annealed under different conditions (e.g., 70 °C for 8 h, 80 °C for 1h, 120 °C for 1h), removed from the oven, and cooled to room temperature (25 °C) in the ambient environment. The crystalline morphologies were observed with an optical microscope (Zeiss Axiovert 200M).

CHAPTER III

RAPID FABRICATION OF BIO-INSPIRED 3D MICROFLUIDIC VASCULAR NETWORKS*

3.1 Introduction

Living systems face a fundamental challenge of orchestratingexchange of nutrients and oxygen throughout 3D space in orderto satisfy their metabolic needs[8]. In nature, vascular networkshave evolved to elegantly address this problem by incorporatinghighly branched fractal-like architectures that are efficientlyspace-filling while minimizing the energy required to sustain transport[20, 21]. The ability to mimic these features *in vitro* would beimmensely beneficial in the field of tissue engineering, wherediffusion limitations generally restrict the maximum thickness ofconstructs to a few hundred microns[12, 16, 153].In this chapter, we address thisneed by introducing a nearly instantaneous method to embedbranched 3D microvascular networks inside plastic materials. Inthis microfabrication process, a high level of electric charge is firstimplanted inside a polymer dielectric using electron beamirradiation. The accumulated energy is then discharged in acontrolled manner to locally vaporize and fracture the material,leaving behind a network of branched microchannels arranged ina tree-like architecture with diameters ranging from 10 μm to1mm.

---

*Part of the data reported in this chapter is reprinted with permission from: Rapid Fabrication of Bio-inspired 3D Microfluidic Vascular Networks by Huang, J.H. et al..*Advanced Materials***21**, 3567-3571 (2009).©2009 by WILEY-VCH Verlag GmbH & Co. KGaA, Weinheim.

Modulating the irradiation profile and discharge locationsallows the networks' morphology and interconnectivity to beprecisely tailored. Interconnected networks with multiple fluidicaccess points can be straightforwardly constructed, and quantificationof their branching characteristics reveals remarkablesimilarity to naturally occurring vasculature. This method can beapplied in a variety of polymers, and may help enable productionof organ-sized tissue scaffolds containing embedded vasculature.

3.2 Limitation

The hierarchy of length scales that comprise vascular networks(ranging from μm–mm in diameter) and the need for thesestructures to be widely accessible throughout a sizeable 3Dvolume present significant manufacturing challenges. Photolithography-based microfabrication technology has been extensivelyexamined as a potential avenue to address some of theseissues[34, 37, 39, 41, 48, 104, 154, 155] Here, planar micromachining is harnessed toproduce 2D microchannel arrays that can be stacked in alayer-by-layer fashion to achieve a limited degree of three dimensionality[156]. But assembly of large-scale multi-tiered structures is tedious, and the inherently planar nature of the individual layers restricts the network's topological complexity.More recent developments have enabled fully 3D flow architectures to be produced using methods including solid freeform fabrication, stereolithography, and direct printing[42, 60, 66, 153]. But these approaches generally involve time consuming serial processes, and the optimal range of feature sizes associated with each technology is often relatively narrow. These methods only provide a coarse approximation of microvascular structure, and no single technique

has proven ideal for use over the entire range of length scales associated with a whole-tissue vascular network. Most of these processes are also challenging to scale up toward levels feasible for mass production[157].

3.3 Electrostatic Discharge

We have developed a fabrication method that uniquelyovercomes these limitations, enabling branched 3D microvascularnetworks incorporating a wide range of microchanneldiameters to be rapidly constructed in a variety of plastic materials (**Fig. 3.1**). This process harnesses electron beam irradiation to implant a high level of electric charge inside a substrate so that theenergy released upon discharge will be sufficiently intense to locally vaporize and fracture the surrounding material. In this way, networks of highly branched tree-like microchannels are produced that become permanently embedded within the substrate. The formation and growth of these electrostatic discharge structures (i.e., Lichtenberg figures or Lichtenberg trees) are analogous to lightning phenomena that occur during thunderstorms when charge accumulation within clouds exceeds the breakdown potential of the surrounding atmosphere[158-160].

We first explored applying this process to construct 3D vascular microchannel networks in acrylic plastic substrates by irradiating blocks of polished poly(methyl methacrylate) (PMMA) using a 10MeVelectron beam to implant a prescribed charge distribution (typical space charge densities are on the order of 1 $\mu C/cm^2$)[160], after which the energized blocks were discharged by one of two methods. In the first approach (**Fig. 3.1a**), release of the accumulated charge was achieved by striking the irradiated block

with the sharp tip of a grounded electrode. The point source of electrical grounding and the mechanical stress associated with the physical impact of striking the block combine to produce an immediate and rapid energy release[159]. Alternatively, a defect (e.g., a small hole ~1mm in diameter) was intentionally introduced on the surface of the block prior to irradiation.Upon exposure to the electron beam this depthserved as a nucleation site for spontaneous discharge without the need for further physical contact (**Fig.3.1b**). In either case, the rapid and intense release of electrostatic energy instantaneously generated a hierarchically branched microchannel array penetrating throughout the entire volume of the block and originating from either the point of contact with the grounded electrode or the nucleationsite created on the surface (**Fig. 3.1c**). Networks formed using the grounded contact methodgenerally incorporate more tree-like architectures consisting of awell-defined central trunk several mm in diameter with progressively finer branches extending outward, while spontaneous discharge yields microchannels that are more randomly dispersed throughout the substrate (e.g., see photos in **Fig. 3.1a and b**).

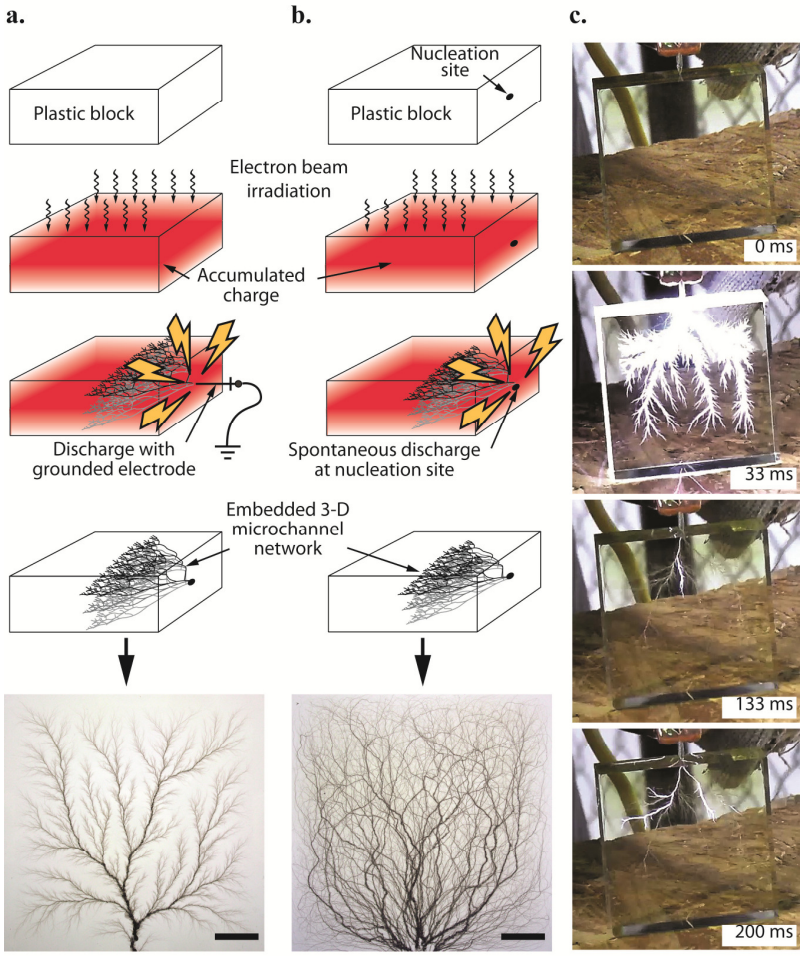

Figure 3.1. Harnessing electrostatic discharge phenomena to rapidly construct branched 3D microvascular networks. **(a)** In the grounded contact method, electron beam irradiation is used to implant a high level of internal electric charge inside a dielectric substrate. A grounded electrode is then brought into contact with the substrate surface, initiating sudden energy release that locally vaporizes the surrounding material leaving behind a tree-like branched microchannel network. **(b)** In the spontaneous discharge method, a defect (e.g., small hole) is first created on the substrate surface prior to irradiation. When the internal electric charge exceeds a critical level upon exposure to the electron beam, the defect acts as a nucleation site for spontaneous energy release. The grounded contact method yields a more "tree-like" morphology while microchannels produced by spontaneous discharge permeate the substrate more uniformly. **(c)** Image sequence from a video recording of discharge by grounded contact shows that energy release is nearly instantaneous with subsequent weaker discharges persisting over longer timescales. All photographs depict microchannel networks in 1x3x3 inch polished acrylic blocks. Note that all networks extend in 3D throughout the volume of the blocks. Scale bars, 1 cm.

The morphology and branching characteristics of the microchannelnetworks are largely dictated by the magnitude and distribution of accumulated charge inside the substrate prior to discharge. This level of accumulation is in turn determined by an interplay between 1) the penetration depth (range) of the impinging electrons and 2) the time of exposure to the incidentbeam (dose). Penetration depth profiles inabsorbing media reflect the distribution ofcomplex and tortuous paths traveled by incident electrons, and can be inferred using a combination of experimental dose distribution data[151] and penetration range calculations based on the continuous slowing down approximation (CSDA)[161]. The CSDA analysis predicts a maximum penetration depth of4.3 cm for PMMA, implying that mostelectrons would pass through the 2.54 cm thick acrylic blocks and yield little or no charge accumulation. Since the beam energy is fixed, we controlled the penetration depth by inserting polyethylene attenuators into the beam path to ensure that a majority of the incident electrons became implanted inside the PMMA blocks. Exposure dose from the continuous irradiation source was controlled by adjusting the speed of a conveyor that transported the blocks through the beam. We found that a speed of 10 ft/min (1 ft = 0.3048 m) permitted sufficient charge accumulation. Faster speeds resulted in weak discharges thatgenerated tiny thread-like microchannels whileslower speeds yielded regions where locally violent discharges produced large globule-like features that obscured the underlying branched network morphology (**Fig. 3.2**). Proper selection of penetration depth and irradiation dose enabled us to reproducibly achieve a high level of control over the microchannel network architectures constructedusing electrostatic discharge.

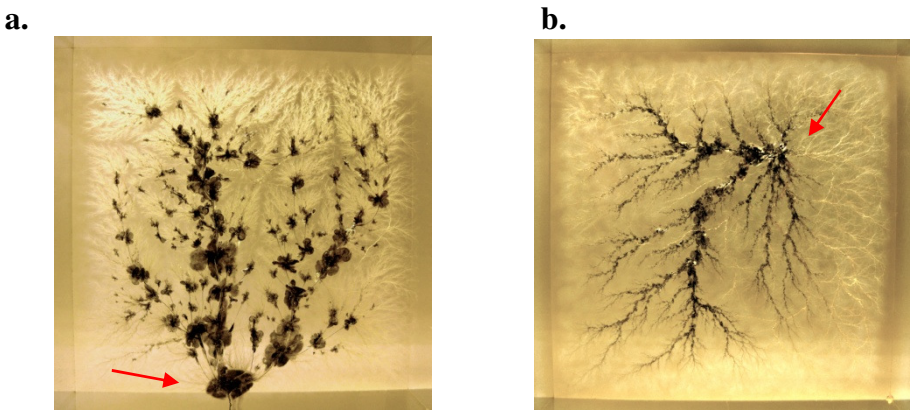

Figure 3.2.Microchannels with globule-like features.(a),(b) Photographs depicting two examples of microchannel networks implanted in 1x3x3 inch polished acrylic blocks using the grounded contact method (arrows denote discharge locations). In both cases a level of charge higher than normal was implanted inside the block prior to discharge, leading to locally violent energy release that produced large globule-like regions that obscured and interfered with the underlying branched network morphology.

3.4 Flow Visualization

Flow-through perfusion capabilities necessarily require interconnected networks possessing multiple access points for inlet and outlet streams. These architectures can be straightforwardly constructed using a multi-stepprocess whereby an initial discharge networkis first implanted using either of the methods illustrated in **Fig.3.1**, after which the substrate is re-irradiated by the electron beam one or more additional times in order to nucleate further discharges. These secondary spontaneously generated microchannels originate from nucleation sites defined by positioning one or more small holes at desired locations along perimeter of the block, and naturally become interconnected with the network already embedded inside the substrate (**Fig. 3.3a**). The location of each nucleation site and the number of irradiation/discharge cycles can be adjusted to

manipulate the size, morphology, and density of the resulting microchannelnetwork (**Fig. 3.3b–e**). Each discharge nucleation site provides an independent access point for fluid injection or collection. Flow and interconnectivity can be directly observed by introducing tracer dye solutions using a syringe pump to permit visualization, both in 2D by recording images of a subset of the network occupying a specific focal plane (**Fig. 3.4a**), and in 3D by usingconfocal laser scanning microscopy (**Fig. 3.4b**). Analysis of these images reveals a fractal-likemicrochannel architecture incorporating a hierarchy of diameters ranging from 500 μm at the ‘‘trunk’’ of the tree structure to10 μm near the tips of the outermost branches. Some of themicrochannels incorporate dead ends, mostly at the highest levels of branching (i.e., the tips of the branches), yielding anarchitecture analogous to a capillary bed where the smallest ducts at the ends of the network may not be physically interconnected but are densely arrayed to facilitate diffusive transport between neighboring branches.

We also wanted to determine whether electrostatic discharge could be harnessed to embed branched vascular networks in biodegradable substrate materials relevant for tissue engineering by testing the process using thermally molded blocks of poly(lactic acid) (PLA). Here, we used the spontaneous discharge approach (**Fig. 3.1b**) to define the network’s point of origin by creating nucleation sites at specific surface locations (**Fig. 3.4c**).We find that electrostatic discharge is robustly applicable to PLA substrates, with interconnected networks possessing channel diameters comparable to but within a slightly narrower range than those formed in the acrylic blocks (300 μm at the trunk to

20 μm near the tips), likely reflecting differences in dielectric properties between materials.

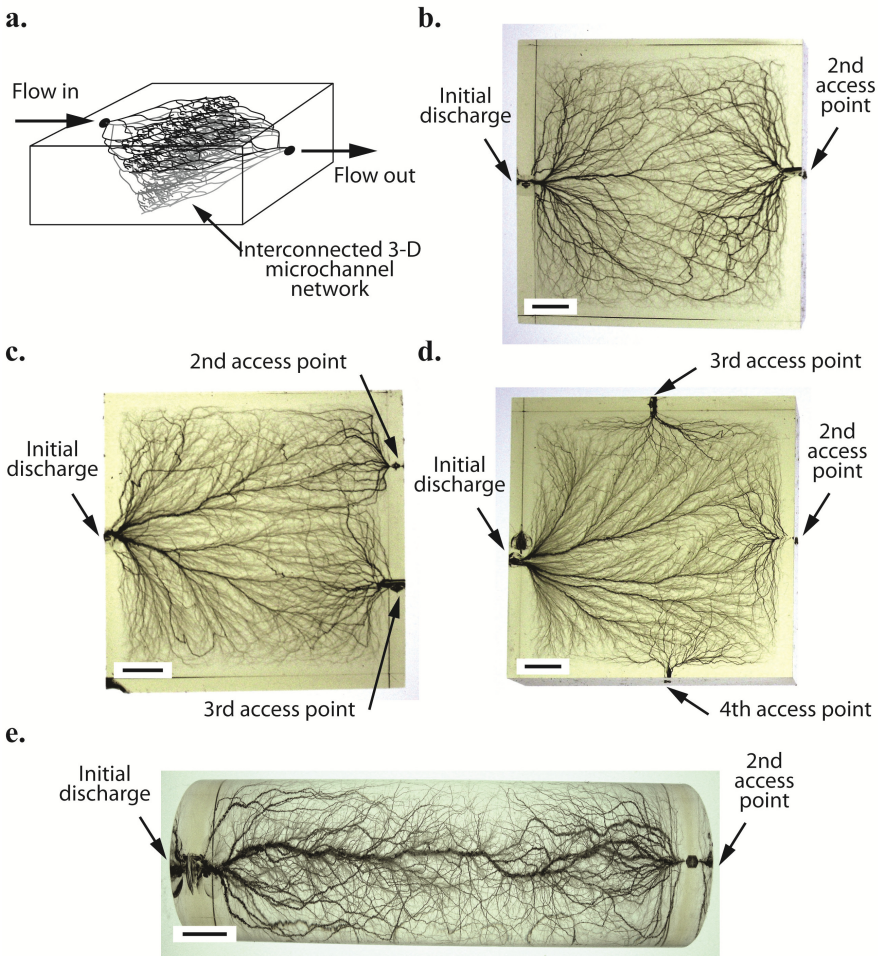

Figure 3.3. Interconnected branched microvascular networks with multiple fluidic access points. **(a)** A single branched microchannel network is first constructed using either of the methods described in Fig. 3.1. One or more additional nucleation sites are then created on the surface and the block is re-irradiated to initiate further spontaneous discharges originating at each site. Microchannel networks created in 1x3x3 inch polished acrylic blocks **(b-d)** and a 1.5 inch dia., 4.5 inch long polished acrylic rod **(e)** become interconnected during the subsequent irradiation/discharge steps providing multiple locations for fluidic injection and collection. The extent of branching in the embedded networks are progressively increased by the additional irradiation/discharge cycles. Scale bars, 1 cm.

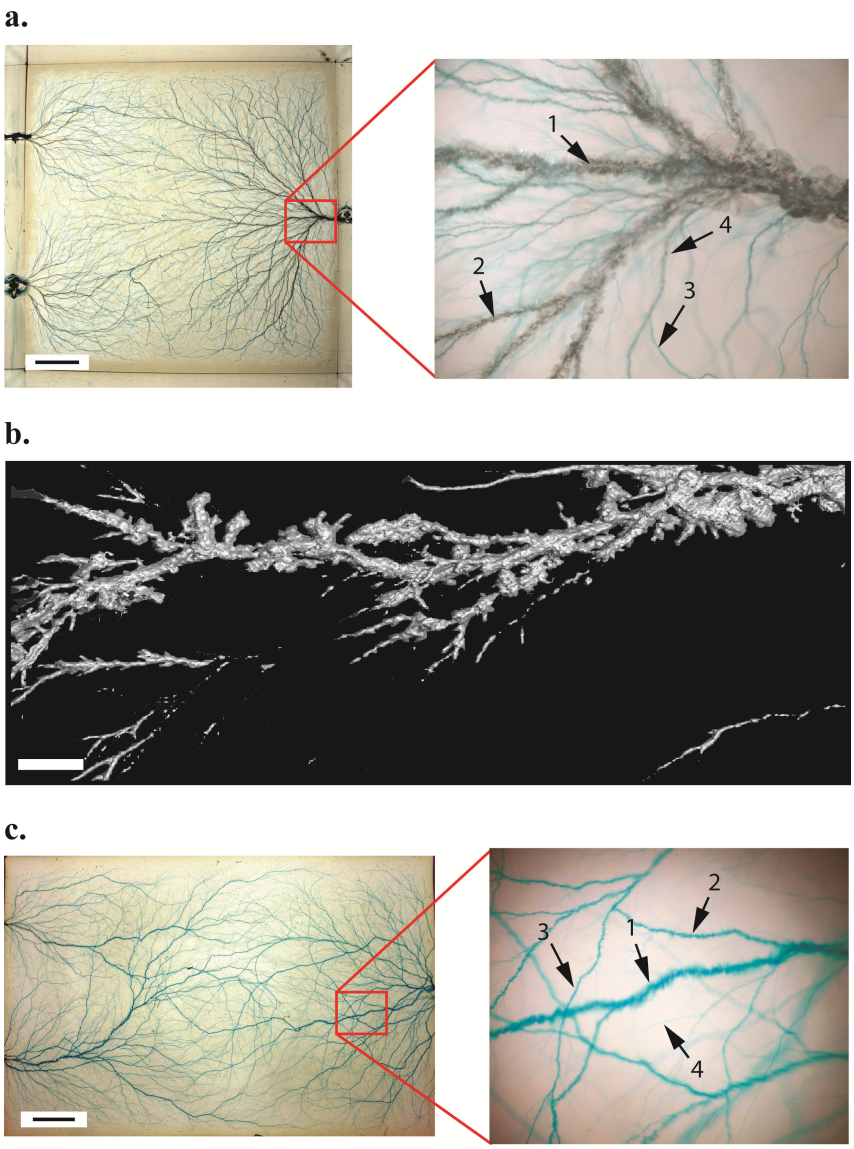

Figure 3.4.Branched microvascular networks embedded in acrylic and PLA substrates incorporate a hierarchy of microchannel diameters. **(a)** Injecting an aqueous solution of blue food dye into an interconnected microchannel array in a 1x3x3 inch polished acrylic block with three fluidic access points enables direct visualization of the flow network (scale bar, 1 cm). A close-up view reveals the tree-like microvascular hierarchy (point 1: 350 µm; point 2: 90 µm; point 3: 45 µm; point 4: 10 µm dia.). **(b)** 3D confocal microscope scan of a branched microvascular network embedded in acrylic loaded with Rhodamine B dye. These data reveal the general features of the network morphology and confirm the ability to pump liquids through the microchannels. Scale bar, 1 mm. **(c)** Branched microvascular network embedded in a 1.5x5x8 cm molded PLA block ((scale bar, 0.5 cm; point 1: 180 µm; point 2: 70 µm; point 3: 40 µm; point 4: 20 µm dia.).

3.5 MicrovascularNetwork Morphology

Microchannels produced by electrostatic discharge mimic many attributes of naturally occurring vasculature where a well-defined global architecture persists despite the fact that no two networks are completely identical at all structural levels. The extent of this self-similarity becomes evident when we compare the branching characteristics of microchannel networks produced in three identical acrylic blocks exposed todifferent irradiation and discharge conditions (**Fig. 3.5**).Discharge networks were first embedded in each block using the grounded contact method (**Fig. 3.1a**). The blocks were then exposed to additional cycles of re-irradiation and spontaneous discharge, during which the embedded branched network continued to grow and expand[159].Quantitative descriptors of the corresponding network morphologies based on consideration of a bifurcation model where a parent channel of diameter d_0 splits intotwo daughter channels of diameters d_1 and d_2(**Fig. 3.5a**)were then extracted from analysis of images acquiredalong the midplane of each block. Multiple branchesoriginating from exactly the same point (trifurcations, etc.) were rarely observed. Remarkably, these data indicate that although the network density increases with each subsequent irradiation/discharge cycle, the average bifurcation angle and fractal dimension remain relatively unchanged and within physiological ranges observed in living systems (**Table 3.1**)[162-164]. These results demonstrate that all three networks share a fundamentally similar underlying architecture despite clear differences in network density. A more detailed picture was obtained by examining the variation in the ratio between the parent and daughter cross-sectional areas (area ratio) and the bifurcation index (**Fig. 3.5b–d**). These data show that

the network comprises a distribution of bifurcations ranging from symmetric ($d_2/d_1 = 1$) to asymmetric ($d_2/d_1<1$) that are not only self-similar among all three blocks, but also mirror the features of physiologically relevant vasculature[165].

The architecture of naturally occurring vascular networks isoften described in terms of Murray's law[61], a model based onenergy minimization arguments that predicts a system-wide state of uniform shear stress corresponds to a global scaling of flow rate with the cube of vessel diameter[20, 21, 55]. Considering the case of bifurcations from a parent channel to two daughter channels, Murray's law implies that $d_0^k = d_1^k + d_2^k$ where a value of $k = 3$ is predicted under ideal conditions (e.g., laminar, non-pulsatileflow). Analysis of the branched networks in **Fig.3.5** yield exponents in the vicinity of $2.1<k<2.3$ (**Table 3.1**), within the range of available physiological data (deviations from $k = 3$ are common and attributable to departures from the idealized flow conditions assumed in the formulation of Murray's law)[29, 30, 164, 166, 167].Furthermore, it is notable that the physics of electrostatic discharge phenomena yield networks whose scaling exponents naturally approach $k = 2$ owing to the requirement for the minimization of electrical resistance[168]. Optimal networks for diffusive mass transport inherently share this $k = 3$ scaling(consistent with physiological observations indicating a transition from $k = 2$ in larger vessels near the base of arterial trees to $k = 3$in the capillary beds[28]), an observation further supported byfractal dimension values in the vicinity of 1.8[169]. These data imply that branched microchannels constructed using electrostatic discharge inherently possess morphologies ideally suited to satisfy the transport requirements of tissue engineering applications.

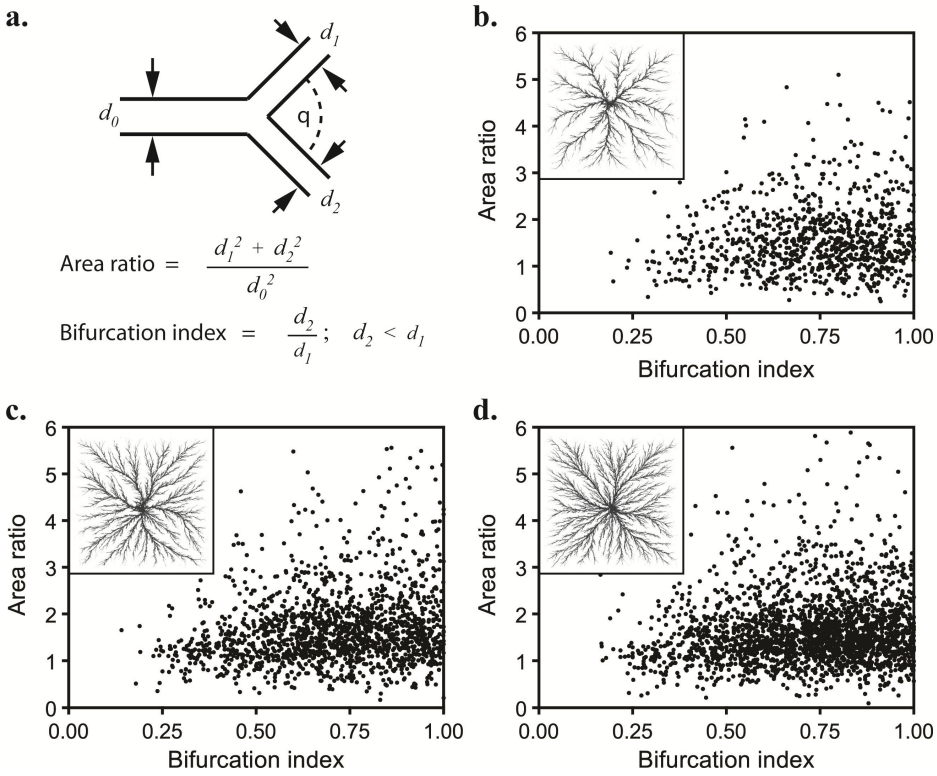

Figure 3.5.Microvascular networks produced under different irradiation/discharge conditions incorporate morphologically similar branching characteristics. (a) Quantitative branching parameters corresponding to bifurcation from a parent channel of diameter d_0 into two daughter channels of diameters d_1 and d_2.**(b-d)** Characterization of microchannel networks originating in the center of three identical 1x3x3 inch polished acrylic blocks subjected to **(b)** 1, **(c)** 2, and **(d)** 3 successive irradiation/discharge cycles. All three networks exhibit a similar relationship between the area ratio and bifurcation index. despite differences in the overall network density (inset). The area ratio data are mostly clustered about the limiting theoretical range between 1 and $2^{1/3}$ corresponding to Murray's law exponents of $k = 3$ and 2 respectively[151].

Table 3.1.Quantitative characteristics of branched microchannel networks.

Irradiation/ discharge cycles	Network density (%)	Average bifurcation angle θ (°)	Fractal dimension	Murray's law exponent, k
1	17.3	52.8	1.79	2.14
2	24.8	44.0	1.88	2.16
3	29.0	45.6	1.88	2.32

Parameters were determined from analysis of images reconstructed from microvascular networks embedded in acrylic blocks upon exposure to multiple irradiation/discharge cycles (Fig. 3.5b-d). Network density represents the fraction of the total image area occupied by the microchannel network (i.e., number of pixels associated with the network divided by total pixels in the image).

3.6 Summary

We introduce a nearly instantaneous method to embed branched 3D microvascular networks inside plastic materials. In this microfabrication process, a high level of electric charge is first implanted inside a polymer dielectric using electron beam irradiation. The accumulated energy is then discharged in a controlled manner to locally vaporize and fracture the material, leaving behind a network of branched microchannels arranged in a tree-like architecture with diameters ranging from approximately 10 μm to 1 mm. Modulating the irradiation profile and discharge locations allows the networks' morphology and interconnectivity to be precisely tailored. Interconnected networks with multiple fluidic access points can be straightforwardly constructed, and quantification of their branching characteristics reveals remarkable similarity to naturally occurring vasculature. This method can be applied in a variety of polymers, and may help enable production of organ-sized tissue scaffolds containing embedded vasculature.

CHAPTER IV

FABRICATION ENDOTHELIALIZED OF CIRCULAR MICROCHANNEL NETWORKS

4.1 Introduction

Physiological systems rely on branched flow networks to achieve efficient transport within extended 3D spaces[170], making the ability to replicate these features *in vitro* critically important in many fields[1, 2, 35, 171-173]. Planar micromachining is the most mature technology to construct synthetic microvascular networks, but it is not an ideal solution because cross-sectional profiles of the corresponding microchannels are typically square, rectangular, or trapezoidal. These topographies make it challenging to establish fully endothelialized microenvironments due to nonuniform cell seeding in the sharp corner regions[92]. Wall shear stresses can also vary widely at these locations[93, 94], potentially impacting flow-based studies[95-99]. Rounded cross-sectional profiles are therefore highly desirable, and recent progress toward this goal has made it possible to construct semi-circular topologies by applying methods such as photoresist-based molding[39], wet etching[42], electroplated molding[52], laser ablation[56], and micromilling[101]. Circular cross-sections are then produced by aligning and bonding two substrates imprinted with complementary semi-circular patterns. Sacrificial approaches also permit circular profiles to be obtained upon embedding and removal of soldering wire[174], sugar fibers[78], and polylactide fibers[175]. Post-fabrication circularization has also been demonstrated by coating rectangular microchannels with solvent diluted poly(dimethyl

siloxane) (PDMS)[176-178] and poly(methyl methacrylate) (PMMA)[179]. Alternatively, direct-ink writing has been employed to construct networks with circular cross-sectional shapes in hydrogel matrices albeit in a low throughput serial format[65]. In addition to limitations in fabrication technology, material specific issues also pose challenges to long term culture and biological response studies, particularly in the case of PDMS which is susceptible to nonspecific surface absorption and leaching of uncured monomer[180, 181].

4.2 Pressurized Air Deformation Process

We have developed a new strategy to overcome many barriers that have limited previous efforts to construct synthetic microvascular networks. Our approach is based on pressure-assisted expansion of biocompatible poly(lactic acid) (PLA) substrates—a versatile process that can be readily applied in both 2D and 3D branched networks incorporating a heirarchy of microchannel diameters. This treatment simultaneously renders the interior surfaces circular and smooth, yielding a robust cell-favored microenvironment capable of supporting uniform seeding and culture of endothelial monolayers under continuous flow. Rigid microchannels are first constructed in PLA by molding from a negative PDMS template (**Fig. 4.1a**). The resulting microchannels with rectangular cross-section are subsequently enlarged and shaped into circular profiles by heating the substrate and injecting compressed air under constant pressure (**Fig. 4.1b-d**). When pressurized air is injected in the glassy state, the interior air pressure force (F_{air}) is counteracted by resistance from the surrounding rigid wall (F_w) (**Fig. 4.1b and e**).

Increasing the temperature above the glass transition (T_g ~ 55 – 58 °C) causes the material to enter a rubbery regime where the interior air pressure force overcomes the wall resistance (**Fig. 4.1c and f**). Incubation at 80 °C for 8 min is sufficient to allow the interior of a 4 mm thick substrate to reach equilibrium (confirmed by placing a thermocouple probe between PLA layers; thermal conductivity = 0.13 W/m·K, specific heat capacity = 2,135 J/kg·K). Under these conditions, the microchannel initially assumes an elliptical profile, ultimately attaining an enlarged circular cross section after ~ 20 min (**Fig. 4.1d and 4.1g**). The process is arrested by quenching the sample at room temperature.

4.3 Mechanism of Polymer Deformation

The final microchannel diameter is governed by temperature, applied pressure, and incubation time. This interplay can be captured by a dynamic equilibrium associated with the internal stress balance $\tau = \frac{PR(t)}{h(t)}$ where τ is the hoop stress, P is the air pressure, $R(t)$ is the channel radius, and $h(t)$ is the wall thickness. When the wall thickness is much greater than the channel radius ($h_0 >> R_0$; h_0 and R_0 are initial values), the time variation of the wall thickness during enlargement can be approximated as $h(t) = h_0 - (R(t) - R_0)$. The deformation can be expressed in terms of the rate of strain $\dot{\varepsilon} = \frac{1}{R(t)}\frac{dR(t)}{dt}$, yielding the following upon substitution into stress balance $\frac{dR(t)}{dt} = \frac{P}{\mu}\frac{R^2}{(h_0 + R_0) - R}$, where μ is the material's viscosity coefficient.

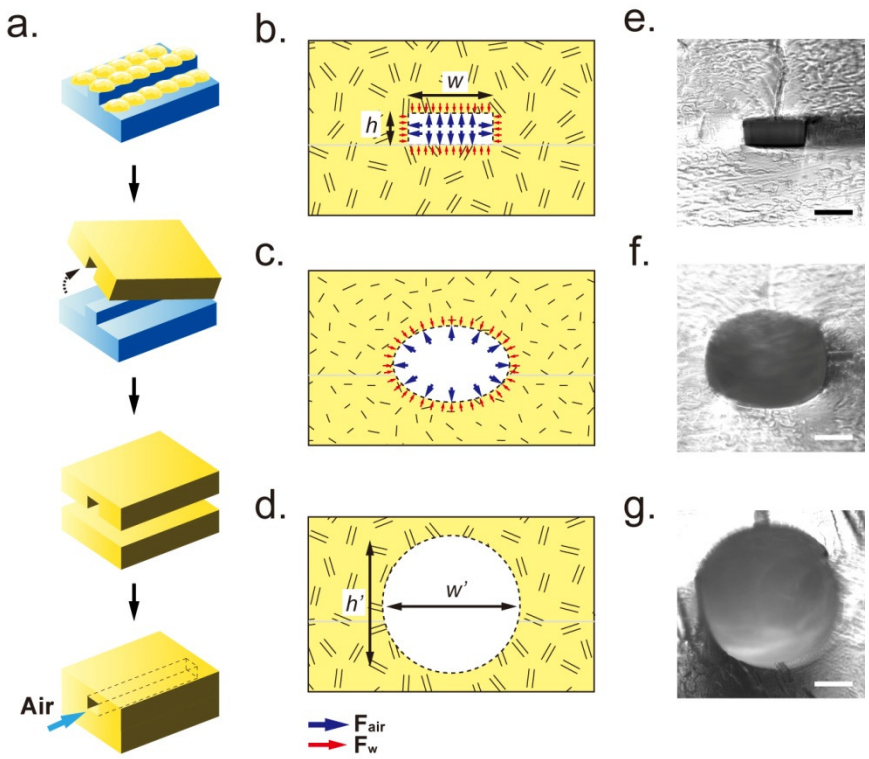

Figure 4.1.Enlargement of PLA microchannel diameters by pressure-assisted expansion. (a) Microchannel with initially rectangular cross-section in PLA. **(b-c)** Pressurized air is injected upon heating the PLA to the rubbery state (above glass transition temperature and below melting temperature) causing the interior air pressure force to exceed the wall resistance.The channel eventually assumes a circular shape. **(d-g)** Cross-sectional images of PLA microchannels**(d)** untreated; **(e)** 80 °C, 15 psi for 10 min; **(f)** 80 °C, 15 psi for 15 min; and **(g)** 80 °C, 15 psi for 25 min (expansion ratio = 5; bars, 50 µm).

This time dependent equation then can be solved to describe the relationship between inflation time and channel enlargement. Although this relatively simple model is strictly valid for thin walled tubes, good agreement is observed between these predictions and our experimental data displaying an exponential increase in channel size with time (**Fig. 4.2a)**. Circular cross sections can be obtained from initially rectangular microchannels within 20 min over a wide range of aspect ratios (initial height/width = 0.07 – 2.23) (**Fig. 4.2b**), with expansion ratios ranging from 5 – 10 (**Fig. 4.2c**). Elliptical cross sections are produced at shorter inflation times, while bursting eventually occurs in the long time limit.

4.4 Multi-Layers and Branched Microvascular Networks

We applied the air inflation technique in simplified 3D constructs using a seven layer thick synthetic microvascular network in PLA (**Fig. 4.3a**). The initially rectangular cross section of all four generations in the branched architecture became circularized in a single inflation step, with all microchannels attaining an aspect ratio close to unity. Our method therefore is not only capable of circularizing the cross sectional profiles, it also enables the process to be simultaneously performed across a broad range of microchannel diameters (~ 1.5 mm to 50 μm).

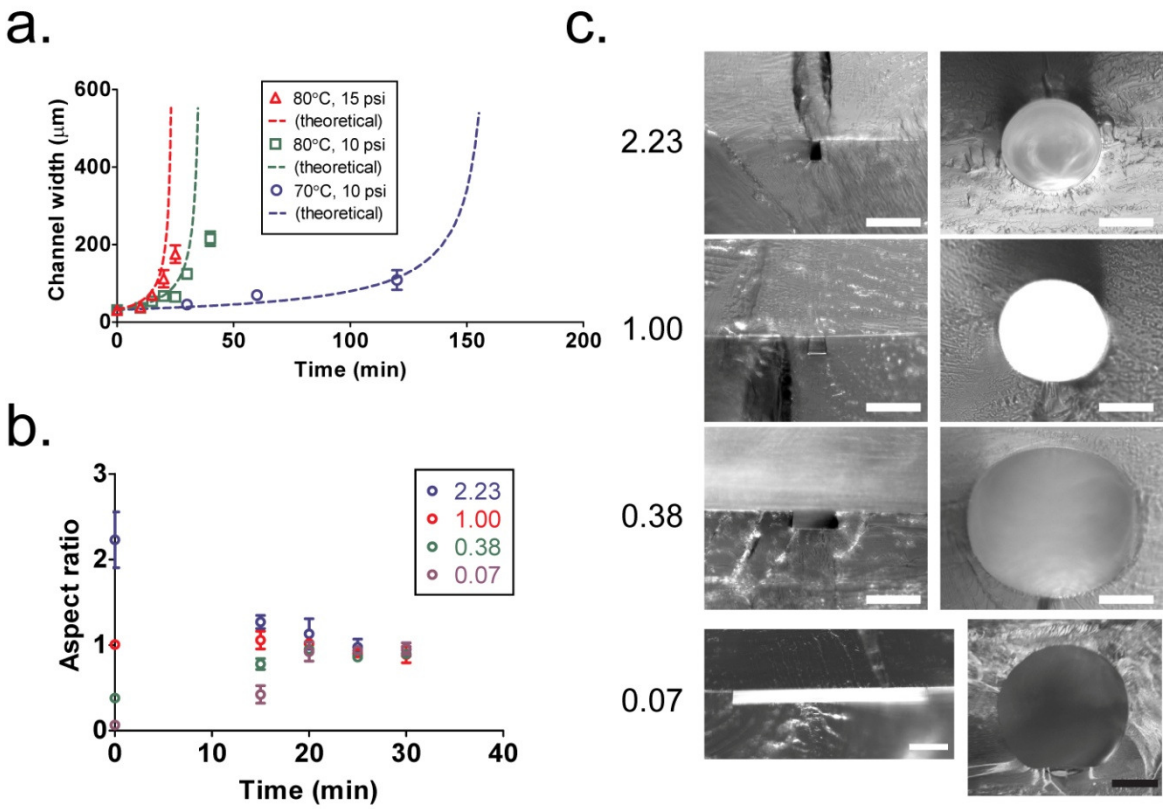

Figure 4.2.Characterization and optimization of inflation process. (a) Experimental results (dots) and analytic model (dash lines) show expansion of rectangular microchannels as a function of time and channel width (*w'*). Three different processing conditions were considered: 80 °C at 15 psi (red), 80 °C at 10 psi (green), and 70 °C at 10 psi (blue). **(b)** Effect of initial rectangular channel aspect ratio (80 °C at 15 psi). **(c)** Cross sectional images of channels with different aspect ratio before and after inflation under the same conditions as (b) (white bar, 100 μm; black bar, 1000 μm). Experiment data: mean ± SD (n = 3).

This is a significant finding because although similar network structures incorporating rectangular cross sections can be constructed using conventional lithography and molding approaches[48, 171, 173, 182], the microchannels in every branching generation inherently retain the same channel height. This creates a problematic situation because internal shear rates are therefore highly nonuniform (e.g., low aspect ratio channels display much higher shear rates in the vertical direction than in the horizontal plane), generating severe internal shear stresses that are physiologically unfavorable. We also applied the inflation method in a fully 3D synthetic microvascular network embedded in PLA using electrostatic discharge[81]. The interior microchannels were subsequently deformed, yielding a global increase in channel diameter throughout the network as well as smoother sidewall profiles (**Fig. 4.3b**). Unlike liquid etchants, pressurized air penetrates the entire network, yielding identical topographies in each branch.

4.5 Endothelialized Circular Microchannel Network

To study cell morphology under dynamic flow conditions during long term culture, and to demonstrate feasibility of employing PLA substrates for cell-based studies, bovine aortic endothelial cells (BAECs) were harvested from a static petri dish environment and seeded within a branched circularized synthetic microvascular network. We continually perfused culture medium at constant flow rate in a closed recirculation loop so that cell signaling interactions could be maintained.

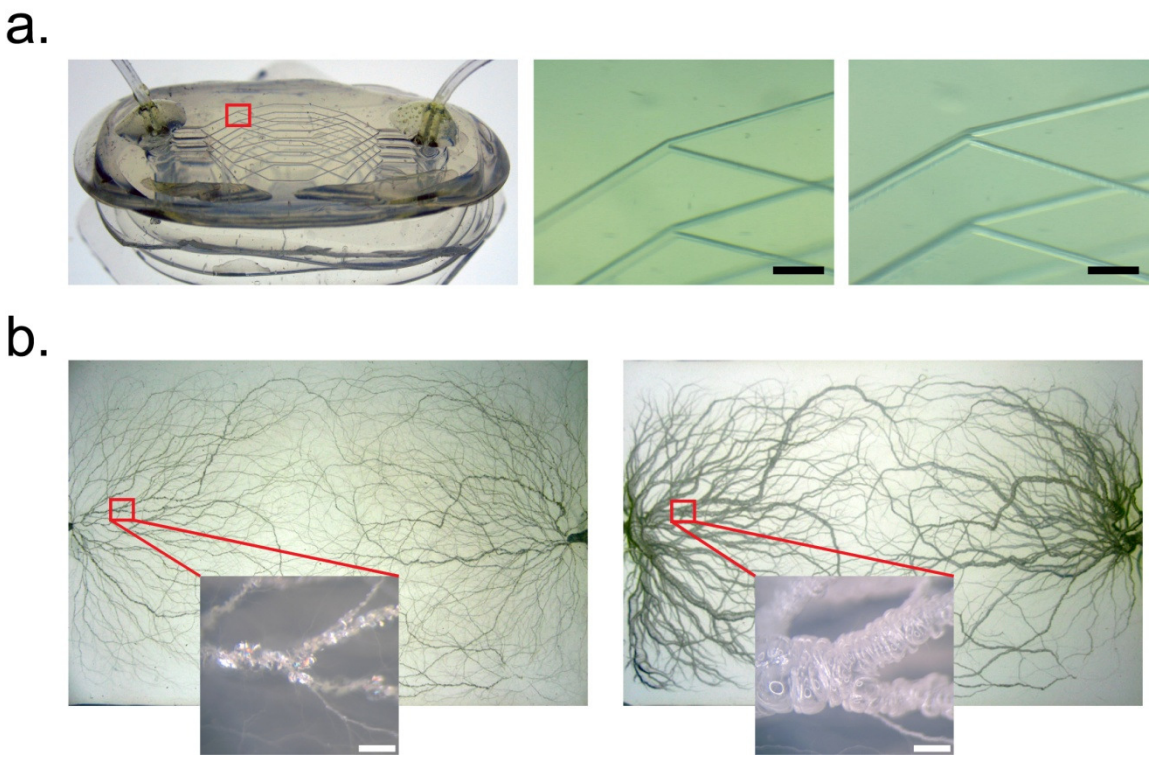

Figure 4.3.The application of air deformation process.(a) Seven layers stacked PLA branched networks before and after treatment. Bar, 300 µm. **(b)** 3D branched microchannel network embedded in 1.5 cm x 5 cm x 8 cm molded PLA block by electrostatic discharge. Before treatment, the microchannel diameters are not optimal for cell seeding. After air inflation, the average channel diameters are significantly widened throughout and the sidewall topology becomes smoother. Bar, 500 µm. All channels mentioned above were injected with 15 psi of pressurized air for 20 min at 80 °C.

Live cell confocal microscopy revealed uniform attachment and growth of a confluent BAEC monolayer along the microchannel walls (**Fig. 4.4a**).Endothelial cells could be successfully seeded within four generations of a branched microchannel network whose smallest channel size was below 50 μm (**Fig. 4.4b**), with viability maintained for up to 2 days. However viability and morphology could be maintained for at least 5 days in straight microchannels under identical continuous flow conditions (**Fig.4.4c**, due to the long term incubation, CellTracker stained cells displayed weak florescence after day 5). These differences reflect unique challenges associated with culture in synthetic microvascular networks as compared with previous studies focused on straight microchannels. First, the hierarchy of channel sizes leads to differences in local cell density within each branch. Consequently, the same seeding conditions may place gaps between adjacent cells in larger channels while simultaneously imposing crowding and overlap in smaller peripheral branches. The less severe sidewall curvature in larger microchannels (> 100 μm diameter) is also more favorable to establish uniform coverage, whereas very different environments emerge in smaller capillaries whose dimensions approach those of the flattened cells (~ 50 – 100 μm in length, 10 – 20 μm in width). The ability to successfully seed BAECs throughout a branched network (**Fig. 4.4d**) is therefore a significant finding because it represents a more physiologically realistic scenario than has been previously considered. More work is needed, however, to identify flow conditions that optimally achieve uniform long-term culture throughout the entire network.

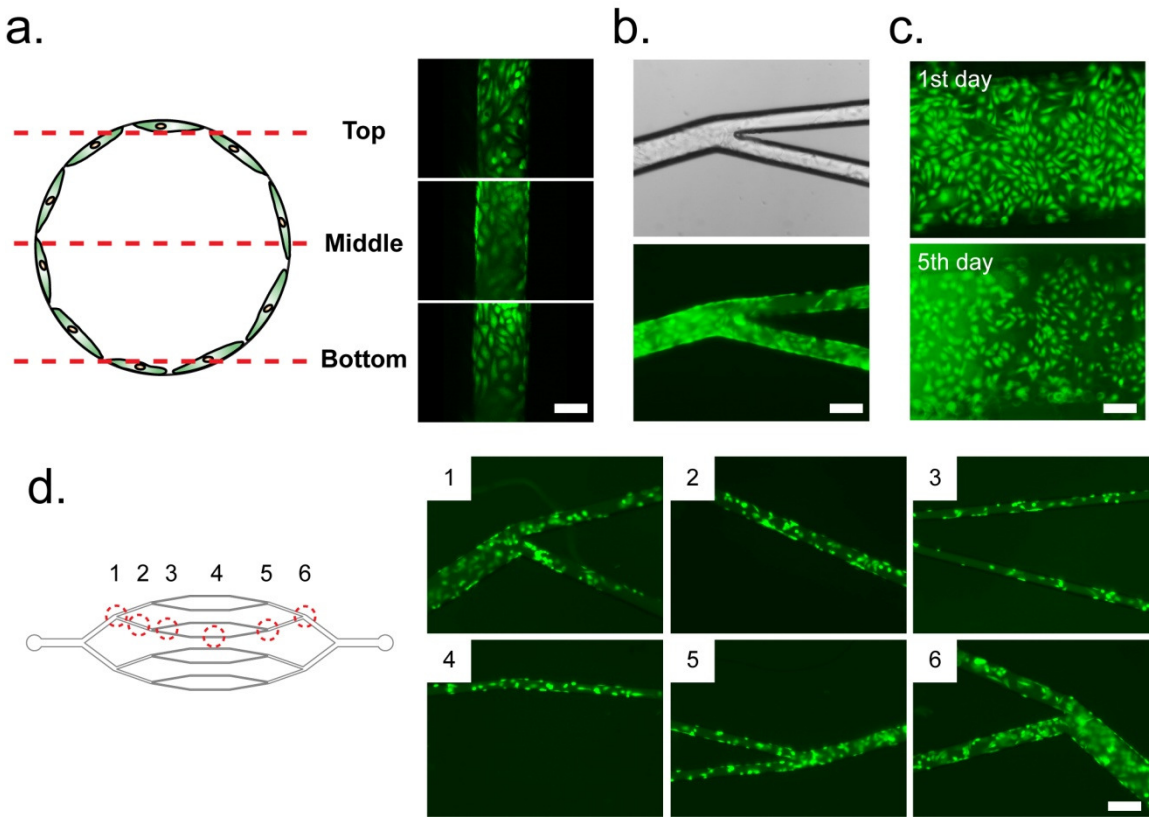

Figure 4.4. Imaging of bovine aortic endothelial cells (BAECs) cultured in circular microchannels.(a) Illustration of image acquisition in top, middle and bottom focal planes. Confocal images show 100 µm of microchannel walls were seeded with endothelial cells and confirmed that cells can be confluently cultured in monolayer surrounded the channel wall after 3 days. CellTracker was used in this study to continuously observe live cells. **(b)** BAECs can also be cultured within circular branched network with diameter range lower than 50 µm. The cells are observed in bright view and **(c)** Fluorescent images show BAECs survived and maintained cell morphology after 5 days. **(d)**BAECs were seeded in four generations of branched network and covered all channel walls. Bar, 50 µm.

4.6 Summary

Synthetic microvascular networks are essential to enable *in vitro* studies of cell biology, biophysics, hemodynamics, and drug discovery, as well as in applications involving tissue engineering and artificial vasculature. But current limitations make it challenging to construct networks incorporating a hierarchy of microchannel diameters possessing cell-favoring circular cross-sectional topographies. We report a new approach that overcomes these limitations by employing pressure-assisted expansion of biocompatible poly(lactic acid) (PLA) substrates. These controllable processes can precisely contribute interconnected microchannel networks with wide range of diameter for each level of branching and circular cross-sections geometry within 3D or pseudo-3D substrate. Additionally, *in vitro* cell culturing demonstrated confluent cell monolayer endothelialized in microvasculature chip and indicated that this platform can potentially provide a bio-mimicking environment for advanced biological and clinical studies.

CHAPTER V

ENZYMATIC SCULPTING OF NANOSCALE AND MICROSCALE SURFACE TOPOGRAPHIES*

5.1 Introduction

Living systems display complex structured nano- and micro-scale topologies that orchestrate a host of physical and biological functions[183-187]. But these features can be challenging to replicate using conventional planar methods[188], and nanometer-scale structures cannot be readily constructed without dedicated facilities[189-193]. Herein we show how enzymatic activity can be harnessed to fashion complex nano- and microscale surface topographies on biodegradable substrates. Coordinated patterning and machining are accomplished by manipulating interactions between an enzyme, substrate, and protein inhibitor. In this way, we are able to construct nanochannels, microchannels containing embedded features templated by the substrates crystalline morphology, and a membraneless filter capable of isolating rare cells from whole blood with a throughput that is orders of magnitude greater than currently possible.

---

* Part of the data reported in this chapter is reprinted with permission from: Enzymatic sculpting of nanoscale and microscale surface topographies by Huang, J.H., Jayaraman, A. and Ugaz, V.M. *Angew Chem Int Ed Engl***51**, 9619-9623 (2012).

In addition to enabling molecularly imprinted surface landscapes mimicking those in living systems to be fashioned by a straightforward process accessible in virtually any laboratory, considerable potential exists to exquisitely control the underlying biochemicalinteractions by employing enzymes and substrates with appropriately engineered properties.

5.2 EnzymaticBiosculpting

Our bioinspired machining approach exploits the enzymatic activity ofproteinase K (PK), a serine protease capable of cleaving peptide bonds with particular affinity toward alanine-alanine linkages[194]. Poly(lactic acid) (PLA) serves as a convenient substrate because it is also susceptible to this degradation mechanism owing to structural similarities between lactic acid and alanine. Machining is initiated when PK is transported from the bulk environment to the PLA surface, after which enzyme-substrate complexation catalyzes surface reactions yielding low molecular weight cleavage products that subsequently become hydrolyzed and are released into the bulk along with dissociated PK (**Fig. 5.1a**). Patterned machining is accomplished by directing an aqueous PK solution through a microfluidic template (constructed from poly(dimethyl siloxane) (PDMS) using conventional soft lithography (see also Chapter II) so that the ensuing enzymatic degradation imprints a replica of the flow path into a PLA substrate on the microchannel floor (**Fig. 5.1b**). Characteristic degradation rates of 2 μm/h are achievable in a 300 μm-wide, 10.7 mm-long microchannel (**Fig. 5.1c**). Feature depths increase monotonically with enzyme concentration up to about 4 μM, above which

surface complexation sites become saturated (**Fig. 5.1d**)[195, 196]. Machining also reflects temperature-dependent enzymatic activity, which occurs about 7 times faster at 37 °C than at room temperature (**Fig. 5.1e**). These rates enable nanometer-size features to be easily imprinted, as illustrated by construction of a 170 nm deep channel via injection of a PK solution at 2 μL/min for 3 h at room temperature (**Fig. 5.1f**).

5.3 Competitive Interaction between Enzyme and Inhibitor

Complex cross-sectional topologies can be fashioned by establishing gradients in enzyme concentration that spatially regulate the machining process. The macromolecular architecture of PK confines lateral diffusion (D = 8.1 x 10^{-7} cm^2/s at 25 °C[152]), enabling the dimensions of imprinted features to be maintained over a much greater downstream distance than possible using conventional small-molecule chemical etchants (e.g., D = 1.6 x 10^{-5} cm^2/s for hydrofluoric acid (HF) etching of glass at 25 °C[197]). Feature definition is further enhanced by replacing the buffer stream with a 1% w/v aqueous solution of bovine serum albumin (BSA) to establish a competitive interaction that inactivates the laterally diffusing enzyme before it can attack the PLA (**Fig. 5.2a**). The resulting complexation between PK and BSA enables sharper boundaries to be established between the machined and masked regions.

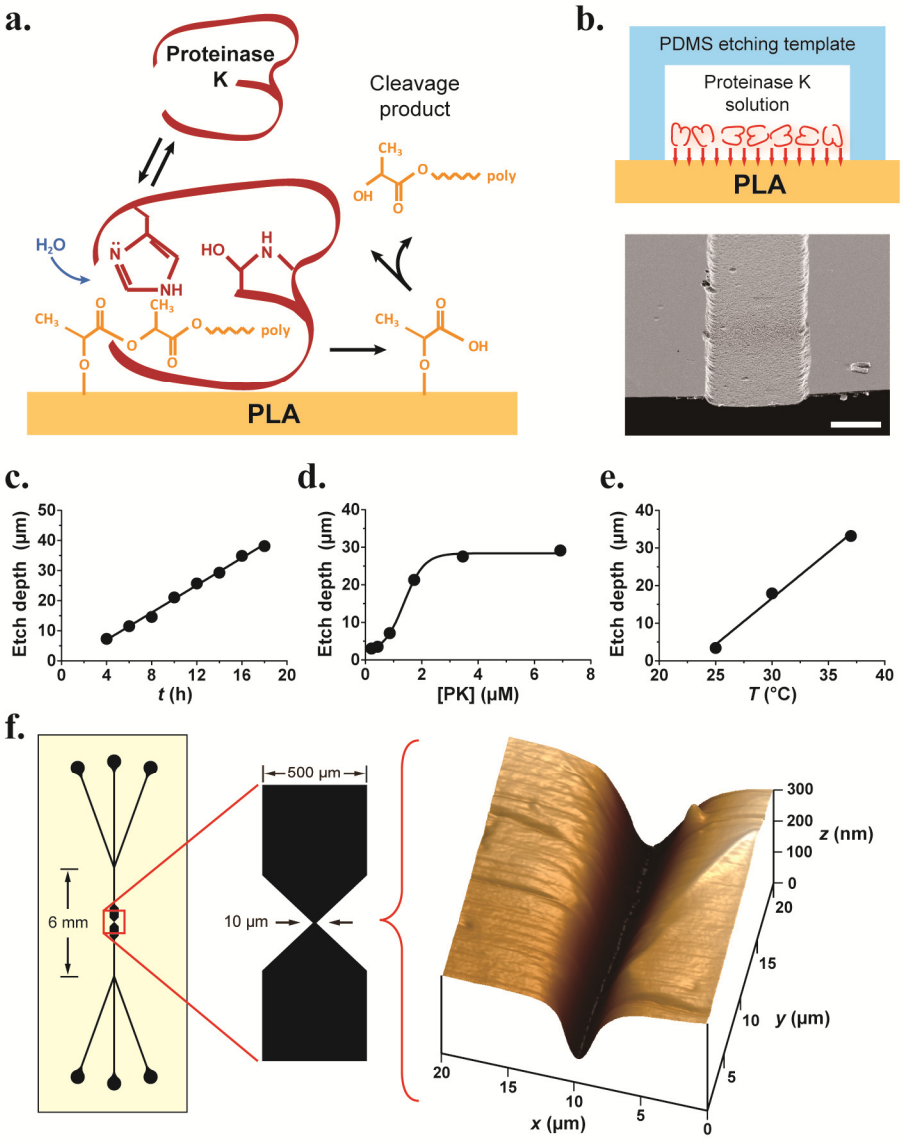

Figure 5.1.Enzymatic nano- and micro-machining. **(a)** Biochemical degradation cycle between proteinase K (PK) and the PLA substrate. **(b)** Cross-sectional schematic (above) illustrating how machining is performed by directing an aqueous PK solution through a PDMS microchannel template bonded to a PLA sheet (bar in SEM image below, 200 μm). **(c)** Feature depth versus time ([PK] = 6.92 μM (0.2 mg/mL), 5 μL/min, 37°C). **(d)** Depth versus enzyme concentration (5 μL/min, 37°C, 16 h). **(e)** Depth versus temperature ([PK] = 6.92 μM, 5 μL/min, 16 h). **(f)** A nanochannel (170 nm deep) is constructed by injecting PK into a PDMS template (left) for 3 h at 25 °C. Machining is laterally confined within a ~ 4 μm-wide zone by hydrodynamic focusing of PK between co-injected streams of bovine serum albumin (2 μL/min each stream; see Fig. 6.2 and Methods). The *z*-axis of the AFM surface profile (right) is expanded to show detail.

Patterning is controlled by adjusting the relative concentrations and flow rates of enzyme and BSA in order to manipulate the balance between convection and diffusion (expressed in terms of a Péclet number $Pe = uL/D$; where u, l, and D represent the characteristic flow velocity, diffusion length, and diffusion coefficient, respectively). In conventional laminar flow patterning, convection-dominated confinement of chemical etchants is only possible at high flow rates ($Pe \sim 5 \times 10^3$ for HF etching of glass at u = 0.1 m/s)[198-200]. In contrast, enzymatic machining employs macromolecular species that display greatly reduced diffusivities, enabling high Pe to be maintained at low flow rates ($Pe \sim 4 \times 10^3$, u = 0.005 m/s) to minimize reagent consumption and operate below the threshold for undesirable inertial effects (i.e., Dean vortices that would disrupt pattern fidelity along curved flow paths). We applied a convection-diffusion model to capture this interplay, yielding close quantitative agreement between the cross-sectional profile of the machined microchannels and the predicted distribution of free (uncomplexed) PK (**Fig. 5.2b** and **Fig. 5.3**).

5.4 Kinetic Model

Direct observation using fluorescently labeled BSA reveals the lateral concentration profile, with a 10 % w/v solution experiencing significant transport into the adjacent stream (**Fig. 5.3**). This effect acts to confine the etching zone by promoting strong complexation with PK.

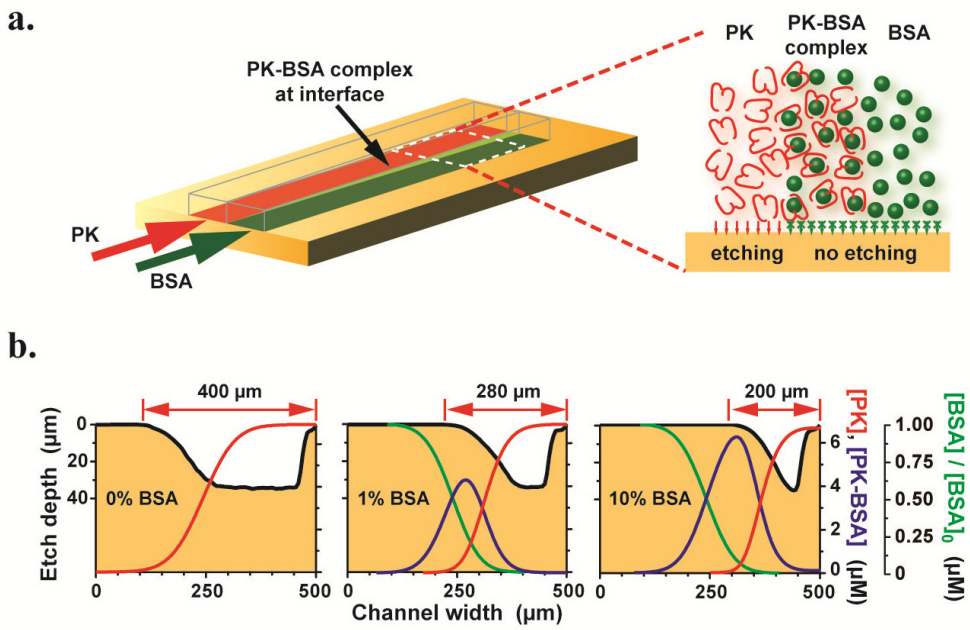

Figure 5.2. Machining is governed by a competitive interaction between enzyme, substrate, and inhibitor. **(a)** When PK (red) and BSA (green) are co-injected into a microchannel, a localized interfacial zone of PK-BSA complexation establishes the boundary of the machined region. **(b)**Profilometery measurements of machined profiles obtained 1 cm downstream from the inlet (black line; left ordinate) as a function of BSA concentration are overlaid with predicted lateral concentration profiles of free PK and PK-BSA complex (red and blue lines, respectively; inner right ordinate) and BSA normalized to the injected concentration (green line; outer right ordinate). Machining conditions: [PK] = 6.92 μM in the bulk solution, 5 μL/min, 37°C, 16 h, $[BSA]_0$ = 0.15 and 1.5 mM for 1 and 10 % solutions, respectively.

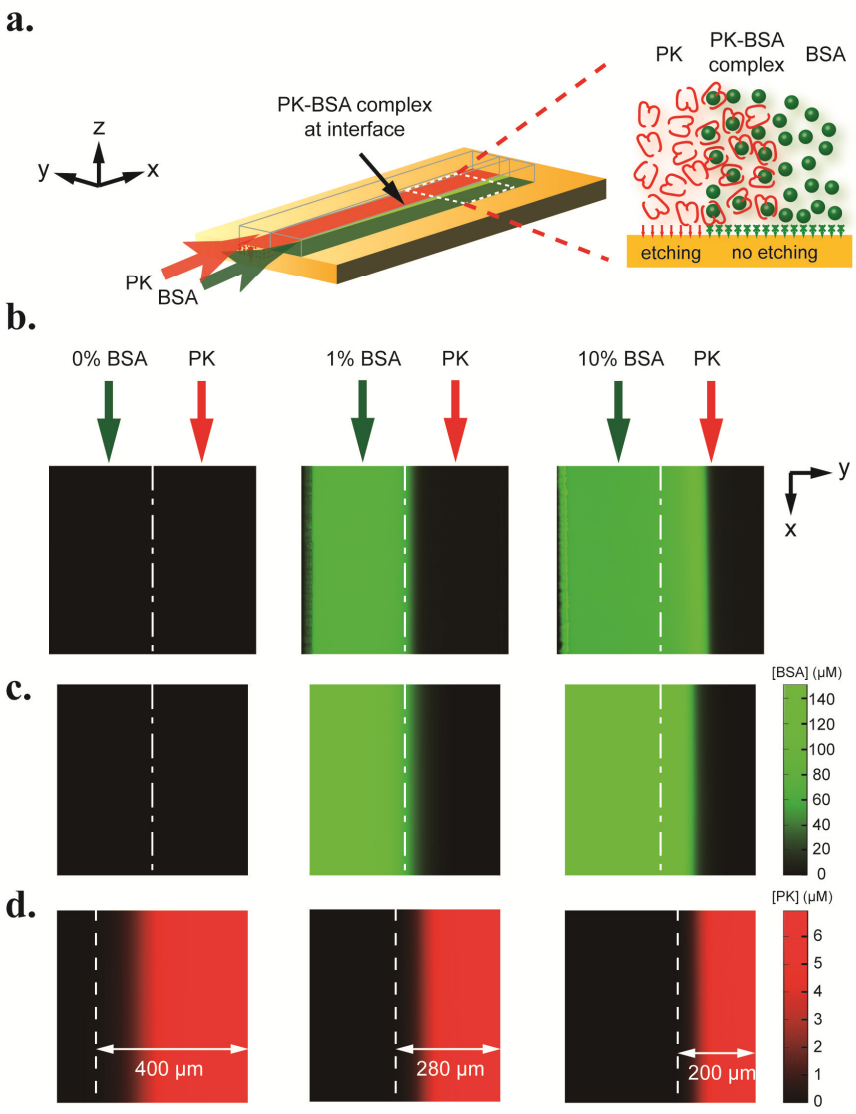

Figure 5.3.Concentration distribution of enzyme and inhibitor.(a) When PK (etchant, red) and BSA (inhibitor, green) are co-injected into a microchannel, a localized interfacial zone of PK-BSA complexation establishes the boundary of the etched region. **(b)** The lateral concentration profile of FITC-BSA is visualized using fluorescence microscopy at three different concentrations (images were acquired in a 500 x 500 μm window located 1 cm downstream from the inlet, dashed line indicates centerline). **(c)** Predicted BSA concentration profile obtained by numerical simulation of the 2D convection-diffusion model in Equations 5.1 – 5.3 (dashed line indicates centerline). **(d)** Predicted concentration profile of free (uncomplexed) PK defining the effective etching zone (dashed line indicates etched boundary where the enzyme concentration approaches zero; effective width of the etched zone is indicated).

The underlying mechanics governing this interplay can be captured in terms of a convection-diffusion framework, yielding a system of differential equations expressing the concentrations of PK, BSA and PK-BSA complexes (C_{PK}, C_{BSA}, and $C_{PK\text{-}BSA}$, respectively).

$$\frac{dC_{PK}}{dt} + \nabla \cdot \left(-D_{PK}\nabla C_{PK} + C_{PK}u\right) = k_{off}C_{PK-BSA} - k_{on}C_{PK}C_{BSA} \tag{5.1}$$

$$\frac{dC_{BSA}}{dt} + \nabla \cdot \left(-D_{BSA}\nabla C_{BSA} + C_{BSA}u\right) = k_{off}C_{PK-BSA} - k_{on}C_{PK}C_{BSA} \tag{5.2}$$

$$\frac{dC_{PK-BSA}}{dt} + \nabla \cdot \left(-D_{PK-BSA}\nabla C_{PK-BSA} + C_{PK-BSA}u\right) = k_{on}C_{PK}C_{BSA} - k_{off}C_{PK-BSA} \tag{5.3}$$

Here D_{PK}, D_{BSA}, and $D_{PK\text{-}BSA}$ are the diffusivities of each species in solution, and the bulk fluid flow is directed axially along the length of the microchannel (the *x*-direction) with characteristic velocity *u*. The association and disassociation rate constants (k_{on} and k_{off}, respectively) represent PK complexation with BSA (i.e., $PK + BSA \underset{k_{off}}{\overset{k_{on}}{\leftrightarrow}} PK - BSA$).

The transport model in Equations 5.1–5.3 was numerically evaluated using COMSOL Multiphysics (version 4.0a, COMSOL, Inc.). The two-dimensional convection-diffusion mode was selected from COMOSL's model library, and the computational domain was discretized into a mesh of quadrilateral elements. Properties of water at 37 °C (ρ = 993.36 kg/m^3, μ = 6.9 x 10^{-4}Pa·s) were used to represent all solutions (PK, buffer, BSA). Diffusion coefficients for PK, BSA, and PK-BSA complex were estimated to be 1.22 x 10^{-6}, 9.25 x 10^{-7}, and 8.2 x 10^{-7} cm^2/s, respectively based on their molecular weight (T = 37 °C)[152]. Association and disassociation rate constant values of k_{on} = 4 M^{-1} s^{-1} and k_{off} = 10^{-4} s^{-1} were assumed based on literature data[201]. The

flow velocity u was determined by analysis of the fully developed two-dimensional velocity profile obtained by solving the steady-state Navier-Stokes equations in the etching template geometry (50 x 500 µm cross-section, 5 µL/min flow rate). Since transport of PK to the PLA surface is governed by the near-wall flow field, a velocity of $u = 4.67 \times 10^{-4}$ m/s was chosen as a representative value that best fit the experimentally observed BSA concentration profile (corresponding to a distance of 1.1 µm from the PLA surface; **Fig. 5.4**).

5.5 Microchannels with Irregular Cross Section

More intricate topologies where the feature depth varies along the microchannel's cross-section can be fashioned by sequentially changing the composition and flow conditions (**Fig. 5.5a**). We demonstrated this by employing a microchannel template with three independent inlets to fashion a cross-sectional profile incorporating a weir-like centerline barrier oriented parallel to the flow direction. First, BSA solution was injected into the center steam while PK was introduced into both outer streams for 4.7 h at 37 °C (2.3 µm/h degradation rate), machining the PLA substrate to a depth of 10 µm on either side of the central zone.

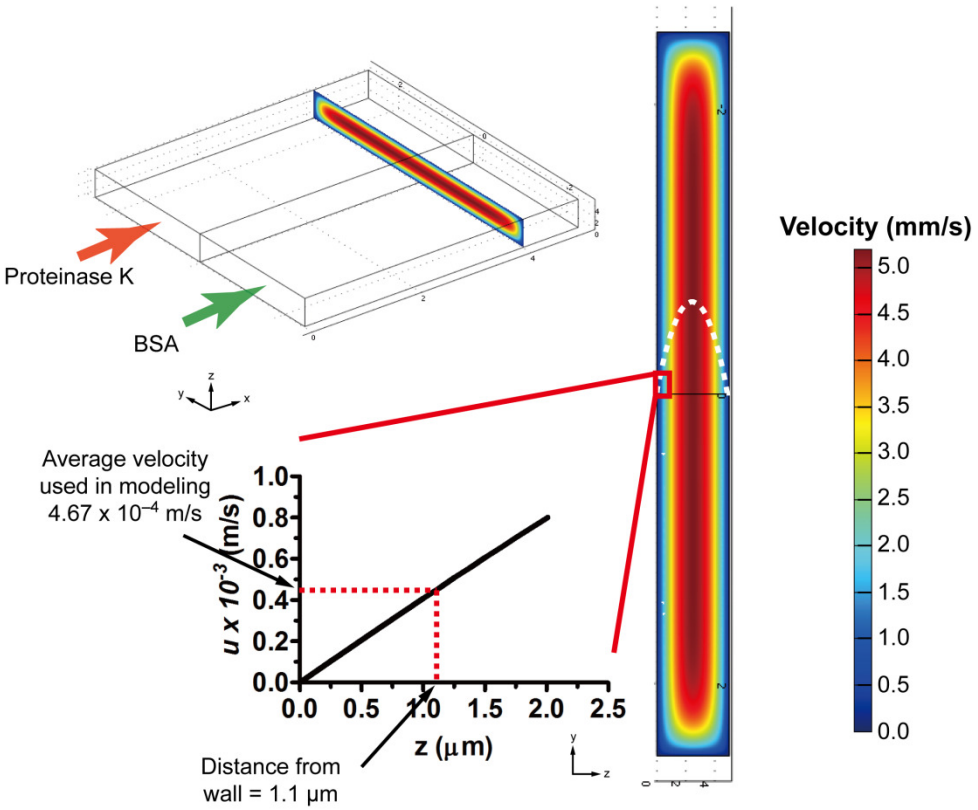

Figure 5.4.Simulated velocity profile.The velocity profile within a microfluidic etching template (50 x 500 µm cross-section, 5 µL/min flow rate) simulated by solving the steady-state Navier-Stokes equations. The velocity at a distance of 1.1 µm from the PLA surface (4.67 x 10^{-4} m/s) was selected for subsequent calculations to evaluate the transport model in Equations 5.1 – 5.3.

Next, BSA was infused into both the center stream and one of the outer streams for 8 h, yielding different depths on each side of the microchannel. Finally, PK was injected into all three inlets for 3 h to define the height of the central barrier. When completed, this process produced a cross-sectional profile incorporating three different

depths (13, 6, and 20 μm from left to right; **Fig. 5.5b**)—a topology preserved along the entire length of the microchannel (**Fig. 5.6a**). Feature sizes can be further tuned by varying the relative flow rates of BSA and PK to hydrodynamically focus the desired streams (**Fig. 5.6b**). Topologies incorporating continuously varying cross-section dimensions, challenging to build using conventional planar methods, can be readily constructed by imposing suitable enzyme concentration gradients (**Fig. 5.6c**). The machined structures can be used as-is, or alternatively the rigid PLA substrate can serve as a re-usable master mold for replication in PDMS by soft lithography (see also **Fig. 2.3**). Thus, even though micron-scale enzymatic machining may be relatively slow, the resulting structures are amenable for mass-production.

5.6 Microchannel with Crystallized Structures

The highly specific nature of enzyme-substrate interactions can also be exploited to enable direct imprinting of molecular-scale topologies. We explored this potential by taking advantage of the machining rate selectivity to PLA crystallinity (increasing the degree of crystallinity from 0 to 50 % yields a ten-fold decrease in the material degradation rate[202]) to embed morphological features associated with the substrate's crystalline domains within a fluidic channel (**Fig. 5.7a**). The crystalline morphology is in turn governed by thermal history (annealing time and temperature, cooling rate) and material properties (molecular weight, stereoisomers and their blends), permitting broad control over the imprinted topologies (**Fig. 5.8**). Machining after the PLA is continuously cooled from the melt exposes a dendritic surface topology (**Fig. 5.7b**),

whereas an array of obstacles reflecting the size and density of spherulitic crystalline domains emerges when PK is injected following a low-temperature anneal (70 °C for 8 h[203]) (**Fig. 5.7c**). In this way, the extent and distribution of crystallinity within the substrate can be manipulated to enable post-like arrays with tunable size and density to be embedded within a fluidic channel in a lithography-free manner.

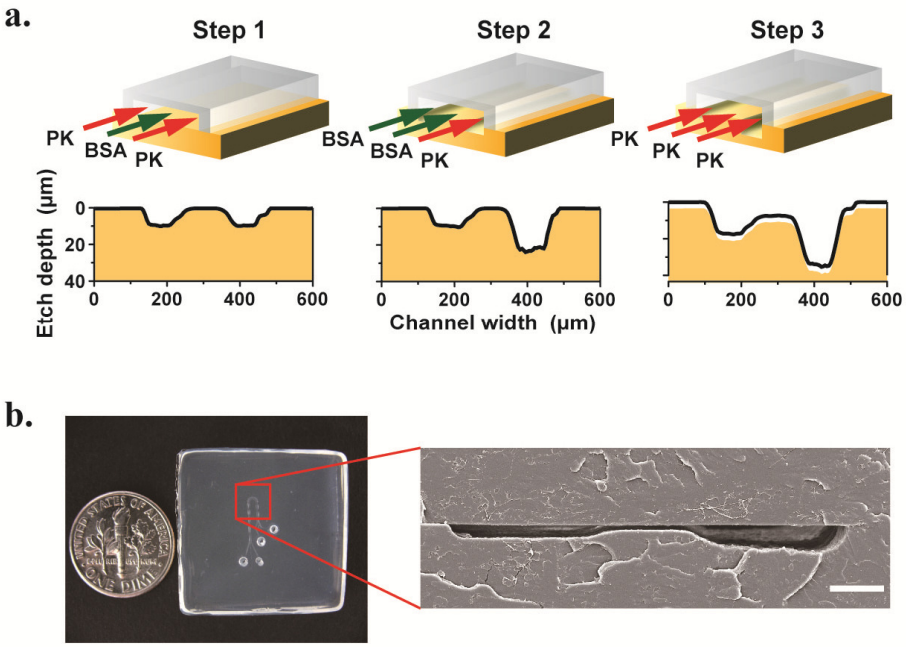

Figure 5.5 Strategy of enzymatic etching.**(a)** Alternating flows of PK and BSA are introduced to fashion a microchannel whose depth varies along the cross-section. Surface profiles are obtained 0.5 cm from the inlet ([PK] = 6.92 μM, [BSA] = 1% w/v (150.6 μM), all flow rates = 5 μL/min). **(b)** SEM image of microchannel incorporating an inner flow channel, central barrier, and outer flow channel with depths of 13, 6, and 20 μm, respectively (from left to right). After machining, the PLA microchannel is thermally bonded to a flat PLA sheet to form an enclosed flow network (bar, 50 μm).

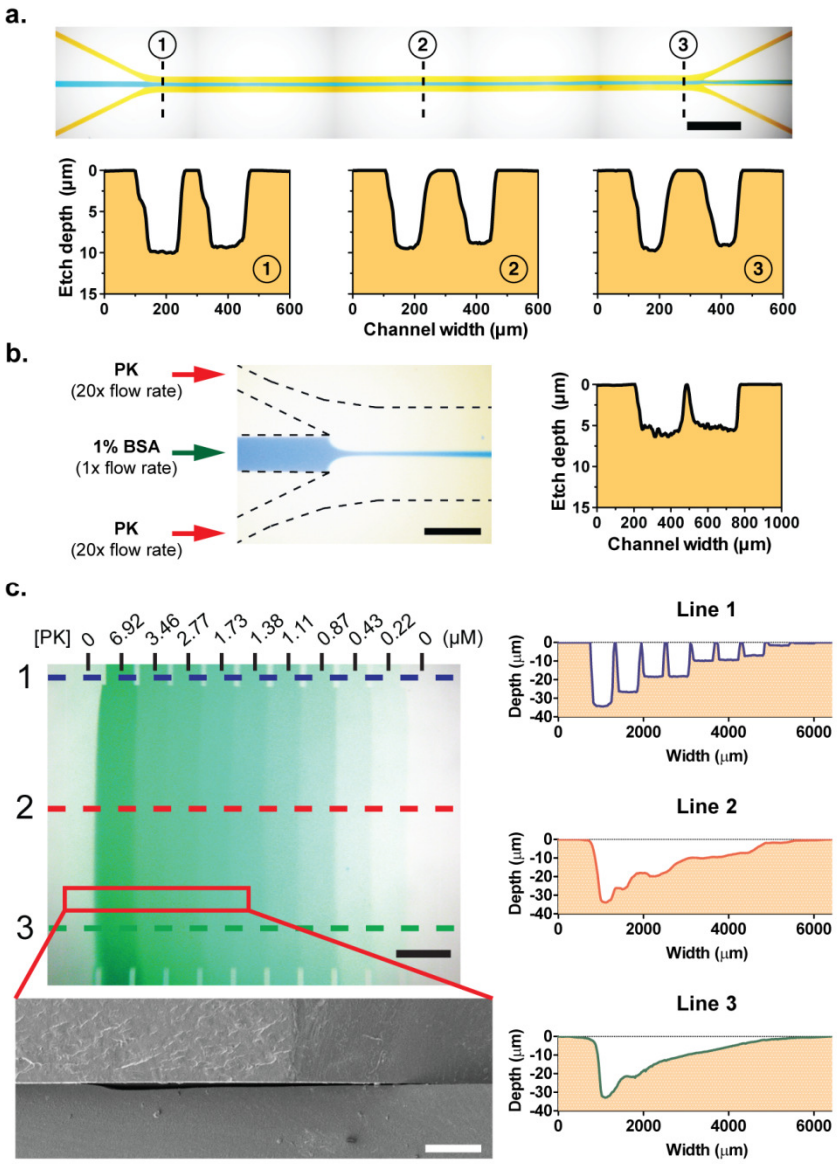

Figure 5.6.Diverse etched structures.**(a)**Profilometry measurements as a function of downstream position confirm that the etching profile is maintained along the entire microchannel length (etching conditions same as in Fig. 5.5a; bar, 1 mm) **(b)** Different flow rates can be applied in each stream to further control the size of the etched zone by hydrodynamic focusing (etching conditions same as in (a) except that flow rates of 10 and 0.5 μL/min were applied in the PK and BSA streams, respectively; bar, 300 μm). **(c)** PK and buffer are co-injected into a microfluidic gradient generating template and allowed to etch PLA at 37 °C for 16 h (22 μL/min, *Re* = 0.16, *Pe* = 0.09; bar in photo, 1 mm). The etched profile shows a continuously varying depth corresponding to the lateral concentration profile of PK (bar in SEM image, 300 μm).

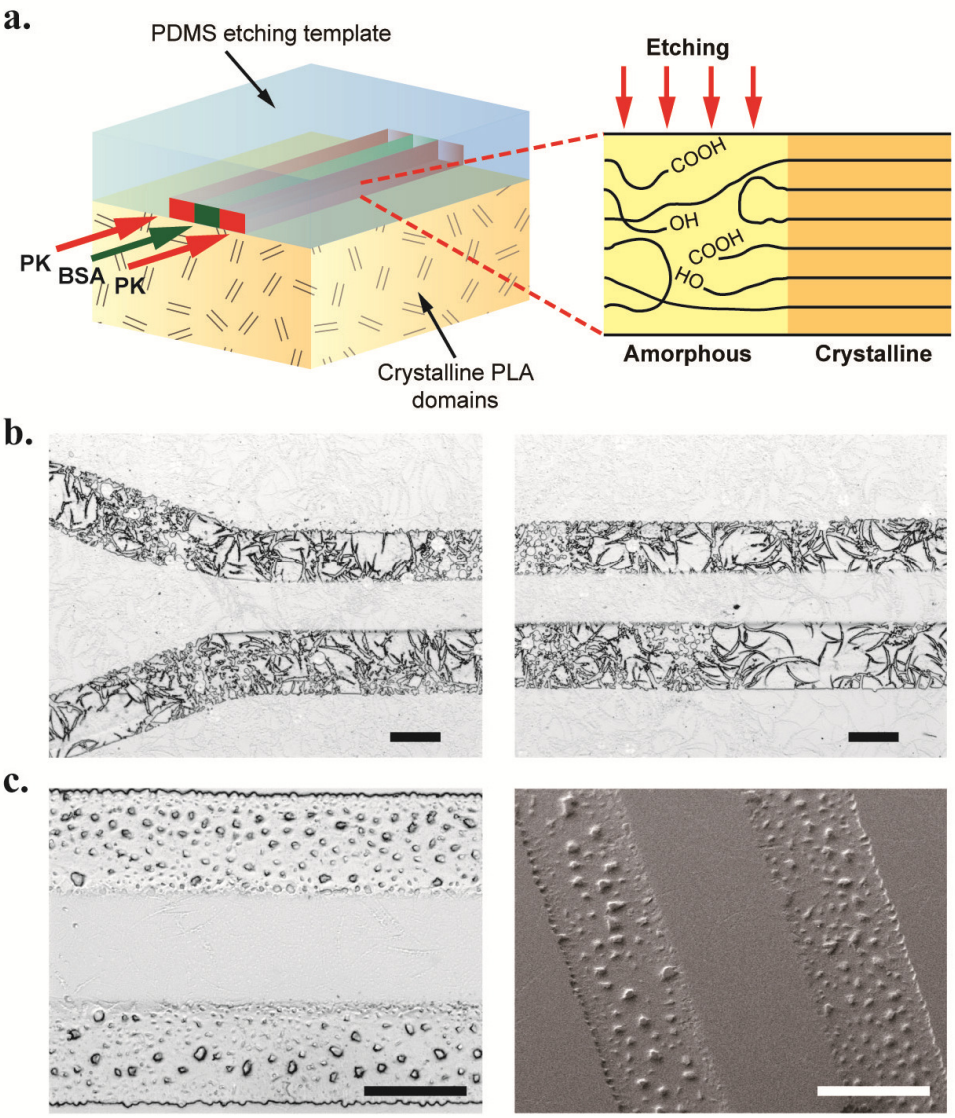

Figure 5.7.Machining molecularly templated surface topographies. **(a)** Morphologically governed selectivity is made possible by differences in the rate of PK-mediated degradation between hydrolysis-resistant crystalline domains and amorphous regions containing condensed hydrophilic and catalytic terminal groups (–OH and –COOH). **(b)** Machining after continuous slow cooling from 180 °C exposes dendritic features. **(c)** Machining after annealing at 70 °C for 8 h embeds an array of post-like obstacles within the microchannel (a 3D topology is evident in the SEM image, right). PK was injected at 37 °C for 2 h using the microchannel template in Fig. 3a (bars, 100 µm).

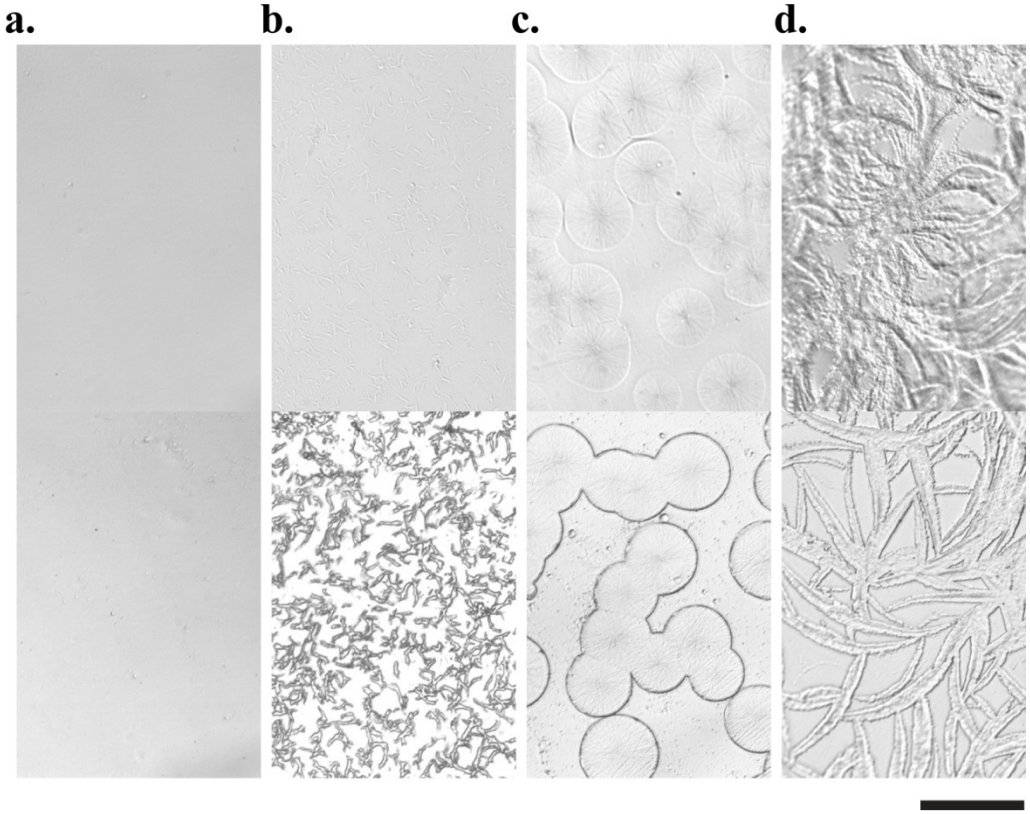

Figure 5.8.Polymer crystal morphology.Morphological dependence on thermal history in crystallized PLA before (upper images) and after (lower images) enzymatic etching with 0.2 mg/mL PK for 2 h at 37 °C. The PLA samples were cooled from the melt (180 °C) to room temperature (25 °C) as follows: **(a)** removed from 180 °C oven to room temperature; **(b)** annealed in oven at 80 °C for 1 h, then removed to room temperature, **(c)** annealed at 120 °C for 1 h, then removed to room temperature; and **(d)** cooled slowly (~ 10 h) to 25 °C in oven. Bar, 50 µm.

5.7 Summary

We report how enzymatic activity can be harnessed as a tool to fashion complex nano- and micro-scale surface topographies on biodegradable substrates. Coordinated patterning and machining are accomplished by manipulating interactions between an enzyme, substrate, and protein inhibitor. In this way, we are able to construct nanochannels, microchannels containing embedded features templated by the substrate's crystalline morphology, and an irregular cross section of microchannel capable of performing mixing, separation and other biological applications greater than currently possible. In addition to enabling molecularly imprinted surface landscapes mimicking those in living systems to be fashioned via a straightforward process accessible in virtually any laboratory, considerable potential exists to exquisitely control the underlying biochemical interactions by employing enzymes and substrates with appropriately engineered properties.

CHAPTER VI

MEMBRANELESS HIGH-THROUGHPUT CELL SEPARATION

6.1 Introduction

There is a critical need for advanced filtration methods adaptable for separation of cells and cell-sized components from blood, specifically offering the capability to rapidly process large volumes (>mL/min flow rates)[111, 204]. Microfluidic technologies provide a natural platform to address these challenges, but these methods generally require timescales of hours (sometimes tens of hours) to process standard 5 mL samples, making them impractical for routine use. Another key area where high-throughput blood separation is important is analysis of rare cell biomarkers relevant to cancer (e.g., circulating tumor cells (CTCs)). Microfluidic methods based on micromachined filtration structures that act either alone (to provide size-selective isolation)[125, 127], or in tandem with functionalized antibodies (to provide affinity capture) show considerable promise[119, 205], but also suffer from limitations inherent to the filtration-based design. Most notably, achievable flow rates are typically very small due to the large pressures that must be applied to inject a cell laden suspension through the tiny internal pore-like networks. Consequently, highly diluted cell suspensions must often be used (making it necessary to process even greater volumes due to the rare nature of CTCs), and large internal shear stresses make recovery of viable cells challenging unless extremely low flow rates are applied (further increasing the analysis time).

We have developed a new filtration approach that overcomes these limitations. Our previous design was based on a microfluidic architecture incorporating an embedded weir-like barrier oriented parallel to the flow direction and extending along the entire centerline length of a microchannel[206](see Chapter V). This arrangement, combined with the transverse centrifugal flow generated within the microchannel's curved path, creates a driving force that transports smaller-sized components across the barrier from the inner lane to the outer lane while larger-sized species are retained in the inner lane[207]. In this chapter, we initially focused on inertial effects in the curved microchannel with central barrier and verify how efficiently smaller sized components can cross the barrier and be collected in the outlet. We unexpectedly find that unequal depths of two parallel flows also contributes a significantlyto separation performance. When the interplay between these effects is considered, we found that performance can be enhanced beyond what is possible if either mechanism is applied alone. Separation efficiency was quantified and the flow mechanism was verified by tracking motion of fluorescent particles in three scenarios: (1) curved channel with equal depth, (2) straight channel with unequal depth, and (3) curved channel with unequal depth. High-throughput harvesting of blood components and cancer cells through separation devices demonstrates the feasibility of biological and clinical applications.

6.2 Limitation

Passive separation in mirofluidic systems without external equipment which purely relies on flow phenomena and channel geometry has been widely studied and

applied to separate blood components[208-212], microorganisms[213, 214] and even rare cells[125, 128, 215-217]. However, a critical problem emerges when using microfluidic device as filter to separate particles or cells from mixture because the most common fabrication method is soft lithography utilizing PDMS (polydimethylsiloxane). The soft mechanical property of the PDMS elastomer often limits filtration performance due to deformation of the channel structures. The difficulty to fabricate complex microstructure geometries constrains further development of these systems.

To overcome these limitations described above, we have developed a novel fabrication method employing enzymatic etching on the rigid biodegradable material polylactic acid (see Chapter V). Instead of forcing a particle- or cell-laden suspension to flow through tiny pores in a membrane filter, this design employs a weir-like centerline barrier embedded within a microchannel. In this way, the resulting secondary forces either by centrifugal or pressure difference act to transport the suspended components across the centerline barrier from the inside wall to the outside wall, with only those smaller than the barrier gap able to pass across. In this chapter, we study the separation efficiency of microsphere particles by performing the continuous filtration in straight and curved microchannels with an equal or unequal depth on each side of weir structure.

6.3 Even Height Curved Channel

Flow in curved channels has been studied and described in terms of a lift force from the wall, a centrifugal force, a Saffman and Magnus forcers, and Dean vortex flow[218].Lateral particle migration in curved microchannel due to centrifugal effect on the

fluid has recently been studied and applied in separation of different sized particles[219, 220]. This secondary flow, also called Dean flow, is introduced by symmetrically counter rotating vortices in the top and bottom halves of the microchannel and can be characterized in terms of dimensionless "Dean number" κ[207], the secondary flow is quantified by the relative magnitudes of inertial and centrifugal forces to viscous forces. This Dean number can be described as $\kappa = (D_h/2R)^{0.5}Re$, where D_h is the channel hydraulic diameter, R is the flow path radius of curvature, and Re refers to Reynolds number (Re).

To study the effect of secondary flow caused by Dean vortices, we used enzymatic micromachining to construct a curved microchannel with inner and outer lanes interconnected by a micro-scale gap that can only allow particles smaller than a certain size to cross the barrier while larger sized particles remain in the original stream. Here, we used 2 μm diameter fluorescent particles to monitor flow paths in the inner and outer lanes at different flow rates (0.1, 0.5, 1.0, 1.5, 2.0, and 2.5 mL/min). At low flow rates (0.1 mL/min), centrifugal effects are not strong enough to drive lateral particle transport, and the laminar flow profile is maintained along the channel. As the flow rate increases, two counter-rotating vortex profiles are generated separately in both inner and outer lanes in the curved region (**Fig. 6.1a**). Particles then begin to follow the rotating vortices. When the particles in the upper vortex move close to the central gap, the particles are ableto cross the barrier and enter the outer lane.

In **Fig. 6.1b**, the injection of two different dye-labeled streams verified that when at higher flow rate (also high κ), the inner stream near the barrier wall migrates toward

the inner wall while the stream near the inner wall is transported across the central barrier and toward the outer wall. These flowpatterns explain how particles trapped in rotating vortex, this Dean vortex can act the same behavior like dyed streams are transported to the inner wall and subsequently cross the barrier into the outer lane (**Fig. 6.1c**). The barrier structure,therefore, acts as a transverse filter to exclude large particles from entering the outer lane. In straight region before the curved region in barrier embed microchannel, fluid even at high flow rate is still in laminar flow regime characterized by Reynolds number ($Re = VD/\nu << 100$, where V is the flow velocity, D_h is the hydraulic diameter of channel, and ν is the fluid kinematic viscosity). Particles, thus, remain in the inner lane until entering curved region. In **Fig. 6.1d**, the fluorescent particle streamline image shows the agreement of particle migration with the flow pattern observed from dye-labeled streams.

6.4 Uneven Height Straight Channel

In addition to the transverse secondary flow, the viscosity difference between the two injected streams has been studied and applied to analyze diffusion coefficient of small molecules or biological samples[221]. However, parallel flows with a pressure difference between them have not been as widely studied. Since the enzymatic sculpting technique is capable of performing micromachining in cross-section to overcome the current fabrication limitation of complex topologies, we constructed a straight microchannel with two uneven height lanes divided with a central barrier.

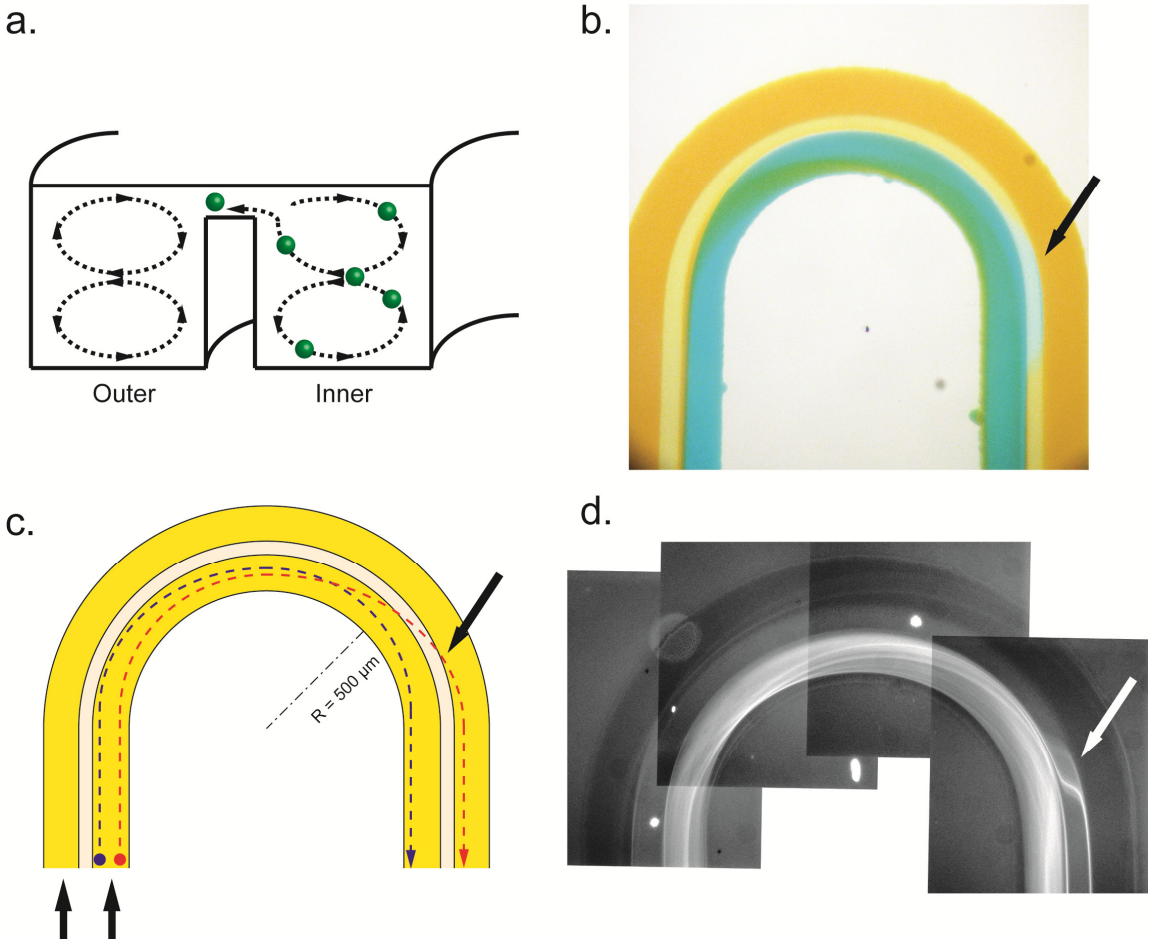

Figure 6.1.Lateral migration of particles in even height of curved channel with central barrier. **(a)** Schematic of barrier embedded microchannel cross section. Dean vortex occurs in curved channel at high flow rate and force small particles travel across the barrier into outer region. **(b)** Top-view image of two streams labeled with blue and yellow dye in a curved microchannel at flow rate of 2 mL/min (inner and outer lanes: 40 µm deep, centerline barrier gap: 5 µm deep, radius of curvature: 500 µm). **(c)** Schematic of the top view of a microchannel and particle movement in curved channel. **(d)** Fluorescence image illustrates 2 µm of particles migrate from inner lane across the barrier to outer lane at flow rate of 2 mL/min.

An initial pressure difference exists between shallow and deep lanes in the entry region can be described by $\Delta P = \Delta P_s - \Delta P_d = \frac{12\mu Q}{h_s{}^3 w}\Delta L - \frac{12\mu Q}{h_d{}^3 w}\Delta L$, where μ represents viscosity of fluid, Q is flow rate, w are the width of lane, h_s and h_d are the heights of shall and deep lanes, respectively, and ΔL means the flow distance along the channel. Thus, the geometry difference of multi-height lane generates a pressure force acting from the shallow lane toward the deep lane which can create additional force to transport particles across the barrier (**Fig. 6.2a**).

This is confirmed by examine the flow pattern of two dye labeled parallel streams, where dye is initially transported across the barrier (**Fig. 6.2b**). This observation is no different when flow rate is higher to 2 mL/min or slower down to 0.1 mL/min. **Fig. 6.2c** shows the effect of this pressure mismatch on particle migration. The initial migration from the shallow lane to the deep lane follows the dye flow (**Fig. 6.2d**). These separated particles become focused at high flow rates (or high *Re*) along the channel wall. Farther downstream,the pressure difference becomes equalizedand particles in deep region concentrate near the barrier where they are influenced by life force and are able to migrate back into the shallow region (**Fig. 6.2e**).

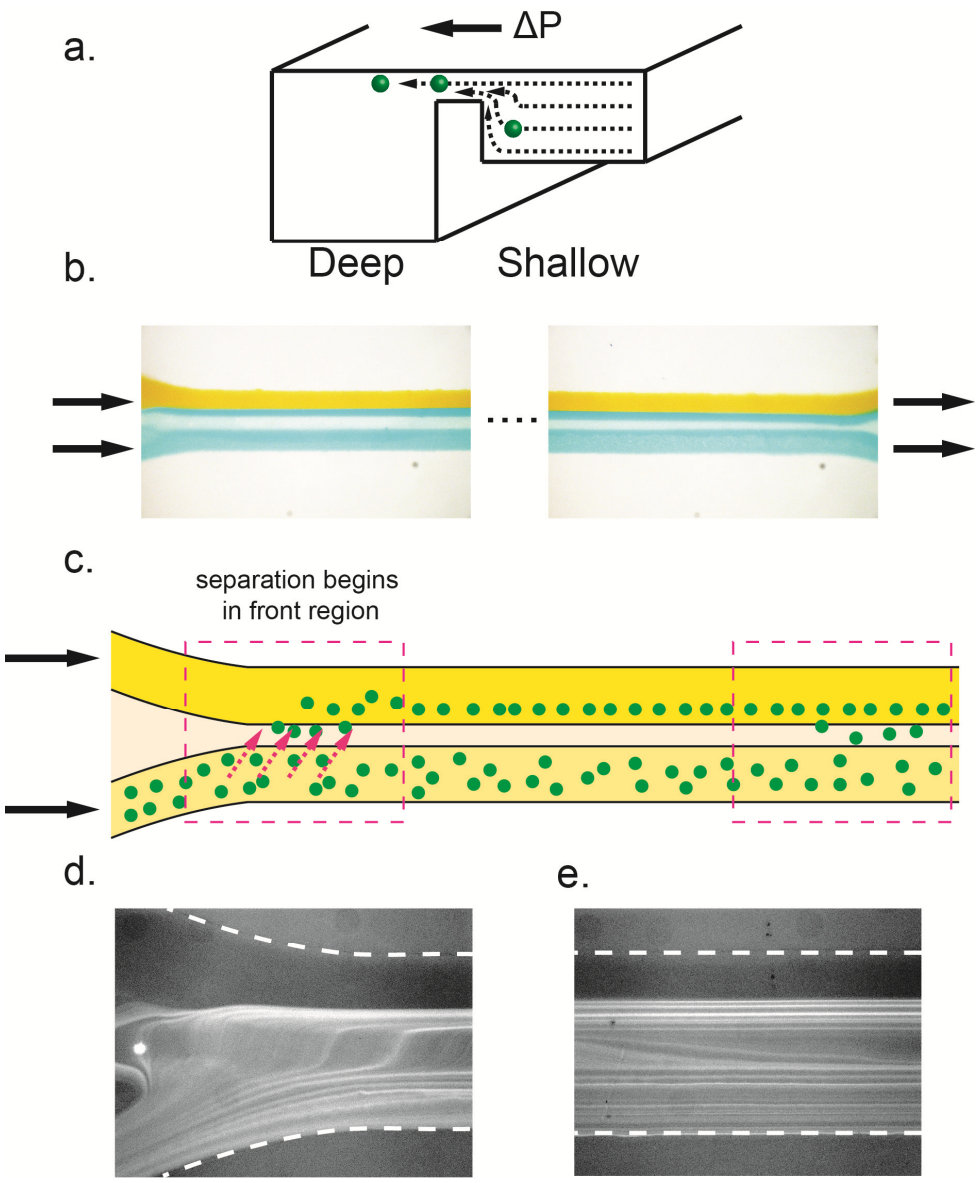

Figure 6.2.Barrier embedded in straight channels with height difference. **(a)** Schematic of cross section of uneven height straight microchannel. **(b)** Two streams labeled with blue and yellow dye in a straight microchannel at the flow rate of 2 mL/min (shallow and deep lanes: 20 µm and 40 µm, respectively, centerline barrier gap: 7 µm deep). **(c)** Two parallel streams were co-injected into uneven height of microchannels. Sample stream was injected through sallow lane while buffer stream was in deep lane. **(d)** Separation of particles happens initially in upstream of channel. The particles across the barrier in deep lane start focusing along the barrier wall at high flow rate. **(e)** In the downstream region, particles can move freely from deep lane back to shallow channel.

6.5 Combination of Uneven Height and Curved Channels

In the previous care of an uneven height straight channel, particle transport in the downstream region becomes randomly distributed as the lateral pressure difference equalizes. We, therefore, explored incorporating a curved region into this "free" movement zone to generate secondary flow that reinforces particle migration to enhance separation efficiency (**Fig. 6.3a**). In **Fig. 6.3b**, small portion of blue dye can cross barrier in the entry section of channel to the outer lane due to the effect of pressure difference caused by uneven height and continue to move outward due to the Dean force at high flow rates.

In **Fig. 6.3c**, we can observe the corresponding particle trajectories. Initially, particles are transported to the outer lane by the pressure difference due to uneven heights. Once the particles cross the barrier, they also experience a transverse Dean flow upon entering the curved region.This makes it difficult for the separated particles to re-enter the sample stream (**Fig. 6.3d**). In this design, the passive secondary flow caused by pressure difference of uneven height acts together with the Dean flow together to achieve enhancement of particle separation.

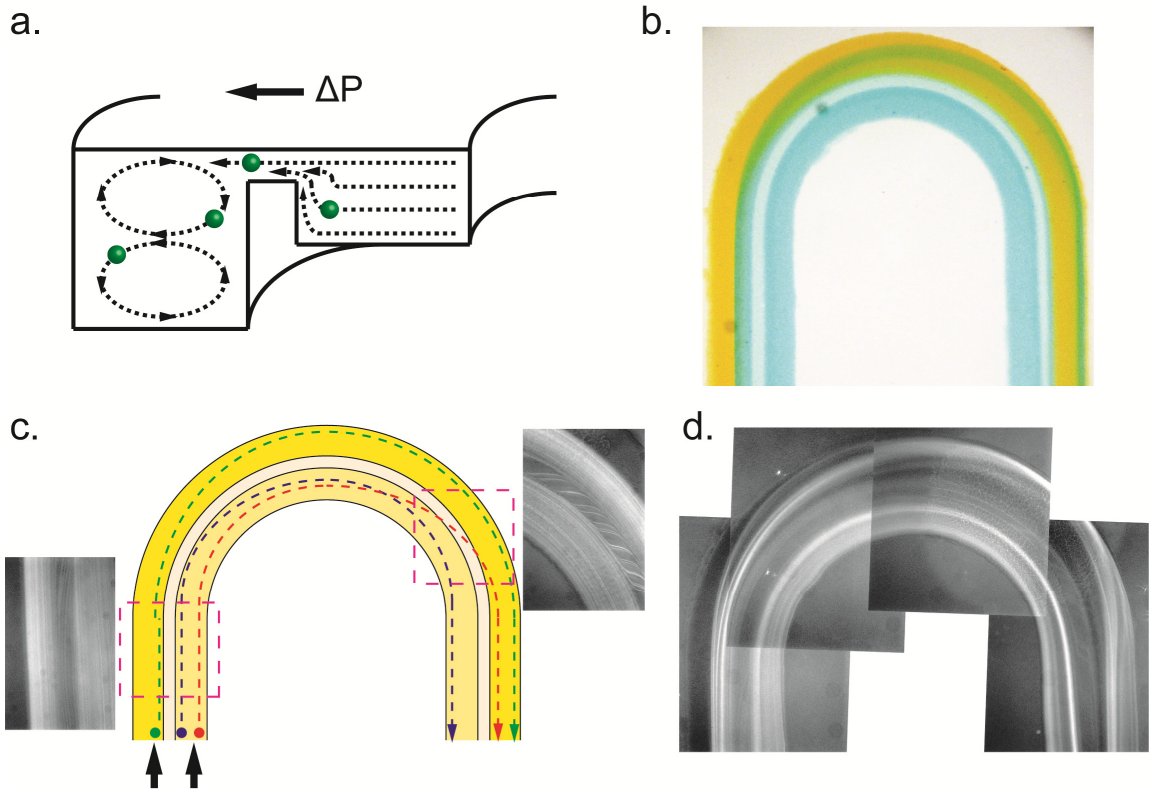

Figure 6.3.An advanced separation device incorporated with uneven and curved channels. **(a)** A schematic of the cross section shows the primary separation driven by height difference and the secondary separation driven by curved geometry can enhance the migration of particles. **(b)** Two streams labeled with blue and yellow dye in a straight microchannel at the flow rate of 2 mL/min (shallow and deep lanes: 20 µm and 40 µm, respectively, centerline barrier gap: 7 µm deep, radius of curvature: 500 µm). **(c)** The fluorescent image of particle stream confirmed the assumption of particle migration. **(d)** Top view of fluoresce stream image to show overall movement of particles.

6.6 Separation Efficiency

To determine separation efficiency, separated particles were collected from two outlet streams and analyzed by Coulter counter and hemocytometer. Separation efficiency is quantitatively defined as the fraction of particles that cross the barrier N_b / N_s= (C_b x V_b) / (C_s x V_s), where N_b and N_s are total number of particles collected in buffer stream and sample stream, respectively. C_b and C_s are particle concentration of buffer and sample stream measured by Coulter counter. V_b and V_s are total volume of buffer and sample collected at the same time. This observation was also evaluated by the computational simulation calculated by STAR-CCM+ (CD-adapco) to verify the fraction of 2 μm particlescrossing the barrier to the outer lane. In **Fig. 6.4a**, the separation efficiency of an even height curved channel is low. As the flow rate increases the transverse Dean vortices enhance separation by transporting more particles across the barrier. Although the separation efficiency is still below 5% at high flow rates, it gives us a clue that the Dean force in the curved region cannot act alone asthe major force to separate particles but can enhance the efficiency at high flow rates.

Separation efficiencies in multi-height channels with a central embedded barrier are dramatically increased.The transverse force caused by the entry pressure difference significantly impacts particle separation. Unlike other passive hydrodynamics in microchannels (i.e. diffusion dominated cross-flow filtration), this transverse pressure drop driven by uneven height lanes provides a new separation concept simply affected by channel geometry. In **Fig. 6.4b**, at low flow rate (0.1 mL/min), the particle separation efficiency increases to about 70%. However, when the flow rate is increased to 2

mL/min, the separation efficiency drops 10-20 % because the particles tend to focus near the centerline barrier and experience a shorter residence time to cross the barrier.

According to the previous equation described internal pressure in a rectangular microchannel, pressure drop is inversely proportional to the cube of channel height if at the same flow rate, and even a slight change of height difference will cause channel pressure gradient with a large scale of change. To verify this hypothesis, we constructed another separation device with smaller channel height difference (40-7-30 (deep-gap-shallow) μm) to observe the separation efficiency caused by channel height and obtained separation efficiency from counting of particles in inner and outer lanes. From **Fig. 6.4c** the separation efficiency drops almost two times (from 70 % to 35 %) at lower flow rate (0.1 mL/min). Similar separation efficiency is also observed when increasing of flow rate.

By combining pressure and Dean forces, lateral particle migration and separation efficiency can be enhanced up to 80 %,even at high from rates (**Fig. 6.4d**). Compared to all of the separation efficiency data, we can conclude that the pressure drop force caused by the channel height difference is the major driving force to induce migration of particles across the barrier. But, the Dean force in the curved channel also plays a crucial role in dispersing the separated particles after the entry pressure difference becomes equalized.

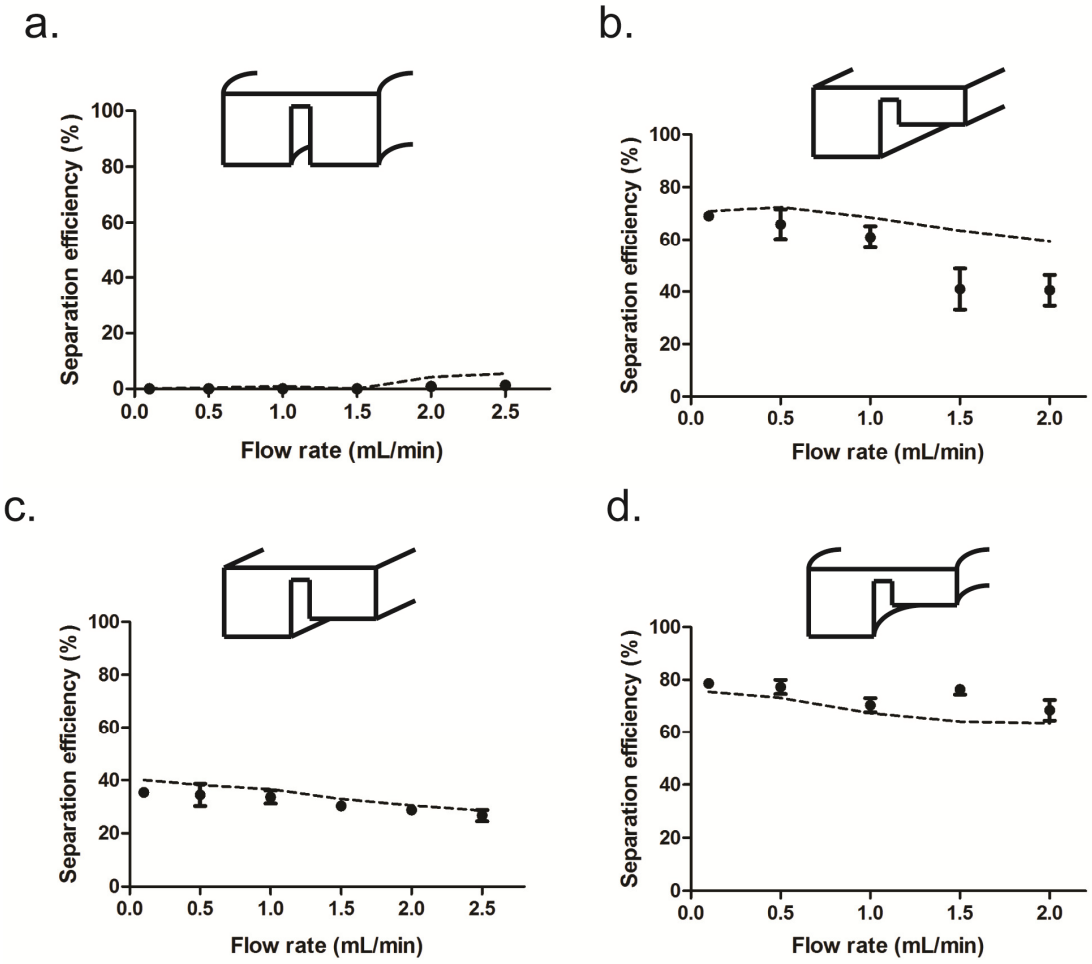

Figure 6.4.**Separation efficiency of particles in different scenarios of microfluidic separators**. Output samples were collected and analyzed to obtain separation efficiency at different flow rate. Experimental (dots) and computational simulation (dash line) results show in **(a)** curved microchannel with 40-5-40 (inner-gap-outer) μm of cross section; **(b)** straight microchannel with 40-7-20 (deep-barrier-shallow) μm; **(c)** straight microchannel with 40-7-30 (deep-barrier-shallow) μm; **(d)** curved microchannel with 40-7-20 (inner-gap-outer) μm. All experimental data were analyzed from three different devices.

6.7 MembranelessMicrofluidic Filtration

After knowing the separation mechanism, we next constructed a membraneless filter employing a tunable weir-like centerline barrier embedded within a microchannel that follows a curved flow path by enzymatic micromachining(**Fig. 6.5a**). In this way, the resulting centrifugal forces act to transport suspended components across the centerline barrier from the inside wall to the outside wall[207], with only those smaller than the barrier gap able to pass across. This separation mechanism is distinct from conventional cross-flow filtration methods where devices are specifically designed to suppress inertial effects[125, 129, 130, 222, 223]. The membraneless arrangement does not impose an excessive pressure drop and is less susceptible to clogging because the barrier is oriented parallel to the flow direction rather than perpendicular to it so that the primary flow continually sweeps material downstream. This approach is most effective at high flow rates where the curvature-induced forces are maximized, making it ideally suited for high-throughput processing of large sample volumes.

We assessed filtration efficiency by injecting a mixture of fluorescent polystyrene beads of diameter 3 and 10 μm (1.68×10^6 and 4.55×10^4 particles/mL, respectively; 1:37 concentration ratio) into the inner inlet of the microchannelshown in **Fig. 6.5a**at a flow rate of 1.2 mL/min (water was co-injected into the outer inlet at the same flow rate),), after which samples were collected at outlets positioned at the inner and outer sides of the centerline barrier and analyzed by fluorescence microscopy (**Fig. 6.5b**). Separation was observed above a threshold flow rate of about0.1 mL/min, consistent with the combination of pressure difference and Dean flow effect. Under these

conditions, the 10 μm beads were unable to pass across the barrier and were therefore confined to the inner outlet, while the outer outlet contained only 3 μm beads—the only species able to cross the barrier. Analysis of serial dilutions using flow cytometry demonstrated ability to isolate the 10 μm beads with > 98% normalized efficiency at a concentration ratio of 10^4 (**Fig. 6.6**).

Inertially driven flow and particle migration in conduits with complex asymmetric cross sectional geometries has been investigated by observing the particle streams. Furthermore, key features of the underlying flow phenomena governing filtration can also be inferred from 3D computational fluid dynamics simulations in the same geometry of previous device (**Fig. 6.7a**). The circulatory flow field established in the curved segment of the microchannel provides a centrifugal driving force for transport from the inner half to the outer half of the curved flow path—an effect that is enhanced by the unequal depths on each side of the central barrier (**Fig. 6.7b**). The simulation of velocity field result gave us an overlook that the secondary flow was directed from inner lane toward outer lane. In addition, the symmetrically counter rotating vortices occurred in curved region can be demonstrated in different aspect ratio of channels. The resulting particle advection becomes evident from Lagrangian tracking of 3 μm diameter beads, indicating that 61% are transported from the inner to the outer channel by the time they reach the end of the curved segment (**Fig. 6.7c**).

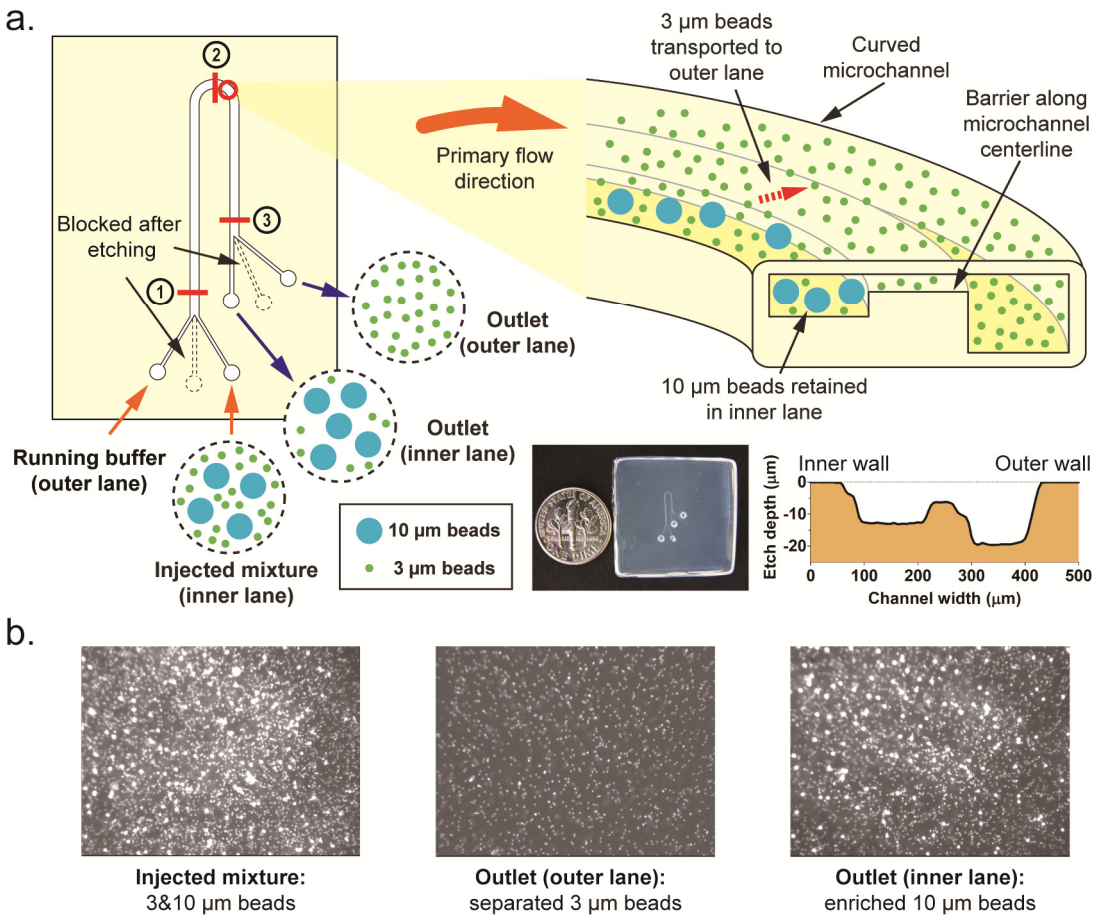

Figure 6.5.Size-selective filtration of a mixture of 3 and 10 μm beads.(a) Schematic and cross-sectional profile of a U-shaped microchannel fabricated using the method shown in Fig. 5.5. The width and radius of curvature of the microchannel are 300 and 500 μm, respectively. The depths of the inner and outer channels are 13 μm and 20 μm, respectively, while the centerline has a 6 μm barrier gap. The central machining port was blocked during filtration.Above a sufficiently high flow rate, the 3 μm beads are driven across the 6 μm barrier by secondary centrifugal flow established in the curved microchannel segment. The 10 μm beads are filtered by remaining confined in the inner flow lane. **(b)** A mixture of 3 μm (1.68×10^6 particles/ml) and 10 μm (4.55×10^4 particles/ml) fluorescent microspheres is injected through inner channel of the U-shape device at 1.2 mL/min. Only 3 μm beads were collected in outer outlet (no 10 μm beads were observed in 3 ml of collection). Enriched and concentrated 10 μm beads are collected from the inner outlet.

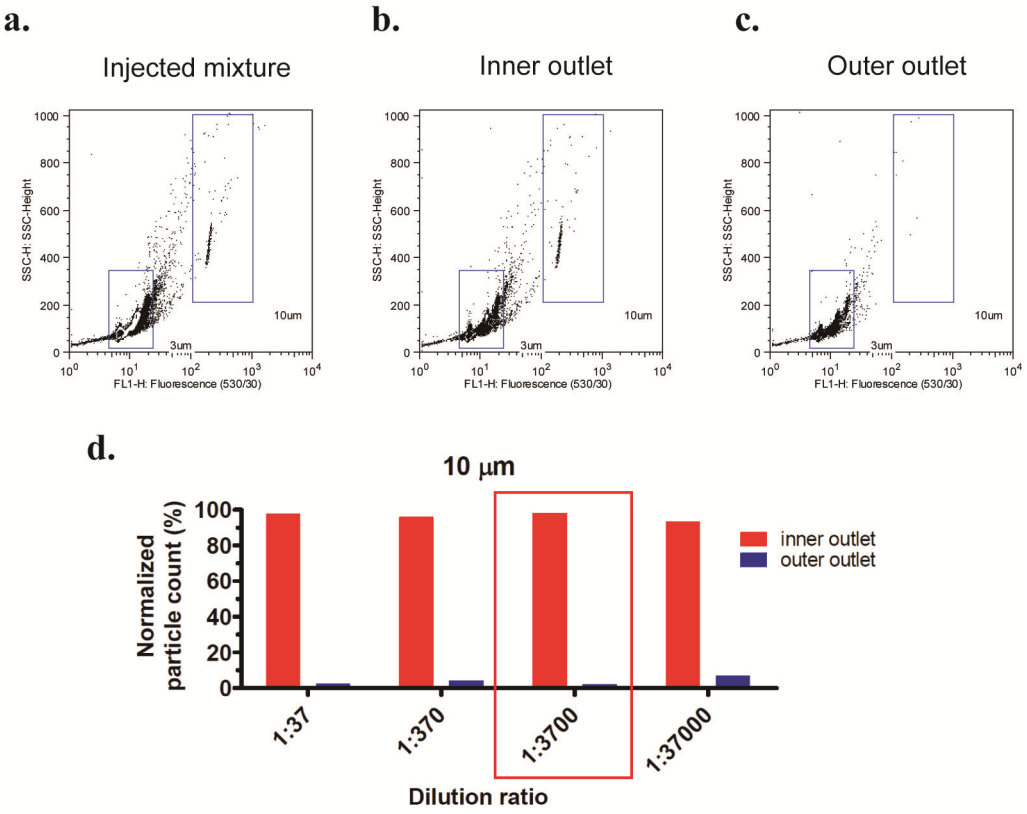

Figure 6.6.Analysis of particle separation capability.Flow cytometry data are shown for **(a)** the injected mixture of 3 and 10 µm beads at concentrations of 1.68 x 10^6 and 4.55 x 10^2 particles/mL, respectively; **(b)** the sample collected from the inner outlet; and **(c)** the sample collected from the outer outlet. **(d)** Normalized particle counts of 10 µm beads recovered from the inner outlet. Data are shown for mixtures injected at concentration ratios of 3:10 µm beads ranging from 1:37 to 1:37,000. The red box denotes conditions shown in (a–c), where the collection efficiency approaches 100%. Beads were analyzed on a FACSCalibur flow cytometer (Becton Dickinson), equipped with a 15 mW air-cooled argon laser, using CellQuest acquisition software. Green fluorescence was collected through a 530/30 nm bandpass filter. List mode data were acquired and analyzed using FlowJo (version 8.8.6, Treestar, Inc.).

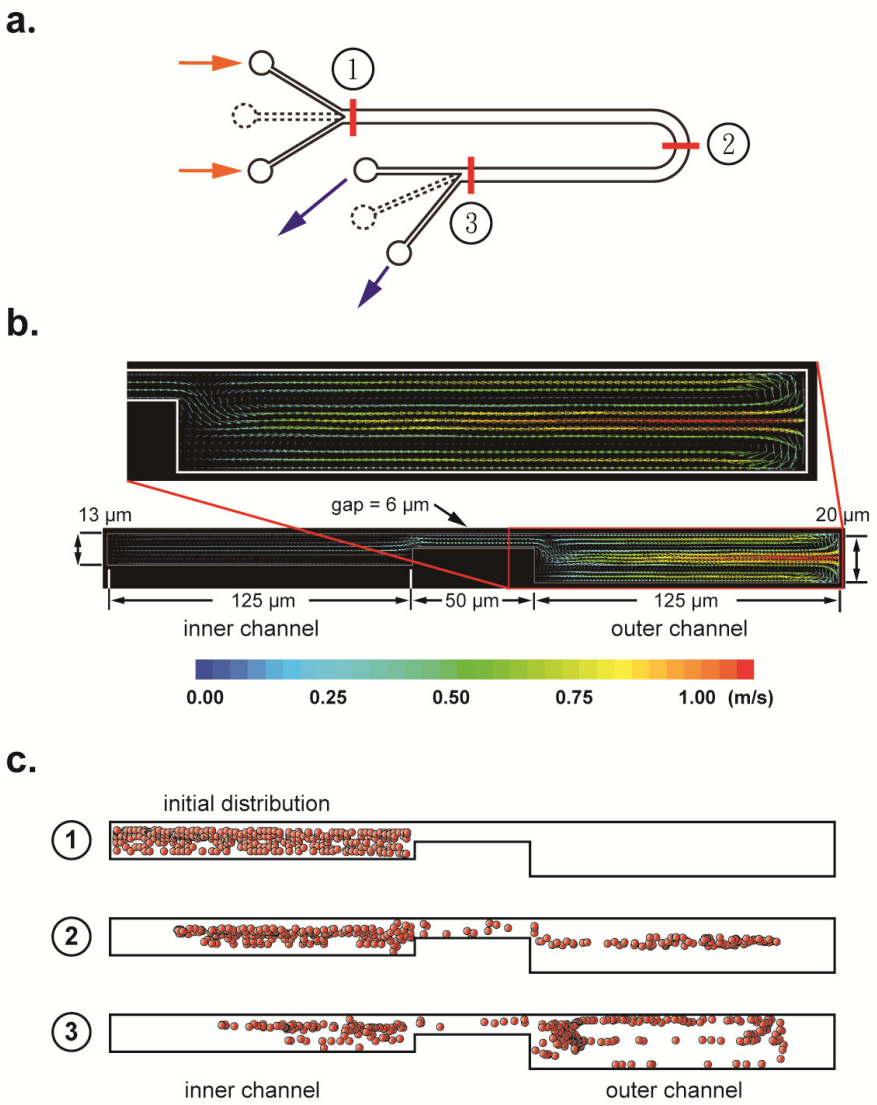

Figure 6.7.Computational simulation of membraneless filtration.(a) Simulated microchannel geometry matching the filtration device shown in Fig. 6.5. **(b)** Cross-sectional view of the steady-state transverse component of the velocity field in the curved segment (position 2). Distinct counter-rotating vortices are evident on each side of the centerline barrier (500 µm radius of curvature, 1 mL/min flow rate). **(c)**Lagrangian tracking analysis shows the transport of 3 µm particles from the inside to the outside of the curved flow path as they travel from inlet (position 1) to outlet (position 3)

To demonstrate practical application, we next used this filtration device to harvest PC3 human prostate cancer cells (20–30 μm diameter) from whole blood (injected component densities: PC3-1.43x10^6 cells/mL, WBC-1.22x10^6 cells/mL, RBC-7.32x10^8 cells/mL) (**Fig. 6.8a**). The PC3-spiked blood sample was injected into the inner lane at 1 mL/min (PBS was co-injected into the outer lane at the same flow rate) and separated samples were collected from inner outlet and outer outlet.In **Fig. 6.8b**, red fluorescent dyed PC3 cells were collected in inner outlet and none of PC3 cells were observed in outer outlet. To be noticed, when collected cells were observed under a microscope, sample collected in inner outlet showed higher cell density and has a half reduction of volume compared to the original cell mixture injected from inner inlet.

In order to quantitatively verify the device performance, the collected samples were analyzed by cell counting methods. Cell counts indicate that PC3 cells were harvested with more than 99% efficiency and 1.6-fold enrichment upon recovery from the inner lane (45% of RBCs, 4% of WBCs, and less than 1% of PC3 cells cross to the outer lane in **Fig.6.8c**). The enriched cells were maintained in the as-injected blood environment with no discernible change in viability (before filtration: 98.7 ± 0.6%, n = 3; after filtration: 98.9 ± 0.1%, n = 3; **Fig.6.8d**).

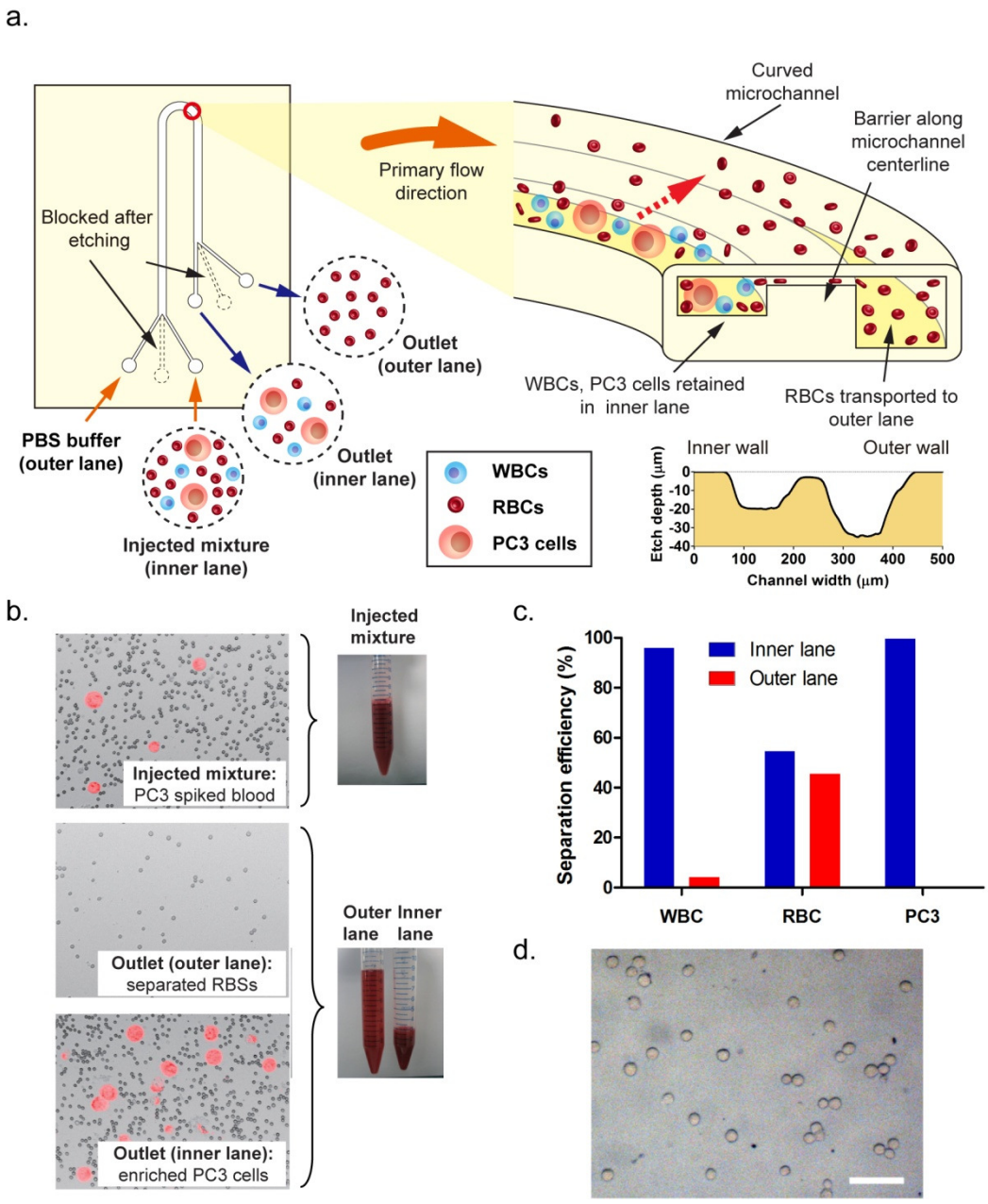

Figure 6.8.An enzymatically machined membraneless architecture enables high-throughput cell harvesting. **(a)** Illustration and cross-sectional profile (inner and outer lanes: 20 and 35 mm deep, respectively, centerline barrier gap: 3 mm deep, radius of curvature: 500 mm). **(b)** Separation of whole blood spiked with PC3 cancer cells at 1 mL/min, showing isolation and enrichment of PC3 cells from whole blood (inner lane). **(c)** Cell-count data show the relative fractions of WBCs, RBCs, and PC3 cells recovered at the inner lane. **(d)** Viability of PC3 cells is unchanged after filtration (trypan blue assay, viable cells unstained; bar, 50 mm).

6.8 Summary

We demonstrate size-based isolation and enrichment of cells from whole blood with throughput 1 – 2 orders of magnitude faster than currently possible. Separation is achieved using an enzymatically machined filtration architecture that uniquely merges the high selectivity of a physical membrane barrier with the ability to operate at high flow rates (mL/min range). This design makes it possible to process large volumes with no clogging, while simultaneously preserving cell viability.

CHAPTER VII

CONCLUSIONS

The novel fabrication methods described in this dissertation has make new contributions toward the goal of producing 3D microchannel networks mimicking the features of physiological vasculature.These techniques are likely to play a key role in enabling culture of functional organ-sized engineered tissues.A key future challenge will be to ensure convergence between the science and engineering associated with these microchannel network construction approaches, and the biology associated with incorporating this technology into the broader scope of life science applications. This shift toward the biological aspects of the problem introduces new considerations. For example, as the complexity of tissue engineering constructs continues to evolve it becomes increasingly important to maintain some degree of standardization with respect to experimental conditions. This is evident when considering the array of conditions already employed in microchannel-based cell culture studies. Meaningful comparisons between results obtained by different research groups are possible only if common cell types and culture conditions are consistently employed. Improved methods to seed and culture cells in extended 3D spaces also need to be developed and refined. Current microscopy-based approaches to observe cell culture in thin planar multiwell plate formats are inadequate to probe conditions deep within the interior of cm-sized constructs. Other key challenges involve embedding vasculature into porous scaffold substrates and developing methods amenable to mass production. Overcoming these

barriers promises to set the stage for a host of exciting developments in the field of tissue engineering during the coming years.Specific conclusions of all investigations described in this dissertation are summarized below.

7.1 Electrostatic Discharge Constructed 3D Microvascular Networks

The qualitative and quantitative resemblance of these branched 3D microchannel networks to anatomical vascular trees is remarkable in terms of both global architecture and local morphology. In addition to providing a convenient platform to study transport and flow in branched 3D microfluidic networks, these similarities introduce the exciting possibility of harnessing electrostatic discharge phenomena as a new tool to embed vascular networks in tissue scaffold materials so they can support cell culture throughout much larger volumes than are currently possible. Unlike conventional microfabrication processes, this method enables large-scale bio-inspired 3D flow networks containing a wide range of channel dimensions to be instantaneously constructed in a straightforward non-serial manner amenable to mass-production.

7.2 Air Deformation Process Enlarged 3D Microvascular Networks

Inflation process makes it possible for fabrication of artificial microvascular networks which can mimic the living system via a simple and rapid method. Unlike conventional microfabrication processes, hot-molding and pressurized air inflation methods together enable a bio-mimicked flow networks containing a desired range of channel dimensions to be simply constructed from 2D patternablemicrochannels. This

deformation process is also tunable globally increase the diameters of every channel inside a thermoplastic PLA substrate andmicrochannels with rectangular cross section to deform into circular as well as elliptic. The morphology of microchannelscan be further tuned by manipulating properties of rubbery nature of the thermoplastic polymer. For example, polypropylene and polystyrene are other thermoplastic polymers can also be used by those methods to construct circular 3D microvascular networks for a variety of biological mass transported applications.

Moreover, we have successfully applied this technique to not only enlarge the channels diameter but also to smoothen the channel walls ofphysiologically similar 3D vasculature fabricated by electrostatic discharge. Finally, we showed that endothelial cells can be seeded and cultured inside biocompatible and biodegradable polymer PLA to form an endothelial layer around branched and interconnected microchannels. We believe that this microvascular device combined with an automated circulating perfusion system can as a platform to study rheology of blood flow potential drug discovery.

7.3 Enzymatic Sculpted Surface Topographies

Enzymatic machining introduces an unexplored avenue to fashion molecularly imprinted surface features mimicking those in living systems via a simple process that can be accessed in virtually any laboratory. More broadly, the highly-specific nature of the governing interactions lays a foundation to exquisitely control the templatednano-scale morphologies by manipulating properties of the enzyme and substrate. For example, various classes of biodegradable polymers are selectively machined by

different enzymes For example, polycaprolactone (PCL) can be degraded by lipase[224], and numerous strains of the bacterial classes *Firmicutes* and *Proteobacteria* can degrade PCL, polyhydroxybutyrate, and polybutylene succinate[225]. These interactions can be further tuned by engineering enzymes displaying enhanced activities and specificities that can be toggled in response to environmental cues, as well as by employing substrates containing assembled crystalline morphologies.

7.4 MembranelessHigh-Throughput Cell Separation

A key benefit of our approach is the capability for highthroughput operation, and this can be seen upon comparison with existing methods for isolation of rare-cell biomarkers relevant to cancer (for example, circulating tumor cells (CTCs); **Table 7.1**; results are expressed in terms of normalized throughput representing the time to process 1 mL of undiluted whole blood). Not only is our approach orders of magnitude faster than comparable methods, it also delivers 99.2 ± 0.2% (n = 3) retention of PC3 cells from spiked whole blood and 99.7 ± 0.5% (n = 3) when dispersed in PBS buffer. No additional steps are required to retrieve the separated cells, in contrast to conventional membrane or affinity capture approaches. These advantages suggest considerable untapped potential to enable a wide range of blood-cell analysis applications where harvesting throughput is currently a limiting constraint (for example, granulocyte isolation[204, 226]cancercell analysis[119]).

In the context of CTC analysis, we remark that immunoselection (the current gold standard) requires pre-programming with antibodies to enable recognition of

specific epithelial antigens expressed by CTCs, thus limiting the ability to capture different cell types and introducing the possibility of retaining non-malignant cells. Optimal capture efficiencies are achieved by applying low flow rates and increasing the binding surface area (requiring more antibodies), with additional wash steps and reagents necessary to recover the captured cells. CTCs have also been efficiently separated by dielectrophoresis, but the cells must be dispersed in isotonic buffers at high dilution, and low flow rates are required. Physical barrier filtration architectures also achieve high separation efficiency, but high dilution and low flow rates are needed to prevent clogging. Methods exploiting other hydrodynamic effects also generally require high dilution and often operate within a narrow "sweet spot" of cell size and flow rate. Our approach overcomes these throughput limitations because separation occurs optimally at high flow rates, with considerable potential for further improvement by employing multistage designs that sequentially feed the enriched effluent into additional downstream filtration elements. Multiple weirs with different widths, depths, and gaps can also be arrayed in parallel to process multicomponent mixtures.

Table 7.1.Comparison of microfluidic-based CTC enrichment methods.
(Normalized throughput represents the time to process 1 mL of undiluted whole blood)

Method	Flow Rate (reported)	Dilution Factor	Normalized Throughput (mL min^{-1})	CTC recovery	Ref.	Comments
This work	**1 mL min^{-1}**	**5**	**0.2**	**99 %**	**–**	• **Optimal operation at high flow rates**
Immunoselection(bead-based)	10 mL h^{-1}	> 1*	unknown*	90 %	227	• Antibody-based • Additional washing
	240 µL min^{-1}	> 1*	unknown*	85 %	228	
Immunoselection(micropost array)	1 mL h^{-1}	1	0.017	65–80 %	119	• Antibody-based • Low volume capacity
	1 mL h^{-1}	1	0.017	95 %	229	
	2 mL h^{-1}	1	0.03	92 %	230	
Dielectrophoresis	1.5 ml min^{-1}	40,000	3.75 x 10^{-5}	90 %	121	• Special buffer conditions
	126 µL min^{-1}	400	3.15 x 10^{-4}	75 %	231	
Physical barrier						• Dilution and/or low flow rate operation needed to avoid clogging
• Pool-dam	0.1 mL min^{-1}	5,000	2 x 10^{-5}	99 %	125	
• Isolation wells	0.7 mL h^{-1}	3	3.9 x 10^{-3}	80 %	128	
Hydrodynamics						• Dilution and/or low flow rate operation needed to avoid clogging
• Expansion/ contraction	0.4 mL min^{-1}	20	0.02	80 %	232	
• Microvortex trapping	4.5 mL min^{-1}	40	0.11	85 %	233	

* Normalized throughput is difficult to assess due to the incubation, washing, and resuspensionsteps inherent to bead-based capture protocols.

REFERENCES

1. Fidkowski, C. et al. Endothelialized microvasculature based on a biodegradable elastomer. *Tissue Engineering***11**, 302-309 (2005).

2. King, K.R., Wang, C.C.J., Kaazempur-Mofrad, M.R., Vacanti, J.P. & Borenstein, J.T. Biodegradable microfluidics. *Advanced Materials***16**, 2007-2012 (2004).

3. Johnson, T.J., Ross, D. & Locascio, L.E. Rapid microfluidic mixing. *Analytical Chemistry***74**, 45-51 (2002).

4. Stroock, A.D. et al. Chaotic mixer for microchannels. *Science***295**, 647-651 (2002).

5. Howell, P.B. et al. A microfluidic mixer with grooves placed on the top and bottom of the channel. *Lab on a Chip***5**, 524-530 (2005).

6. Palsson, B. & Bhatia, S. Tissue engineering. (Pearson Prentice Hall, Upper Saddle River, N.J.; 2004).

7. Roger Heart Disease and Stroke Statistics-2011 Update: A Report From the American Heart Association (vol 123, pg e18, 2011). *Circulation***123**, E240-E240 (2011).

8. Griffith, L.G. & Swartz, M.A. Capturing complex 3D tissue physiology in vitro. *Nature Reviews Molecular Cell Biology***7**, 211-224 (2006).

9. Peters, M.C., Polverini, P.J. & Mooney, D.J. Engineering vascular networks in porous polymer matrices. *Journal of Biomedical Materials Research***60**, 668-678 (2002).

10. Vozzi, G., Flaim, C., Ahluwalia, A. & Bhatia, S. Fabrication of PLGA scaffolds using soft lithography and microsyringe deposition. *Biomaterials***24**, 2533-2540 (2003).

11. Wu, X. et al. Tissue-engineered microvessels on three-dimensional biodegradable scaffolds using human endothelial progenitor cells. *American Journal of Physiology-Heart and Circulatory Physiology***287**, H480-H487 (2004).

12. Lavik, E. & Langer, R. Tissue engineering: current state and perspectives. *Applied Microbiology and Biotechnology***65**, 1-8 (2004).

13. Van Eijk, F. et al. Tissue engineering of ligaments: A comparison of bone marrow stromal cells, anterior cruciate ligament, and skin fibroblasts as cell source. *Tissue Engineering***10**, 893-903 (2004).

14. Vunjak-Novakovic, G., Altman, G., Horan, R. & Kaplan, D.L. Tissue engineering of ligaments. *Annual Review of Biomedical Engineering***6**, 131-156 (2004).

15. Waldman, S.D., Spiteri, C.G., Grynpas, M.D., Pilliar, R.M. & Kandel, R.A. Long-term intermittent compressive stimulation improves the composition and mechanical properties of tissue-engineered cartilage. *Tissue Engineering***10**, 1323-1331 (2004).

16. Freed, L.E. et al. Advanced tools for tissue engineering: Scaffolds, bioreactors, and signaling. *Tissue Engineering***12**, 3285-3305 (2006).

17. Griffith, L.G. & Naughton, G. Tissue engineering - Current challenges and expanding opportunities. *Science***295**, 1009-1014 (2002).

18. Kellner, K. et al. Determination of oxygen gradients in engineered tissue using a fluorescent sensor. *Biotechnology and Bioengineering***80**, 73-83 (2002).

19. Colton, C.K. Implantable Biohybrid Artificial Organs. *Cell Transplantation***4**, 415-436 (1995).

20. Labarbera, M. Principles of Design of Fluid Transport-Systems in Zoology. *Science***249**, 992-1000 (1990).

21. West, G.B., Brown, J.H. & Enquist, B.J. A general model for the origin of allometric scaling laws in biology. *Science***276**, 122-126 (1997).

22. Nerem, R.M. & Seliktar, D. Vascular tissue engineering. *Annual Review of Biomedical Engineering***3**, 225-243 (2001).

23. Rheinwald, J.G. & Green, H. Formation of a Keratinizing Epithelium in Culture by a Cloned Cell Line Derived from a Teratoma. *Cell***6**, 317-330 (1975).

24. Murray, C.D. The Physiological Principle of Minimum Work. I. The Vascular System and the Cost of Blood Volume. *Proceedings of the National Academy of Sciences of the USA***12**, 207-214 (1926).

25. LaBarbera, M. Principles of Design of Fluid Transport Systems in Zoology. *Science***249**, 992-1000 (1990).

26. West, G.B., Brown, J.H. & Enquist, B.J. A General Model for the Origin of Allometric Scaling Laws in Biology. *Science***276**, 122-126 (1997).

27. Emerson, D.R., Cieslicki, K., Gu, X. & Barber, R.W. Biomemetic Design of Microfluidic Manifolds Based on a Generalized Murray's Law. *Lab on a Chip***6**, 447-454 (2006).

28. Restrepo, J.G., Ott, E. & Hunt, B.R. Scale dependence of branching in arterial and bronchial trees. *Physical Review Letters***96**, 128101 (2006).

29. Kassab, G.S. Scaling laws of vascular trees: of form and function. *American Journal of Physiology-Heart and Circulatory Physiology***290**, H894-H903 (2006).

30. Vanbavel, E. & Spaan, J.A.E. Branching Patterns in the Porcine Coronary Arterial Tree - Estimation of Flow Heterogeneity. *Circulation Research***71**, 1200-1212 (1992).

31. Huang, W., Yen, R.T., McLaurine, M. & Bledsoe, G. Morphometry of the human pulmonary vasculature. *Journal of Applied Physiology***81**, 2123-2133 (1996).

32. Mittal, N. et al. Analysis of blood flow in the entire coronary arterial tree. *American Journal of Physiology-Heart and Circulatory Physiology***289**, H439-H446 (2005).

33. Gafiychuk, V.V. & Lubashevsky, I.A. On the principles of the vascular network branching. *Journal of Theoretical Biology***212**, 1-9 (2001).

34. Borenstein, J.T. et al. Microfabrication technology for vascularized tissue engineering. *Biomedical Microdevices***4**, 167-175 (2002).

35. Kaihara, S. et al. Silicon micromachining to tissue engineer branched vascular channels for liver fabrication. *Tissue Engineering***6**, 105-117 (2000).

36. Duffy, D.C., McDonald, J.C., Schueller, O.J.A. & Whitesides, G.M. Rapid prototyping of microfluidic systems in poly(dimethylsiloxane). *Analytical Chemistry***70**, 4974-4984 (1998).

37. Wang, G.J., Chen, C.L., Hsu, S.H. & Chiang, Y.L. Bio-MEMS fabricated artificial capillaries for tissue engineering. *Microsystem Technologies-Micro-and Nanosystems-Information Storage and Processing Systems***12**, 120-127 (2005).

38. Wang, G.J., Hsu, Y.F., Hsu, S.H. & Horng, R.H. JSR photolithography based microvessel scaffold fabrication and cell seeding. *Biomedical Microdevices***8**, 17-23 (2006).

39. Wang, G.J., Ho, K.H., Hsu, S.H. & Wang, K.P. Microvessel scaffold with circular microchannels by photoresist melting. *Biomedical Microdevices***9**, 657-663 (2007).

40. Janakiraman, V., Kienitz, B.L. & Baskaran, H. Lithography Technique for Topographical Micropatterning of Collagen-Glycosaminoglycan Membranes for Tissue Engineering Applications. *J Med Device***1**, 233-237 (2007).

41. Janakiraman, V., Sastry, S., Kadambi, J.R. & Baskaran, H. Experimental investigation and computational modeling of hydrodynamics in bifurcating microchannels. *Biomedical Microdevices***10**, 355-365 (2008).

42. Camp, J.P., Stokol, T. & Shuler, M.L. Fabrication of a multiple-diameter branched network of microvascular channels with semi-circular cross-sections using xenon difluoride etching. *Biomedical Microdevices***10**, 179-186 (2008).

43. Golden, A.P. & Tien, J. Fabrication of microfluidic hydrogels using molded gelatin as a sacrificial element. *Lab on a Chip***7**, 720-725 (2007).

44. Shin, M. et al. Endothelialized networks with a vascular geometry in microfabricated poly(dimethyl siloxane). *Biomedical Microdevices***6**, 269-278 (2004).

45. Carraro, A. et al. In vitro analysis of a hepatic device with intrinsic microvascular-based channels. *Biomedical Microdevices***10**, 795-805 (2008).

46. Ling, Y. et al. A cell-laden microfluidic hydrogel. *Lab on a Chip***7**, 756-762 (2007).

47. Choi, N.W. et al. Microfluidic scaffolds for tissue engineering. *Nature materials***6**, 908-915 (2007).

48. Shevkoplyas, S.S., Gifford, S.C., Yoshida, T. & Bitensky, M.W. Prototype of an in vitro model of the microcirculation. *Microvascular Research***65**, 132-136 (2003).

49. Hoganson, D.M. et al. Principles of Biomimetic Vascular Network Design Applied to a Tissue-Engineered Liver Scaffold. *Tissue Engineering Part A***16**, 1469-1477 (2010).

50. Hoganson, D.M., Pryor, H.I., Bassett, E.K., Spool, I.D. & Vacanti, J.P. Lung assist device technology with physiologic blood flow developed on a tissue engineered scaffold platform. *Lab on a Chip***11**, 700-707 (2011).

51. Gilbert, R.J. et al. Computational and functional evaluation of a microfluidic blood flow device. *Asaio Journal***53**, 447-455 (2007).

52. Borenstein, J.T. et al. Functional endothelialized microvascular networks with circular cross-sections in a tissue culture substrate. *Biomedical Microdevices***12**, 71-79 (2010).

53. Leclerc, E. et al. Fabrication of microstructures in photosensitive biodegradable polymers for tissue engineering applications. *Biomaterials***25**, 4683-4690 (2004).

54. Lim, D., Kamotani, Y., Cho, B., Mazumder, J. & Takayama, S. Fabrication of microfluidic mixers and artificial vasculatures using a high-brightness diode-pumped Nd : YAG laser direct write method. *Lab on a Chip***3**, 318-323 (2003).

55. Emerson, D.R., Cieslicki, K., Gu, X.J. & Barber, R.W. Biomimetic design of microfluidic manifolds based on a generalised Murray's law. *Lab on a Chip***6**, 447-454 (2006).

56. Kam, D.H. & Mazumder, J. Three-dimensional biomimetic microchannel network by laser direct writing. *Journal of Laser Applications***20**, 185-191 (2008).

57. Kam, D.H., Shah, L. & Mazumder, J. Femtosecond laser machining of multi-depth microchannel networks onto silicon. *Journal of Micromechanics and Microengineering***21**, 045027 (2011).

58. Cui, X.F. & Boland, T. Human microvasculature fabrication using thermal inkjet printing technology. *Biomaterials***30**, 6221-6227 (2009).

59. Gillette, B.M. et al. In situ collagen assembly for integrating microfabricated three-dimensional cell-seeded matrices. *Nature materials***7**, 636-640 (2008).

60. Nahmias, Y., Schwartz, R.E., Verfaillie, C.M. & Odde, D.J. Laser-guided direct writing for three-dimensional tissue engineering. *Biotechnology and Bioengineering***92**, 129-136 (2005).

61. Murray, C.D. The physiological principle of minimum work II Oxygen exchange in capillaries. *Proceedings of the National Academy of Sciences of the United States of America***12**, 299-304 (1926).

62. Murray, C.D. The physiological principle of minimum work applied to the angle of branching of arteries. *J Gen Physiol***9**, 835-841 (1926).

63. Bettinger, C.J. et al. Three-dimensional microfluidic tissue-engineering scaffolds using a flexible biodegradable polymer. *Advanced Materials***18**, 165-169 (2006).

64. Kniazeva, T., Hsiao, J.C., Charest, J.L. & Borenstein, J.T. A microfluidic respiratory assist device with high gas permeance for artificial lung applications. *Biomedical Microdevices***13**, 315-323 (2011).

65. Wu, W., DeConinck, A. & Lewis, J.A. Omnidirectional Printing of 3D Microvascular Networks. *Advanced Materials***23**, H178-H183 (2011).

66. Therriault, D., White, S.R. & Lewis, J.A. Chaotic mixing in three-dimensioned microvascular networks fabricated by direct-write assembly (vol 2, pg 265, 2002). *Nature materials***2**, 347-347 (2003).

67. Therriault, D., Shepherd, R.F., White, S.R. & Lewis, J.A. Fugitive inks for direct-write assembly of three-dimensional microvascular networks. *Advanced Materials***17**, 395-399 (2005).

68. Wu, W. et al. Direct-write assembly of biomimetic microvascular networks for efficient fluid transport. *Soft Matter***6**, 739-742 (2010).

69. Toohey, K.S., Sottos, N.R., Lewis, J.A., Moore, J.S. & White, S.R. Self-healing materials with microvascular networks. *Nature materials***6**, 581-585 (2007).

70. Hansen, C.J. et al. Self-Healing Materials with Interpenetrating Microvascular Networks. *Advanced Materials***21**, 4143-4147 (2009).

71. Norotte, C., Marga, F.S., Niklason, L.E. & Forgacs, G. Scaffold-free vascular tissue engineering using bioprinting. *Biomaterials***30**, 5910-5917 (2009).

72. Jakab, K., Neagu, A., Mironov, V., Markwald, R.R. & Forgacs, G. Engineering biological structures of prescribed shape using self-assembling multicellular systems. *Proceedings of the National Academy of Sciences of the United States of America***101**, 2864-2869 (2004).

73. Leclerc, E., Sakai, Y. & Fujii, T. Cell culture in 3-dimensional microfluidic structure of PDMS (polydimethylsiloxane). *Biomedical Microdevices***5**, 109-114 (2003).

74. Asakawa, N. et al. Pre-vascularization of in vitro three-dimensional tissues created by cell sheet engineering. *Biomaterials***31**, 3903-3909 (2010).

75. Koike, N. et al. Creation of long-lasting blood vessels. *Nature***428**, 138-139 (2004).

76. Sieminski, A.L., Was, A.S., Kim, G., Gong, H. & Kamm, R.D. The stiffness of three-dimensional ionic self-assembling peptide gels affects the extent of capillary-like network formation. *Cell Biochemistry and Biophysics***49**, 73-83 (2007).

77. McGuigan, A.P. & Sefton, M.V. Vascularized organoid engineered by modular assembly enables blood perfusion. *Proceedings of the National Academy of Sciences of the United States of America***103**, 11461-11466 (2006).

78. Bellan, L.M. et al. Fabrication of an artificial 3-dimensional vascular network using sacrificial sugar structures. *Soft Matter***5**, 1354-1357 (2009).

79. Miller, J.S. et al. Rapid casting of patterned vascular networks for perfusable engineered three-dimensional tissues. *Nature materials***11**, 768-774 (2012).

80. Lee, W. et al. On-Demand Three-Dimensional Freeform Fabrication of Multi-Layered Hydrogel Scaffold With Fluidic Channels. *Biotechnology and Bioengineering***105**, 1178-1186 (2010).

81. Huang, J.H. et al. Rapid Fabrication of Bio-inspired 3D Microfluidic Vascular Networks. *Advanced Materials***21**, 3567-3571 (2009).

82. Black, A.F., Berthod, F., L'Heureux, N., Germain, L. & Auger, F.A. In vitro reconstruction of a human capillary-like network in a tissue-engineered skin equivalent. *Faseb Journal***12**, 1331-1340 (1998).

83. Gibot, L., Galbraith, T., Huot, J. & Auger, F.A. A Preexisting Microvascular Network Benefits In Vivo Revascularization of a Microvascularized Tissue-Engineered Skin Substitute. *Tissue Engineering Part A***16**, 3199-3206 (2010).

84. Risau, W. & Flamme, I. Vasculogenesis. *Annual Review of Cell and Developmental Biology***11**, 73-91 (1995).

85. Jain, R.K. Molecular regulation of vessel maturation. *Nature Medicine***9**, 685-693 (2003).

86. Ott, H.C. et al. Perfusion-decellularized matrix: using nature's platform to engineer a bioartificial heart. *Nature Medicine***14**, 213-221 (2008).

87. Uygun, B.E. et al. Organ reengineering through development of a transplantable recellularized liver graft using decellularized liver matrix. *Nature Medicine***16**, 814-U120 (2010).

88. Petersen, T.H. et al. Tissue-Engineered Lungs for in Vivo Implantation. *Science***329**, 538-541 (2010).

89. Price, A.P., England, K.A., Matson, A.M., Blazar, B.R. & Panoskaltsis-Mortari, A. Development of a Decellularized Lung Bioreactor System for Bioengineering the Lung: The Matrix Reloaded. *Tissue Engineering Part A***16**, 2581-2591 (2010).

90. Ott, H.C. et al. Regeneration and orthotopic transplantation of a bioartificial lung. *Nature Medicine***16**, 927-U131 (2010).

91. Quint, C. et al. Decellularized tissue-engineered blood vessel as an arterial conduit. *Proceedings of the National Academy of Sciences of the United States of America***108**, 9214-9219 (2011).

92. Green, J.V. et al. Effect of channel geometry on cell adhesion in microfluidic devices. *Lab on a Chip***9**, 677-685 (2009).

93. Lu, H. et al. Microfluidic shear devices for quantitative analysis of cell adhesion. *Analytical Chemistry***76**, 5257-5264 (2004).

94. Khan, O.F. & Sefton, M.V. Endothelial cell behaviour within a microfluidic mimic of the flow channels of a modular tissue engineered construct. *Biomedical Microdevices***13**, 69-87 (2011).

95. Ives, C.L., Eskin, S.G. & Mcintire, L.V. Mechanical Effects on Endothelial-Cell Morphology - Invitro Assessment. *In Vitro Cellular & Developmental Biology***22**, 500-507 (1986).

96. Helmlinger, G., Geiger, R.V., Schreck, S. & Nerem, R.M. Effects of Pulsatile Flow on Cultured Vascular Endothelial-Cell Morphology. *Journal of Biomechanical Engineering-Transactions of the Asme***113**, 123-131 (1991).

97. Malek, A.M. & Izumo, S. Mechanism of endothelial cell shape change and cytoskeletal remodeling in response to fluid shear stress. *Journal of Cell Science***109**, 713-726 (1996).

98. Shen, F., Kastrup, C.J., Liu, Y. & Ismagilov, R.F. Threshold Response of Initiation of Blood Coagulation by Tissue Factor in Patterned Microfluidic

Capillaries Is Controlled by Shear Rate. *Arteriosclerosis Thrombosis and Vascular Biology***28**, 2035-U2226 (2008).

99. Runyon, M.K., Kastrup, C.J., Johnson-Kerner, B.L., Van Ha, T.G. & Ismagilov, R.F. Effects of shear rate on propagation of blood clotting determined using microfluidics and numerical simulations. *Journal of the American Chemical Society***130**, 3458-3464 (2008).

100. Mammen, E.F. Pathogenesis of Venous Thrombosis. *Chest***102**, S640-S644 (1992).

101. Wilson, M.E. et al. Fabrication of circular microfluidic channels by combining mechanical micromilling and soft lithography. *Lab on a Chip***11**, 1550-1555 (2011).

102. Barber, R.W. & Emerson, D.R. Optimal design of microfluidic networks using biologically inspired principles. *Microfluidics and Nanofluidics***4**, 179-191 (2008).

103. Reneman, R.S. & Hoeks, A.P. Wall shear stress as measured in vivo: consequences for the design of the arterial system. *Med Biol Eng Comput***46**, 499-507 (2008).

104. Janakiraman, V., Mathur, K. & Baskaran, H. Optimal planar flow network designs for tissue engineered constructs with built-in vasculature. *Annals of Biomedical Engineering***35**, 337-347 (2007).

105. Boron, W.F. & Boulpaep, E.L. Medical physiology: a cellular and molecular approach. (Saunders/Elsevier, 2009).

106. Weinberg, C.B. & Bell, E. A Blood-Vessel Model Constructed from Collagen and Cultured Vascular Cells. *Science***231**, 397-400 (1986).

107. Drake, C.J., Hungerford, J.E. & Little, C.D. Morphogenesis of the first blood vessels. *Morphogenesis: Cellular Interactions***857**, 155-179 (1998).

108. Laschke, M.W. et al. Angiogenesis in tissue engineering: Breathing life into constructed tissue substitutes. *Tissue Engineering***12**, 2093-2104 (2006).

109. Paterlini-Brechot, P. & Benali, N.L. Circulating tumor cells (CTC) detection: Clinical impact and future directions. *Cancer Letters***253**, 180-204 (2007).

110. Krivacic, R.T. et al. A rare-cell detector for cancer. *Proceedings of the National Academy of Sciences of the United States of America***101**, 10501-10504 (2004).

111. Cristofanilli, M. et al. Circulating tumor cells, disease progression, and survival in metastatic breast cancer. *New England Journal of Medicine***351**, 781-791 (2004).

112. Rosenberg, R. et al. Comparison of two density gradient centrifugation systems for the enrichment of disseminated tumor cells in blood. *Cytometry***49**, 150-158 (2002).

113. Muller, V. et al. Circulating tumor cells in breast cancer: Correlation to bone marrow micrometastases, heterogeneous response to systemic therapy and low proliferative activity. *Clinical Cancer Research***11**, 3678-3685 (2005).

114. Racila, E. et al. Detection and characterization of carcinoma cells in the blood. *Proceedings of the National Academy of Sciences of the United States of America***95**, 4589-4594 (1998).

115. Deng, G. et al. Enrichment with anti-cytokeratin alone or combined with anti-EpCAM antibodies significantly increases the sensitivity for circulating tumor cell detection in metastatic breast cancer patients. *Breast Cancer Research***10**, - (2008).

116. Yang, L.Y. et al. Optimization of an Enrichment Process for Circulating Tumor Cells From the Blood of Head and Neck Cancer Patients Through Depletion of Normal Cells. *Biotechnology and Bioengineering***102**, 521-534 (2009).

117. Schindlbeck, C. et al. Immunomagnetic enrichment of disseminated tumor cells in bone marrow and blood of breast cancer patients by the Thomsen-Friedenreich-Antigen. *Clinical & Experimental Metastasis***25**, 233-240 (2008).

118. Riethdorf, S. et al. Detection of circulating tumor cells in peripheral blood of patients with metastatic breast cancer: A validation study of the CellSearch system. *Clinical Cancer Research***13**, 920-928 (2007).

119. Nagrath, S. et al. Isolation of rare circulating tumour cells in cancer patients by microchip technology. *Nature***450**, 1235-1239 (2007).

120. Adams, A.A. et al. Highly efficient circulating tumor cell isolation from whole blood and label-free enumeration using polymer-based microfluidics with an integrated conductivity sensor. *Journal of the American Chemical Society***130**, 8633-8641 (2008).

121. Gascoyne, P.R.C., Noshari, J., Anderson, T.J. & Becker, F.F. Isolation of rare cells from cell mixtures by dielectrophoresis. *Electrophoresis***30**, 1388-1398 (2009).

122. Vona, G. et al. Isolation by size of epithelial tumor cells - A new method for the immunomorphological and molecular characterization of circulating tumor cells. *American Journal of Pathology***156**, 57-63 (2000).

123. Lelievre, L. et al. Effect of laparoscopy versus laparotomy on circulating tumor cells using isolation by size of epithelial tumor cells. *International Journal of Gynecological Cancer***14**, 229-233 (2004).

124. Pinzani, P. et al. Isolation by size of epithelial tumor cells in peripheral blood of patients with breast cancer: correlation with real-time reverse transcriptase-polymerase chain reaction results and feasibility of molecular analysis by laser microdissection. *Human Pathology***37**, 711-718 (2006).

125. Chen, Z.Z. et al. Pool-dam structure based microfluidic devices for filtering tumor cells from blood mixtures. *Surface and Interface Analysis***38**, 996-1003 (2006).

126. Zabaglo, L. et al. Cell filtration-laser scanning cytometry for the characterisation of circulating breast cancer cells. *Cytometry Part A***55A**, 102-108 (2003).

127. Zheng, S. et al. Membrane microfilter device for selective capture, electrolysis and genomic analysis of human circulating tumor cells. *Journal of Chromatography A***1162**, 154-161 (2007).

128. Tan, S.J., Yobas, L., Lee, G.Y.H., Ong, C.N. & Lim, C.T. Microdevice for the isolation and enumeration of cancer cells from blood. *Biomedical Microdevices***11**, 883-892 (2009).

129. Kuo, J.S. et al. Microfabricating high-aspect-ratio structures in polyurethane-methacrylate (PUMA) disposable microfluidic devices. *Lab on a Chip***9**, 1951-1956 (2009).

130. Mohamed, H., Murray, M., Turner, J.N. & Caggana, M. Isolation of tumor cells using size and deformation. *Journal of Chromatography A***1216**, 8289-8295 (2009).

131. Chang, S.F. et al. Tumor cell cycle arrest induced by shear stress: Roles of integrins and Smad. *Proceedings of the National Academy of Sciences of the United States of America***105**, 3927-3932 (2008).

132. Borgen, E. et al. Standardization of the immunocytochemical detection of cancer cells in BM and blood: I. establishment of objective criteria for the evaluation of immunostained cells. *Cytotherapy***1**, 377-388 (1999).

133. Kraeft, S.K. et al. Detection and analysis of cancer cells in blood and bone marrow using a rare event imaging system. *Clinical Cancer Research***6**, 434-442 (2000).

134. Meng, S.D. et al. Circulating tumor cells in patients with breast cancer dormancy. *Clinical Cancer Research***10**, 8152-8162 (2004).

135. Pierga, J.Y. et al. Clinical significance of immunocytochemical detection of tumor cells using digital microscopy in peripheral blood and bone marrow of breast cancer patients. *Clinical Cancer Research***10**, 1392-1400 (2004).

136. Vona, G. et al. Impact of cytomorphological detection of circulating tumor cells in patients with liver cancer. *Hepatology***39**, 792-797 (2004).

137. Friedl, P. & Wolf, K. Tumour-cell invasion and migration: Diversity and escape mechanisms. *Nature Reviews Cancer***3**, 362-374 (2003).

138. Christiansen, J.J. & Rajasekaran, A.K. Reassessing epithelial to mesenchymal transition as a prerequisite for carcinoma invasion and metastasis. *Cancer Research***66**, 8319-8326 (2006).

139. Al-Mehdi, A.B. et al. Intravascular origin of metastasis from the proliferation of endothelium-attached tumor cells: a new model for metastasis. *Nature Medicine***6**, 100-102 (2000).

140. Molnar, B., Ladanyi, A., Tanko, L., Sreter, L. & Tulassay, Z. Circulating tumor cell clusters in the peripheral blood of colorectal cancer patients. *Clinical Cancer Research***7**, 4080-4085 (2001).

141. Wang, Z.P. et al. Identification and characterization of circulating prostate carcinoma cells. *Cancer***88**, 2787-2795 (2000).

142. Swerts, K. et al. Standardization of the immunocytochemical detection of neuroblastoma cells in bone marrow. *Journal of Histochemistry & Cytochemistry***53**, 1433-1440 (2005).

143. Went, P.T. et al. Frequent EpCam protein expression in human carcinomas. *Human Pathology***35**, 122-128 (2004).

144. Gastl, G., Spizzo, G., Obrist, P., Dunser, M. & Mikuz, G. Ep-CAM overexpression in breast cancer as a predictor of survival. *Lancet***356**, 1981-1982 (2000).

145. Spizzo, G. et al. Correlation of COX-2 and Fp-CAM overexpression in human invasive breast cancer and its impact on survival. *British Journal of Cancer***88**, 574-578 (2003).

146. Spizzo, G. et al. High Ep-CAM expression is associated with poor prognosis in node-positive breast cancer. *Breast Cancer Research and Treatment***86**, 207-213 (2004).

147. Allard, W.J. et al. Tumor cells circulate in the peripheral blood of all major carcinomas but not in healthy subjects or patients with nonmalignant diseases. *Clinical Cancer Research***10**, 6897-6904 (2004).

148. Sergeant, G., Penninckx, F. & Topal, B. Quantitative RT-PCR detection of colorectal tumor cells in peripheral blood--a systematic review. *J Surg Res***150**, 144-152 (2008).

149. Yamamoto, H., Kato, H., Uruma, M., Nitta, M. & Takamoto, S. Identification of two distinct populations of endothelial progenitor cells differing in size and antigen expression from human umbilical cord blood. *Annals of Hematology***87**, 87-95 (2008).

150. Harris, L. et al. American society of clinical oncology 2007 update of recommendations for the use of tumor markers in breast cancer. *Journal of Clinical Oncology***25**, 5287-5312 (2007).

151. Mehta, K. & Janovsky, I. Measurements of electron depth-dose distributions in thick plastics and effects of accumulated charge. *Radiation Physics and Chemistry***47**, 487-490 (1996).

152. Young, M.E., Carroad, P.A. & Bell, R.L. Estimation of Diffusion-Coefficients of Proteins. *Biotechnology and Bioengineering***22**, 947-955 (1980).

153. Tsang, V.L. & Bhatia, S.N. Fabrication of three-dimensional tissues. *Tissue Engineering Ii: Basics of Tissue Engineering and Tissue Applications***103**, 189-205 (2007).

154. Andersson, H. & van den Berg, A. Microfabrication and microfluidics for tissue engineering: state of the art and future opportunities. *Lab on a Chip***4**, 98-103 (2004).

155. Prabhakarpandian, B. et al. Synthetic microvascular networks for quantitative analysis of particle adhesion. *Biomedical Microdevices***10**, 585-595 (2008).

156. Anderson, J.R. et al. Fabrication of topologically complex three-dimensional microfluidic systems in PDMS by rapid prototyping. *Analytical Chemistry***72**, 3158-3164 (2000).

157. Hollister, S.J. Scaffold engineering: a bridge to where? *Biofabrication***1**, 1-14 (2009).

158. Ficker, T. Electrostatic discharges and multifractal analysis of their Lichtenberg figures. *Journal of Physics D-Applied Physics***32**, 219-226 (1999).

159. Furuta, J., Hiraoka, E. & Okamoto, S. Discharge Figures in Dielectrics by Electron Irradiation. *Journal of Applied Physics***37**, 1873-1878 (1966).

160. Noskov, M.D., Malinovski, A.S., Cooke, C.M., Wright, K.A. & Schwab, A.J. Experimental study and simulation of space charge stimulated discharge. *Journal of Applied Physics***92**, 4926-4934 (2002).

161. Podgoršak, E.B. Radiation physics for medical physicists, Edn. 2nd, enl. (Springer, Heidelberg; 2010).

162. Karch, R. et al. Fractal properties of perfusion heterogeneity in optimized arterial trees: A model study. *Journal of General Physiology***122**, 307-321 (2003).

163. Marxen, M. & Henkelman, R.M. Branching tree model with fractal vascular resistance explains fractal perfusion heterogeneity. *American Journal of Physiology-Heart and Circulatory Physiology***284**, H1848-H1857 (2003).

164. Schreiner, W. et al. Heterogeneous perfusion is a consequence of uniform shear stress in optimized arterial tree models. *Journal of Theoretical Biology***220**, 285-301 (2003).

165. Zamir, M. Vascular system of the human heart: Some branching and scaling issues. *Scaling in Biology*, 129-143 (2000).

166. Karau, K.L., Krenz, G.S. & Dawson, C.A. Branching exponent heterogeneity and wall shear stress distribution in vascular trees. *American Journal of Physiology-Heart and Circulatory Physiology***280**, H1256-H1263 (2001).

167. Arts, T., Kruger, R.T.I., Vangerven, W., Lambregts, J.A.C. & Reneman, R.S. Propagation Velocity and Reflection of Pressure Waves in the Canine Coronary-Artery. *American Journal of Physiology***237**, H469-H474 (1979).

168. Sherman, T.F. On Connecting Large Vessels to Small - the Meaning of Murray Law. *Journal of General Physiology***78**, 431-453 (1981).

169. Masters, B.R. Fractal analysis of the vascular tree in the human retina. *Annual Review of Biomedical Engineering***6**, 427-452 (2004).

170. Kerbel, R.S. Molecular origins of cancer: Tumor angiogenesis. *New Engl J Med***358**, 2039-2049 (2008).

171. Shevkoplyas, S.S., Yoshida, T., Gifford, S.C. & Bitensky, M.W. Direct measurement of the impact of impaired erythrocyte deformability on microvascular network perfusion in a microfluidic device. *Lab Chip***6**, 914-920 (2006).

172. Lima, R. et al. In vitro blood flow in a rectangular PDMS microchannel: experimental observations using a confocal micro-PIV system. *Biomed Microdevices***10**, 153-167 (2008).

173. Tsai, M. et al. In vitro modeling of the microvascular occlusion and thrombosis that occur in hematologic diseases using microfluidic technology. *J Clin Invest***122**, 408-418 (2012).

174. Song, S.H. et al. A rapid and simple fabrication method for 3-dimensional circular microfluidic channel using metal wire removal process. *Microfluid Nanofluid***9**, 533-540 (2010).

175. Esser-Kahn, A.P. et al. Three-Dimensional Microvascular Fiber-Reinforced Composites. *Adv Mater***23**, 3654-3658 (2011).

176. Fiddes, L.K. et al. A circular cross-section PDMS microfluidics system for replication of cardiovascular flow conditions. *Biomaterials***31**, 3459-3464 (2010).

177. Abdelgawad, M. et al. A fast and simple method to fabricate circular microchannels in polydimethylsiloxane (PDMS). *Lab Chip***11**, 545-551 (2011).

178. Abate, A.R., Lee, D., Do, T., Holtze, C. & Weitz, D.A. Glass coating for PDMS microfluidic channels by sol-gel methods. *Lab Chip***8**, 516-518 (2008).

179. Lee, S.H., Kang, D.H., Kim, H.N. & Suh, K.Y. Use of directly molded poly(methyl methacrylate) channels for microfluidic applications. *Lab Chip***10**, 3300-3306 (2010).

180. Toepke, M.W. & Beebe, D.J. PDMS absorption of small molecules and consequences in microfluidic applications. *Lab Chip***6**, 1484-1486 (2006).

181. Regehr, K.J. et al. Biological implications of polydimethylsiloxane-based microfluidic cell culture. *Lab Chip***9**, 2132-2139 (2009).

182. Jain, A. & Munn, L.L. Determinants of Leukocyte Margination in Rectangular Microchannels. *Plos One***4**, e7104 (2009).

183. Crouch, A.S., Miller, D., Luebke, K.J. & Hu, W. Correlation of anisotropic cell behaviors with topographic aspect ratio. *Biomaterials***30**, 1560-1567 (2009).

184. Khabiry, M. et al. Cell Docking in Double Grooves in a Microfluidic Channel. *Small***5**, 1186-1194 (2009).

185. O'Neill, A.T., Monteiro-Riviere, N.A. & Walker, G.M. Microfabricated curtains for controlled cell seeding in high throughput microfluidic systems. *Lab on a Chip***9**, 1756-1762 (2009).

186. Walboomers, X.F. & Jansen, J.A. Cell and tissue behavior on micro-grooved surfaces. *Odontology***89**, 2-11 (2001).

187. Zhu, X.Y. et al. Fabrication of reconfigurable protein matrices by cracking. *Nature materials***4**, 403-406 (2005).

188. Taylor, A.M. et al. A microfluidic culture platform for CNS axonal injury, regeneration and transport. *Nature Methods***2**, 599-605 (2005).

189. Guo, L.J., Cheng, X. & Chou, C.F. Fabrication of size-controllable nanofluidic channels by nanoimprinting and its application for DNA stretching. *Nano Letters***4**, 69-73 (2004).

190. Li, J. et al. Ion-beam sculpting at nanometre length scales. *Nature***412**, 166-169 (2001).

191. Perry, J.M., Zhou, K., Harms, Z.D. & Jacobson, S.C. Ion transport in nanofluidic funnels. *ACS Nano***4**, 3897-3902 (2010).

192. Stavis, S.M., Strychalski, E.A. & Gaitan, M. Nanofluidic structures with complex three-dimensional surfaces. *Nanotechnology***20** (2009).

193. Uram, J.D., Ke, K., Hunt, A.J. & Mayer, M. Label-free affinity assays by rapid detection of immune complexes in submicrometer pores. *Angew Chem Int Edit***45**, 2281-2285 (2006).

194. Ebeling, W. et al. Proteinase K from Tritirachium-Album Limber. *European Journal of Biochemistry***47**, 91-97 (1974).

195. Gopferich, A. & Langer, R. Modeling of Polymer Erosion. *Macromolecules***26**, 4105-4112 (1993).

196. Gopferich, A. Mechanisms of polymer degradation and erosion. *Biomaterials***17**, 103-114 (1996).

197. Eaton, W.P., Jarecki, R.L. & Smith, J.H. Prediction of release-etch times for surface-micromachined structures. *Transducers 97 - 1997 International Conference on Solid-State Sensors and Actuators, Digest of Technical Papers, Vols 1 and 2*, 249-252 (1997).

198. Takayama, S. et al. Topographical micropatterning of poly(dimethylsiloxane) using laminar flows of liquids in capillaries. *Advanced Materials***13**, 570-574 (2001).

199. Brister, P.C. & Weston, K.D. Patterned solvent delivery and etching for the fabrication of plastic microfluidic devices. *Analytical Chemistry***77**, 7478-7482 (2005).

200. Mu, X. et al. Laminar flow used as "liquid etch mask" in wet chemical etching to generate glass microstructures with an improved aspect ratio. *Lab on a Chip***9**, 1994-1996 (2009).

201. Pandhare, J., Dash, C., Rao, M. & Deshpande, V. Slow tight binding inhibition of proteinase K by a proteinaceous inhibitor - Conformational alterations responsible for conferring irreversibility to the enzyme-inhibitor complex. *Journal of Biological Chemistry***278**, 48735-48744 (2003).

202. MacDonald, R.T., McCarthy, S.P. & Gross, R.A. Enzymatic degradability of poly(lactide): Effects of chain stereochemistry and material crystallinity. *Macromolecules***29**, 7356-7361 (1996).

203. Park, S.D., Todo, M. & Arakawa, K. Effects of isothermal crystallization on fracture toughness and crack growth behavior of poly (lactic acid). *Journal of Materials Science***40**, 1055-1058 (2005).

204. Mantovani, A., Cassatella, M.A., Costantini, C. & Jaillon, S. Neutrophils in the activation and regulation of innate and adaptive immunity. *Nature Reviews Immunology***11**, 519-531 (2011).

205. Stott, S.L. et al. Isolation of circulating tumor cells using a microvortex-generating herringbone-chip. *Proceedings of the National Academy of Sciences of the United States of America***107**, 18392-18397 (2010).

206. Huang, J.H., Jayaraman, A. & Ugaz, V.M. Enzymatic sculpting of nanoscale and microscale surface topographies. *Angew Chem Int Ed Engl***51**, 9619-9623 (2012).

207. Sudarsan, A.P. & Ugaz, V.M. Multivortex micromixing. *Proceedings of the National Academy of Sciences of the United States of America***103**, 7228-7233 (2006).

208. Sethu, P., Sin, A. & Toner, M. Microfluidic diffusive filter for apheresis (leukapheresis). *Lab on a Chip***6**, 83-89 (2006).

209. VanDelinder, V. & Groisman, A. Perfusion in microfluidic cross-flow: Separation of white blood cells from whole blood and exchange of medium in a continuous flow. *Anal Chem***79**, 2023-2030 (2007).

210. Zheng, S.Y., Liu, J.Q. & Tai, Y.C. Streamline-based microfluidic devices for erythrocytes and leukocytes separation. *J Microelectromech S***17**, 1029-1038 (2008).

211. Choi, S., Song, S., Choi, C. & Park, J.K. Continuous blood cell separation by hydrophoretic filtration. *Lab Chip***7**, 1532-1538 (2007).

212. Inglis, D.W., Lord, M. & Nordon, R.E. Scaling deterministic lateral displacement arrays for high throughput and dilution-free enrichment of leukocytes. *J Micromech Microeng***21**, 054024 (2011).

213. Wu, Z.G., Willing, B., Bjerketorp, J., Jansson, J.K. & Hjort, K. Soft inertial microfluidics for high throughput separation of bacteria from human blood cells. *Lab Chip***9**, 1193-1199 (2009).

214. Mach, A.J. & Di Carlo, D. Continuous Scalable Blood Filtration Device Using Inertial Microfluidics. *Biotechnol Bioeng***107**, 302-311 (2010).

215. Jain, A. & Munn, L.L. Biomimetic postcapillary expansions for enhancing rare blood cell separation on a microfluidic chip. *Lab Chip***11**, 2941-2947 (2011).

216. Bhagat, A.A.S., Hou, H.W., Li, L.D., Lim, C.T. & Han, J.Y. Pinched flow coupled shear-modulated inertial microfluidics for high-throughput rare blood cell separation. *Lab Chip***11**, 1870-1878 (2011).

217. Hur, S.C., Mach, A.J. & Di Carlo, D. High-throughput size-based rare cell enrichment using microscale vortices. *Biomicrofluidics***5** (2011).

218. Seo, J., Lean, M.H. & Kole, A. Membrane-free microfiltration by asymmetric inertial migration. *Applied Physics Letters***91**, 033901 (2007).

219. Bhagat, A.A.S., Kuntaegowdanahalli, S.S. & Papautsky, I. Continuous particle separation in spiral microchannels using dean flows and differential migration. *Lab Chip***8**, 1906-1914 (2008).

220. Gossett, D.R. & Di Carlo, D. Particle Focusing Mechanisms in Curving Confined Flows. *Anal Chem***81**, 8459-8465 (2009).

221. Hatch, A. et al. A rapid diffusion immunoassay in a T-sensor. *Nat Biotechnol***19**, 461-465 (2001).

222. Chen, X., Cui, D.F., Liu, C.C. & Li, H. Microfluidic chip for blood cell separation and collection based on crossflow filtration. *Sensors and Actuators B-Chemical***130**, 216-221 (2008).

223. Ji, H.M. et al. Silicon-based microfilters for whole blood cell separation. *Biomedical Microdevices***10**, 251-257 (2008).

224. Tokiwa, Y. & Suzuki, T. Hydrolysis of Polyesters by Lipases. *Nature***270**, 76-78 (1977).

225. Suyama, T., Tokiwa, Y., Ouichanpagdee, P., Kanagawa, T. & Kamagata, Y. Phylogenetic affiliation of soil bacteria that degrade aliphatic polyesters available commercially as biodegradable plastics. *Applied and Environmental Microbiology***64**, 5008-5011 (1998).

226. Kotz, K.T. et al. Clinical microfluidics for neutrophil genomics and proteomics. *Nature Medicine***16**, 1042-U1142 (2010).

227. Hoshino, K. et al. Microchip-based immunomagnetic detection of circulating tumor cells. *Lab Chip***11**, 3449-3457 (2011).

228. Plouffe, B.D., Mahalanabis, M., Lewis, L.H., Klapperich, C.M. & Murthy, S.K. Clinically relevant microfluidic magnetophoretic isolation of rare-cell populations for diagnostic and therapeutic monitoring applications. *Anal Chem***84**, 1336-1344 (2012).

229. Wang, S. et al. Highly efficient capture of circulating tumor cells by using nanostructured silicon substrates with integrated chaotic micromixers. *Angew Chem Int Ed Engl***50**, 3084-3088 (2011).

230. Stott, S.L. et al. Isolation of circulating tumor cells using a microvortex-generating herringbone-chip. *Proc Natl Acad Sci U S A***107**, 18392-18397 (2010).

231. Moon, H.S. et al. Continuous separation of breast cancer cells from blood samples using multi-orifice flow fractionation (MOFF) and dielectrophoresis (DEP). *Lab Chip***11**, 1118-1125 (2011).

232. Bhagat, A.A., Hou, H.W., Li, L.D., Lim, C.T. & Han, J. Pinched flow coupled shear-modulated inertial microfluidics for high-throughput rare blood cell separation. *Lab Chip***11**, 1870-1878 (2011).

233. Hur, S.C., Mach, A.J. & Di Carlo, D. High-throughput size-based rare cell enrichment using microscale vortices. *Biomicrofluidics***5**, 22206 (2011).